Computational strategies toward the modelling of the intervertebral disc

Julien Vignollet

Submitted in fulfilment of the requirements for the Degree of Doctor of Philosophy

School of Engineering
University of Glasgow

November 2012

Declaration

I declare that this thesis is a record of the original work carried out by myself under the supervision of Professor Chris Pearce and Dr. Lukasz Kaczmarczyk in the Department of Civil Engineering at the University of Glasgow, United Kingdom, during the period of January 2008 to August 2012. The copyright of this thesis belongs to the author under the terms of the United Kingdom Copyright acts. Due acknowledgement must always be made of the use of any material contained in, or derived from, this thesis. The thesis has not been presented elsewhere in consideration for a higher degree.

Julien Vignollet

Abstract

Lumbar back pain has considerable socio-economical impacts, motivating a recently increasing interest from the research community. Yet, mechanisms triggering pain are not fully understood and this considerably hinders the development of efficient treatments and therapies. The objective of this thesis is to participate to the general understanding of the biomechanics of the spine through the development of computational strategies for the intervertebral disc.

The intervertebral disc is a complex structure mainly comprised of the nucleus pulposus and the annulus fibrosus. The nucleus pulposus is the gelatinous core of the disc, which consists of a charged and hydrated extra-cellular matrix and an ionised interstitial fluid. It is enclosed in the annulus fibrosus which is formed by concentric layers of aligned collagen fibre sheets, oriented in an alternating fashion.

A biphasic swelling model has been derived using mixture theory for soft, hydrated and charged tissues in order to capture the salient characteristics of the disc's behaviour. The model fully couples the solid matrix under finite deformations with the ionised interstitial fluid. The nucleus is assumed to behave isotropically while the effects of the collagen fibres in the annulus fibrosus are accounted for with a transversely isotropic model. The fixed negative charges of the proteoglycans, which induce an osmotic pressure responsible for the swelling capabilities of the disc, are constitutively modelled under the simplifying Lanir hypothesis.

A Newton-Raphson solver was specifically built to solve the resulting nonlinear system of equations, together with a verification procedure to ensure successful implementation of the code. This was first reduced to the one dimensional case in order to demonstrate the appropriateness of the biphasic swelling model. The three dimensional model exhibited numerical instabilities, manifesting in the form of non-physical oscillations in

the pressure field near boundaries, when loads and free-draining boundary conditions are simultaneously applied. As an alternative to considerable mesh refinement, these spurious instabilities have been addressed using a Galerkin Least-Square formulation, which has been extended for finite deformations. The performance and limitations of the GLS framework, which drastically reduces the pressure discrepancies and prevents the oscillations from propagating through the continuum, are demonstrated on numerical examples. Finally, the current state of the model's development is assessed, and recommendations for further improvements are proposed.

Acknowledgements

This is the place where, traditionally, gratitude is expressed toward people who offered support through this long process, and I will not depart from this ritual.

It is natural to start with Professor Chris Pearce, my primary supervisor, who offered this opportunity in the first place. I am grateful for the faith he placed in me, but also for the constant support and encouragement he provided throughout this doctoral project.

My second supervisor, Dr. Lukasz Kaczmarczyk, was also an important point of support and inspiration. He, for example, motivated me to write my own code rather than utilising commercial packages. This turned out to be a very enriching experience, which furthered the quality and content of my work.

I am also grateful for the numerous conversations I had with Dr. Phil Riches regarding the nature of charged soft tissues, which contributed significantly to my understanding of the intervertebral disc.

I would also like to thank the whole team in the Civil Engineering Department, and in particular Dr. Tomasz Koziara for moral and technical support, and Alan Kelly for trying to help with complex meshes. This achievement was also only made possible through the unconditional support and faith, even from a distance, of my family.

Contents

Chapter I

Introduction

The primary objective of this thesis is the formulation of a computational framework for the modelling of the intervertebral disc. It is written in a modular fashion, which in part reflects the chronology of the enterprise, with the intention of producing chapters that can, to some extent, be read independently from one another. To this end, each of them is equipped with clear motivations and objectives, as well as a literature review. The thesis is organised as follows:

- **Chapter II** describes, from an engineering perspective, the biomechanics of the intervertebral disc. It has the twofold objective of characterising the structure and the physiological behaviour of the disc to facilitate the modelling process, and to identify areas where computational modelling can make an impact, intrinsically motivating the purpose of the thesis.

- **Chapter III** focusses on the establishment of a modelling strategy for the intervertebral disc. Existing soft tissue models are reviewed and the general philosophy of the current model is defined. The theoretical framework of the biphasic swelling model is derived.

- **Chapter IV** proposes a framework for the numerical treatment of the biphasic swelling model. This includes the linearisation of the weak form of the problem for the implementation of a Newton-Raphson solver. A specific termination criterion for the iterative loop is also proposed.

- **Chapter V** reduces the model to the one dimensional case. This step was crucial to evaluate the appropriateness of the biphasic swelling model when applied to a relatively simple problem, but also to facilitate familiarity with the mechanics of porous and charged tissues. The 1D model is validated against experimental confined compression tests.

- **Chapter VI** is concerned with the implementation of the three dimensional problem. This involves the selection of constitutive models for each phase and the description of the computational implementation, in particular the design of a methodology to verify this implementation.

- **Chapter VII** reveals the existence of numerical instabilities manifesting in the pressure field at the early stage of simulations where free-flow and loads are simultaneously applied at the boundary. A Galerkin least-square stabilisation technique is proposed to address this shortcoming and tested against confined and unconfined tests.

- **Chapter VIII** appraises the current state of the development of the current framework. A number of the model's features are presented and compared to literature data. Areas requiring further attention are also highlighted.

Chapter II

The biomechanics of the intervertebral disc

The objective of this chapter is to establish an understanding of the biological composition of the intervertebral disc, its behaviour and main load transfer mechanisms. This will allow us to define a modeling strategy in the following chapters. To this end, a general description of the intervertebral disc from an engineering perspective is proposed. A short review of the most common disc disruptions, pathologies and potential sources of back pain is provided, introducing areas where the development of numerical models could prove useful.

II.1 Anatomy, biology and physiology

The human spine is comprised of 24 vertebrae and an additional 5 that are fused to form the sacrum. Flexible spacers known as intervertebral discs (which will interchangeably be referred to as the IVD or simply the disc) are found interspersed between vertebrae: 6 are located in the cervical region, 12 in the thoracic region and 5 in the lumbar region (often called the lower back). As Fig. II.1a suggests, the size of the discs (thickness and surface area) is greater in the lower back: approximately 10mm in height, 65mm laterally and 45mm along the anterior-posterior axis; they also account for approximately 25% of the spine's height. Intervertebral discs are essentially made up of three parts (see Fig. II.1b-II.1c): the nucleus pulposus (NP or simply the nucleus) is located at the centre of the IVD, it is radially encapsulated by the multi-lamellar annulus fibrosus (AF or annulus), and axially sandwiched between the cartilaginous endplates (sometimes referred to as CEP or endplates).

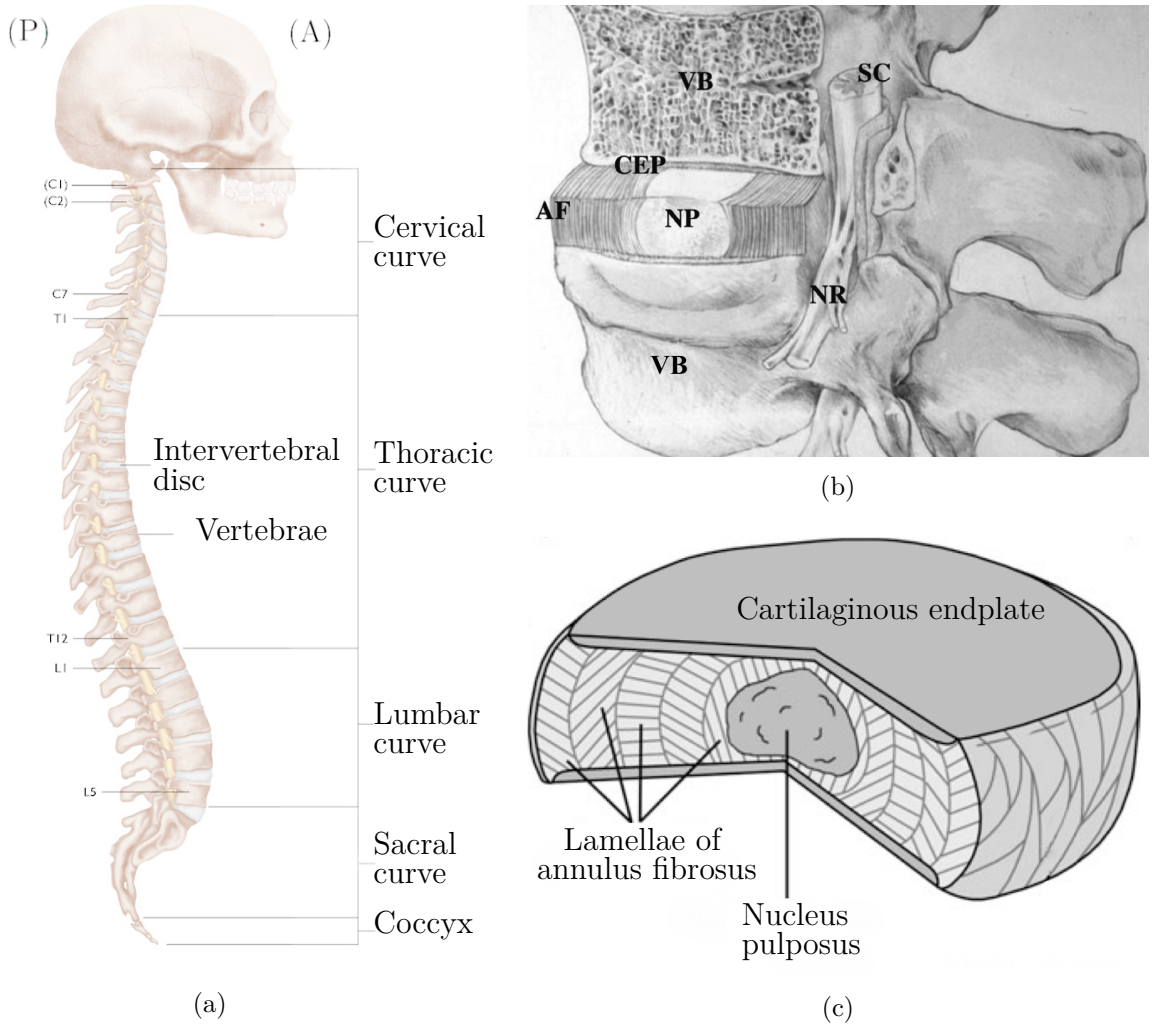

Figure II.1: (a) Spine curvatures, A and P denote the anterior and posterior sides (adapted from www.martianpictures.com) (b) A motion segment: section through a disc and its superior vertebra. The IVD, comprised of the nucleus pulposus (NP), the annulus fibrosus (AF) and the cartilaginous endplates (CEP) is located between the vertebral bodies (VB). The spinal chord (SC) and a nerve route (NR) are also visible (Urban and Roberts, 2003) (c) Structure of the IVD (adapted from Raj (2008))

The **nucleus pulposus** is the gelatinous core of the IVD. It is mainly comprised of an interstitial fluid, accounting for 75-90% of its wet weight, and a solid matrix composed of flexible type II collagen fibres and elastin fibrils. These are randomly and radially oriented (Urban and Roberts, 2003) respectively. This extra-cellular matrix, which represents about 15% of the wet weight, embeds the hydrophilic proteoglycan molecules (approximately 5% of the wet weight). The high proteoglycan content is dominated by aggrecan molecules, containing glycoaminoglycans (GAG's),

which comprise a high density of negative charges. As demonstrated in the following section, concentration gradients of GAG's give rise to an osmotic pressure that is responsible for the highly hydrated nature of the IVD. It is important, from a modelling perspective, to mention that proteoglycans are fairly large molecules that are trapped in the solid matrix, and as such have been found not to leach out of the tissue upon loading (Heneghan and Riches, 2008a).

The **annulus fibrosus** is composed of 15 to 25 concentric layers of collagen sheets called lamellae, frequently compared in the literature to the structure of an onion or a tyre. In contrast to the nucleus pulposus, the annulus is slightly less hydrated (60-75% of the total weight), contains a similar amount of proteoglycans and considerably more collagen fibres (about 15% wet weight). Conversely, the distribution of the collagen fibres in the annulus is highly organised (see Fig. II.1c and II.4c): collagen fibres run parallel within the plane of the lamella and they are inclined at an angle between 40°-70° (Holzapfel et al., 2005) from the spinal axis. The orientation of the fibres alternates to the left and the right of the spinal axis between adjacent lamellae, while the magnitude of the incline varies with the location within the annulus (anterior versus posterior, inner versus outer annulus). The photographs on Fig. II.2 illustrate the absence of a clear demarcation between the nucleus and the annulus. The region where AF and NP seem to blend is called the transition zone (TZ) and can span up to 30mm (Shankar et al., 2009).

The stiffness of the AF gradually increases from the inner lamellae (composed of the flexible type II collagen) that are anchored to the CEP, to the fibre-dense outer lamellae (mainly made up of the stiff type I collagen, similar to ligaments) that are directly attached to the vertebral body. The outer lamellae of the annulus fibrosus also comprise ramifications of the spinal chord, which can be responsible for pain perception (see following section for discussion on pain). Additionally, radial inter-

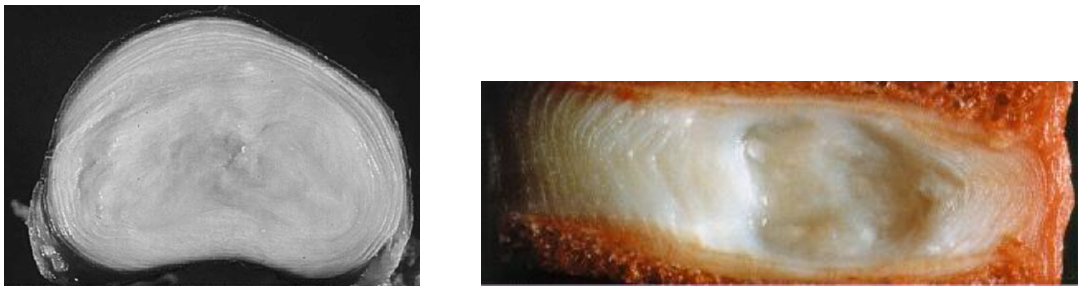

(a) Mid-sagittal section (Vernon-Roberts et al., 1997)

(b) Transverse section through an intervertebral disc and its adjacent vertebrae (Adams et al., 2006)

Figure II.2: Sections through healthy intervertebral discs revealing the nucleus pulposus and the annulus fibrosus

lamellar connection is secured by a complex and irregular trans-lamellar bridging of elastin fibres (Pezowicz et al. (2006); Schollum et al. (2008); Veres et al. (2008)). It is also worth noting that collagen fibres have a crimped structure (e.g. Baer et al. (1991) and Pezowicz (2010)): this offers folding capabilities to the fibres under compression, but also explains the flat toe-region reported in tensile stretching of the annulus fibrosus (e.g. Nerurkar et al. (2008)).

The nucleus and annulus are axially enclosed by **cartilaginous endplates** (CEP) operating as an approximately 0.8mm-thick interface to the adjacent vertebral bodies. The endplates, which are composed of hyaline cartilage, nearly span across the entire interface between the discs and the vertebral bodies, only leaving a narrow rim uncovered (the epiphyseal ring). In this region, sometimes referred to as the ligamentous portion of the annulus, the collagen fibres of the AF are directly anchored to the bone. The CEP are semi-permeable membranes that play a very important role in the nutrition of the IVD. Intervertebral discs are the largest avascular components of the human body, and as such have a limited supply of metabolites. Endplates enable nutrient-rich fluid to flow through the marrow contact channels of the vertebral bodies. As it will be emphasised in the next section, fluid flow is the result of two mechanisms that are independently induced, which is likely a physiological consequence of their serving different purposes in the nutritional process of the IVD (e.g. Kraemer et al. (1985), Ferguson et al. (2004) and Urban et al. (2004)):

- the convective fluid-flow results from deformation of the extracellular matrix upon loading and unloading: this is the main source of transport of large metabolites (e.g. enzymes and hormones)
- the diffusive fluid-flow process is initiated by the osmotic pressure: this is the main source of transport of small metabolites (e.g. oxygen and glucose)

Endplates are the dominant metabolite supply channel of the IVD ((Ayotte et al., 1999), Riches and McNally (2005)). However, fluid flow through the outer annulus fibrosus offers an additional, but limited, nutritional pathway due the presence of minor blood supply. As IVDs have a rather low cell content compared to other regions of the body, a sustained transport of metabolites is essential for the synthesis of collagen and proteoglycans.

Although IVDs can vary considerably in size and shape in order to match the size of the vertebrae to which they are attached, as well as the spine's curvature, their composition is uniform throughout the spine (Shankar et al., 2009).

II.2 The mechanical response of the intervertebral disc

Intervertebral discs play remarkable roles in the spine. Due to their malleable structure and the fact that they are interspersed with vertebrae, they act as flexible joints to the otherwise rigid vertebral column. They also participate in the stable transfer to the lower extremities of compressive, bending and twisting loads arising from upper body weight and muscle activity. Additionally, they act as shock absorbers for the upper body.

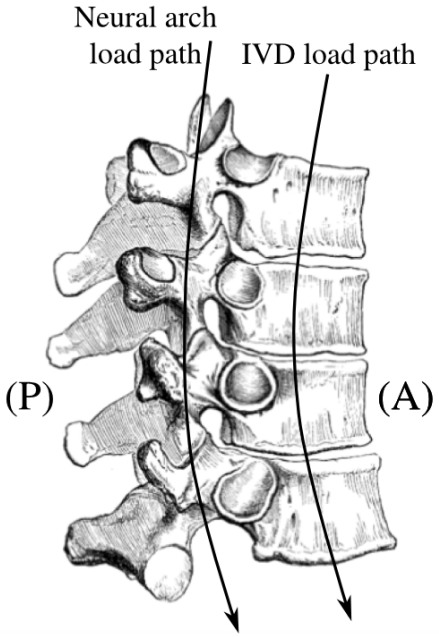

(a) Illustration of the load sharing between anterior and posterior spine (adapted from Strandring (2008))

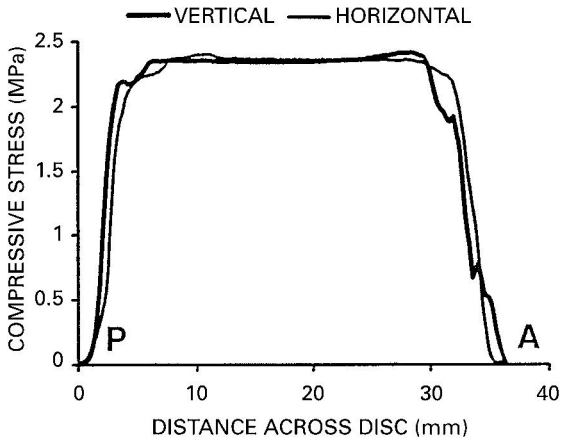

(b) The stress distribution in the transverse plane of an healthy IVD subjected to 1kN compression shows a near to hydrostatic state across the whole disc (Adams et al. (1996b))

Figure II.3: The load transfer through the spine - Posteriorly (P) and anteriorly (A)

Due the complex network of muscles and ligaments holding the discs and vertebrae together, the spine experiences compressive loads in significant excess to the weight of the upper body. It was for example estimated in Schultz et al. (1982), based on experiments performed on patients with a mean weight of 63kg (i.e. equivalent to 617N), that the third lumbar vertebra is subjected to 440N at relaxed standing posture. This number would rise by 20N simply by extending the arms forward. Additionally, the compressive loads increased to 650N when the subject held an 8kg weight close to the chest, and to 1170N when this same weight was lifted forward. Even if, as

illustrated on Fig. II.3a, the neural arch offloads a fraction of the compressive forces from the IVD (estimated about 5-10% in Haher et al. (1994) and Pollintine et al. (2004)), intervertebral discs are subjected to high stress levels. Common sense tells us that obtaining *in-vivo* estimations of the intra-discal stress state is a difficult task. However, in at least three studies (Nachemson and Morris, 1964; Wilke et al., 1999, 2001), healthy volunteers accepted to have a needle transducer the size of a match implanted in a lumbar IVD, so that stress levels within the disc could be recorded while they performed various activities. In Schultz et al. (1982), the intra-discal pressure was estimated indirectly by converting measures of electrical activity in neighbouring muscles into IVD stress. While data reported in these publications are contrasting (e.g. ranging from 0.1MPa to 0.5MPa in relaxed erect posture), it is generally admitted that the pressure within the IVD under daily activities ranges between 0.1MPa and 2.5MPa. Similar magnitudes were measured on *in-vitro* experiments (e.g. Adams et al. (1994)).

The load transfer through the IVD is only made possible by a tight cooperation between the nucleus and the annulus, resulting in optimal utilisation of the superior tensile properties of the collagen fibres within the annulus. The mechanism is schematically explained on Fig. II.4. When the disc is subjected to axial compression, the highly hydrated nucleus pulposus experiences a near to hydrostatic state (see even pressure distribution across the disc on Fig. II.3b) and expands radially, forcing the annulus fibrosus to bulge. This outward pressure, which is resisted by a strong superior and inferior anchoring of the fibres to the VB and the CEP, prevents the annulus from buckling (see left AF on Fig. II.4b). This results in a complex biaxial tensile state within the lamellae, essentially stretching the fibres in tension (Baer et al., 1991). Under bending, a similar mechanism takes place on the compressive

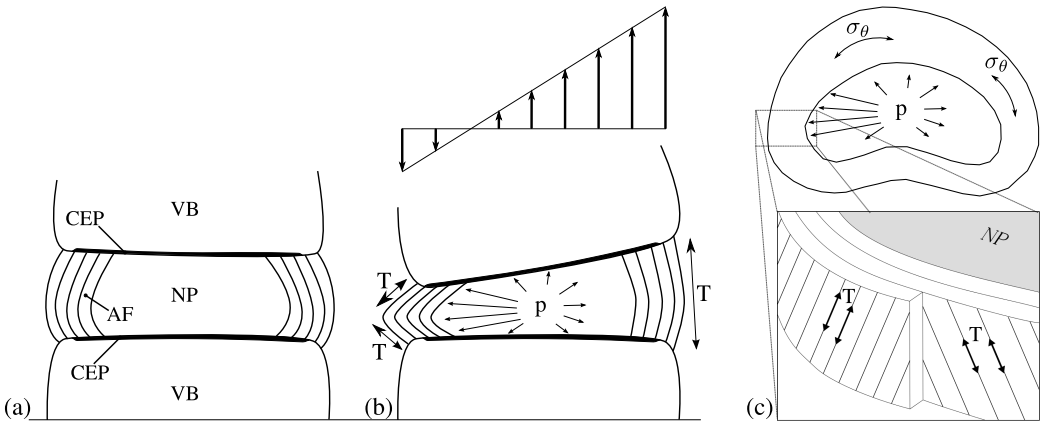

Figure II.4: Idealised disc response to bending: transverse section through the unloaded (a) and loaded (b) IVD, and mid-sagittal section (c)

side of the disc, while the fibres are directly loaded in tension on the tensile side (see right AF on Fig. II.4b). Torsion is resisted by fibres oriented in the direction of the rotation.

The mechanism described above illustrates the disc's response to fast loading (e.g. timescale to lift a weight, lacing a shoe ...). However, intervertebral discs exhibit creep under the prolonged compressive loading imposed over the course of a day, resulting from a slow fluid outflow through the endplates and the annulus; this is called the diurnal cycle. As the fluid is squeezed out, the hydrostatic pressure slowly reduces and the applied loads are gradually transfered to the solid matrix (Martinez et al., 1997), while the osmotic pressure increases. The daily amount of fluid expelled from a disc can represent 10-20% of its volume (McMillan et al., 1996), which can result in a reduction in stature of 15-25mm (Tyrell et al. (1985), Adams et al. (2006)). Hydration of the disc, which is a necessity of a healthy disc, is restored upon unloading (i.e. typically overnight), owing to osmotic pressure.

Osmotic pressure is a diffusive fluid flux induced by an ionic imbalance in the interstitial fluid, that stems from the presence of proteoglycans: the interstitial fluid (a saline solution), present inside and outside of the intervertebral disc, can be seen as an infinite supply of sodium (Na^+) and chloride (Cl^-) ions. In order to satisfy the electro-neutrality condition, an excess of sodium ions exists within the tissue to balance the negative charge of the proteoglycans, which are intertwined in the extracellular matrix. This imbalance of sodium ions induces fluid to flow from regions with lower solute concentrations (e.g. the outside of the IVD) to regions with higher solute concentrations, resulting in tissue dilation and allowing fluid to re-imbibe the tissues. The flow stops once the osmotic pressure and stresses in the solid matrix and collagen fibres are balanced. In practice, as the tissue deforms under complex loading, concentrations of proteoglycans evolve locally, in turn affecting local concentrations of sodium ions. This, together with a naturally non-uniform distribution of proteoglycans, results in a complex distribution of osmotic pressure in the disc. The osmotic pressure, which ranges between 0.1 and 0.3 MPa (Urban and McMullin (1988), Glover et al. (1991), Johannessen and Elliott (2005)), also participates in the intrinsic stiffness of the intervertebral disc.

II.3 Pathology and pain

Lumbar back pain has significant socio-economic impacts: prevalence rates have been reported to range between 12% and 35% at any one time (Raj, 2008), and 70% to

85% of the population in western countries experience back pain at least once in their life time (Andersson, 1999). It impairs people's well being and has dramatic costs on the society. In the UK alone, costs related to patients' treatment and care, as well as the engendered loss of productivity was estimated at £10.6 billion in 1998 (Maniadakis and Gray, 2000).

The health of the intervertebral disc relies on the fragile integrity of its various constituents. This requires an harmonious execution of the previously described mechanisms (e.g. diffusion, diurnal cycles). In this section, the most common manifestations of disc deterioration, whether histologic or structural, are presented together with their consequence in terms of pain. It will be shown that two or more of these phenomena are often linked, triggering what is referred to as cascade or snowball effects.

II.3.1 Structural failure

Failure mechanisms are difficult to predict as they highly depend on rate and posture (Veres et al., 2010), even if they generally result from abnormal loading. Herniation is a common internal disruption of the intervertebral disc, involving radial tearing extending from the nucleus pulposus to the annulus fibrosus and where nuclear matter is squeezed through the AF. It is a multi-stage process that can be initiated both at slow and fast rates (see Fig. II.5b). When the pressure is gradually increased, the fluid is given sufficient time to flow out of the disc, and local stretching of the AF takes place until failure occurs. Upon rapid loading, the nuclear matter is displaced over the full height of the disc resulting in tearing of the upper CEP. This first stage of internal disc disruption is called protrusion and only affects the inner AF without causing any noticeable outward bulging. In the next stage called extrusion, the nucleus is pushed to the outer boundary of the AF (see Fig. II.5a). The most severe case of herniation is called sequestration, which happens when the NP is fragmented outside of the IVD. However, in most cases, herniation remains contained as NP matter can break the weak inter-lamellar connection (Veres et al., 2008).

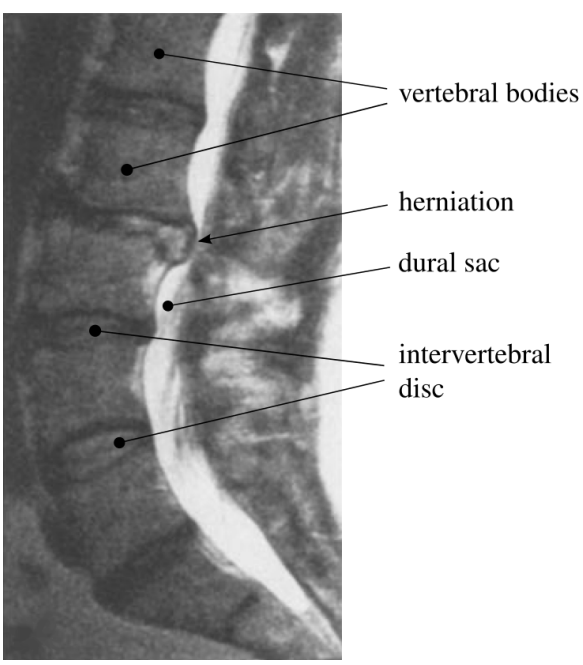

(a) MRI showing a herniated disc - Note that the patient was not experiencing pain (adapted from Van Goethem et al. (1996))

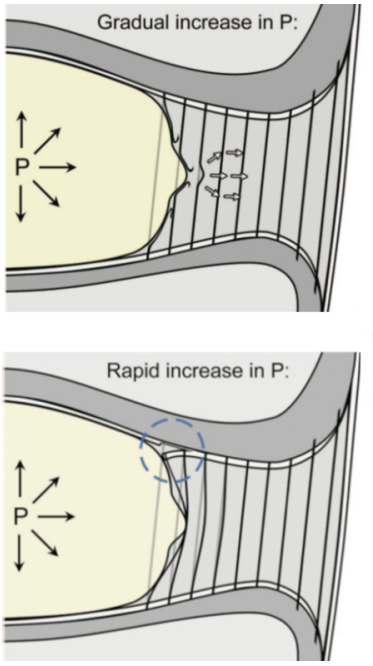

(b) Comparison of failure mechanisms for the IVD subjected to slow (top) and fast (bottom) hydrostatic loading (Veres et al., 2010)

Figure II.5: Disruption of the intervertebral disc

Another example of disc failure concerns the cartilaginous endplates, which are often thought of as the weakest link of the intervertebral disc. Sudden disc pressurisation can lead to fracture of the endplate (see Fig. II.6) resulting in nucleus material to breach into the vertebral body. This is known to cause progressive structural damages in the intervertebral disc (Adams et al., 2000) due to a variety of mechanisms. Indeed, CEP fracture hinders the diffusive fluid flow (Rajasekaran et al., 2004) and consequently the transport of metabolites. It also alters the load transfer: it was reported in Przybyla et al. (2006) that CEP failure can result in a 37% reduction in NP pressurisation and a 97% increase in AF local stress.

Figure II.6: CEP failure: NP material leaching into the upper vertebra (adapted from Adams et al. (2006))

II.3.2 Ageing

The endplates are one of the first constituents of the IVD to experience ageing. As early as the end of the second decade of life, the vascular content rooting from the vertebral bodies (and consequently a potential source of nutrients) reduces (Shankar et al., 2009). The CEP have also been reported to become thinner, to fissure and see their hyaline content increase Coventry (1969). Additionally, due to increased calcification the permeability of the endplate drops (this is called scoliosis), hindering the fluid flow and therefore the delivery of nutrients (Roberts et al., 1996).

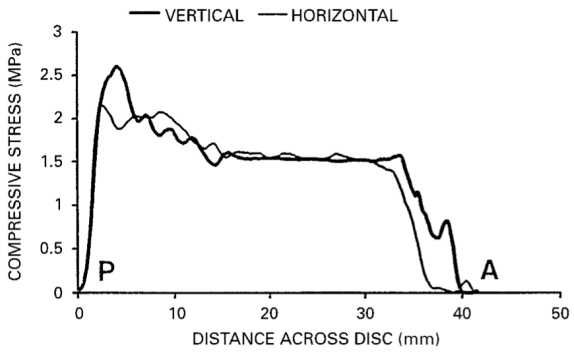

Figure II.7: Stress distribution in transverse plane of a 82 year old IVD subjected to 1kN compression (Adams et al., 1996b) , highlighting the emergence of stress concentrations on the posterior side

Ageing discs see their aggrecan content to become degraded, resulting in smaller fragments being more readily able to leach outside of the tissue (Urban and Roberts, 2003). Consequently, osmotic pressure decreases, together with the ability for the tissue to re-hydrate, resulting in a dryer nucleus that lost its ability to pressurise under loading and therefore evenly transfer loads. As Fig. II.7 shows, the region of NP and inner AF exhibiting hydrostatic pressure is reduced by 50% in diameter (Adams et al., 1996b), leading to higher compressive loads and peak stresses in the

annulus fibrosus.

The fibre content of the ageing NP also becomes denser and stiffer, with the type II collagen being replaced by type I (Shankar et al., 2009). Additionally, fissures commonly appear in the drier nucleus pulposus (Raj, 2008).

II.3.3 Degeneration

There is no unanimous definition of the term disc degeneration, which can probably be attributed to the lack of understanding of the phenomenon and its aetiology (Battie and Videman, 2006). Degeneration is an irreversible process, which compromises the structural integrity of the intervertebral disc. It proliferates as the balance between matrix synthesis and breakdown is impaired. Degeneration has been widely visually assessed using a 4-level grading system, which can be described quoting Adams et al. (1996b):

- Grade 1: the disc was white, and usually showed no signs of structural disruption to the annulus or vertebral body endplates. The distinction between the annulus and nucleus was obvious only on thin sagittal sections; in these the nucleus appeared to be gelatinous or even translucent.

- Grade 2: the disc was cream-coloured and usually showed no signs of structural disruption. The nucleus appeared to be fibrous and rather yellow, but was still soft. The concentric lamellae of the annulus were distinct and intact.

- Grade 3: There were signs of disruption of the annulus or adjacent endplates. The nucleus was fibrous, dry and often discoloured. The annulus usually contained fissures or splits, and small marginal osteophytes were often present around the rim of the vertebral body. The vertebral endplates were usually concave on the disc side.

- Grade 4: Severe disruption made it difficult to distinguish between annulus and nucleus. The disc was usually narrowed. The nucleus was often brown and fibrous and the annulus contained gross radial or circumferential fissures. The endplate was often damaged or depressed in the centre and marginal osteophytes were usually present.

The above description, together with the photographs of Fig. II.8a, highlight dehydration as one of the most prominent characteristic of degeneration. In fact, diurnal variations (i.e. fluid inflow at night, outflow during the day) are no longer observed in degenerated discs (Shankar et al., 2009), probably due to the fact that degenerated discs present reduced diffusion (Rajasekaran et al., 2004). This has recently allowed the use of non-invasive techniques to assess the level of degeneration of the disc: T2 relaxation time is a time measure that can be evaluated from MRI scans. It is sensitive to water content and the arrangement of the collagen network structure (Watanabe et al., 2007) and can therefore be used (Jim et al. (2005), Cheung et al. (2010)) to assess the level of degeneration of the disc (see Fig. II.8b).

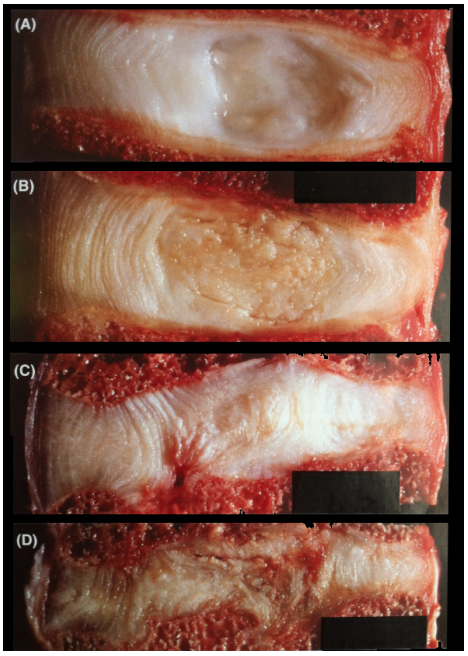

(a) Mid-sagittal section of four intervertebral discs (adapted from Adams et al. (2006))

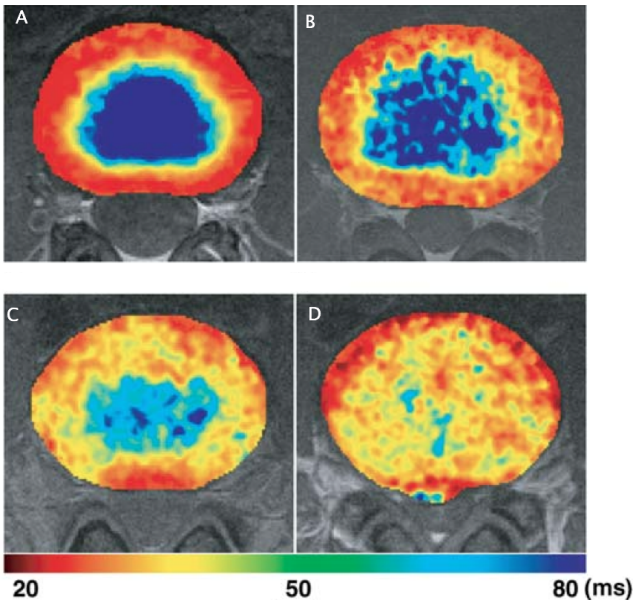

(b) Superior view of four intervertebral disc using axial T2 mapping (adapted from Watanabe et al. (2007))

Figure II.8: The four stages of disc degeneration: grade I (A), grade II (B), grade III (C) and grade IV (D)

Intervertebral discs never markedly stop evolving. For example (Coventry, 1969), the epiphyseal ring only reaches a full mature bond about the age of 20; the shape of the disc constantly adapts to the loading with for example the emergence of pronounced anterior and posterior bulges; the boundary between NP and AF becomes more distinct. Contrary to intuition, disc degeneration can start at early ages compared to that of other musculoskeletal tissues. It is reported in Miller et al. (1988), a publication gathering data from 16 studies -600 intervertebral discs- that about 15%

of people in their teens already have discs exhibiting signs of degeneration (grade II). This rate gradually increases to reach 93% for patients in their sixth decade (mostly grade II and III) and in nearly everyone aged 70 or above (more than 40% of which exhibit grade IV degeneration).

Degeneration has been linked with a number of factors. It was previously thought that degeneration could generally be explained by pathological factors such as trauma (i.e. one of the structural failure mechanisms described above, potentially disrupting the nutrient supply), body weight, occupational activities (e.g. daily exposure to heavy lifting or vibrations) or diet. Ageing has also been put forward to explain the origin of degeneration. However, in more recent publications, degeneration was found to be related to genetic predisposition more than 70% of the time (see Battie and Videman (2006) and references therein).

It is generally thought that degeneration is originally initiated by one of the aforementioned events (i.e. genetics, trauma, ageing), which locally compromises the integrity of the tissue and progresses to eventually affect the whole disc through a chain of events (often referred to as a cascade or snowball effect). For example, genetic factors or simply ageing, may cause a reduction in aggrecan content in the tissue (Urban and Roberts, 2003). Consequently, the disc is not able to maintain its hydration under loads due to a reduction in the osmotic pressure. This directly affects the load bearing mechanisms of the disc by reducing its ability to pressurise (Adams et al. (1996b) and Fig. II.7), altering fluid flow and nutrient exchange, reducing disc height and excessively increasing annulus bulging (Battie and Videman, 2006). The weakened disc then becomes more prone to further damages (Raj, 2008), in turn perpetuating the progression of the degenerative process.

II.3.4 Pain

The origins of back pain are still disputed (e.g. Raj (2008); Sitthipornvorakul et al. (2011) and references therein). Although the disc is avascular and aneural, branches of the spinal chord are wrapped around the outer AF. In a healthy disc, these sensory nerves are also found in the outer 3-4mm portion of the annulus (Shankar et al., 2009). However, it has been reported that depressurisation of the disc as well as the presence of radial annular tears allow for the ingrowth of nociceptive nerve endings (i.e. responsible for the feeling of pain) in the inner third of the AF and even the NP, presumably at the origin of pain-sensitisation (Freemont et al., 1997; Adams et al., 2010).

Naturally, the presence of nerves in the (degenerated) disc has been put forward as

to explain pain felt by symptomatic patients. However, it has been demonstrated that this cannot be the only cause of pain. A study undertaken by Boos et al. (1995) compared two groups of 46 patients, one symptomatic and the other a risk factor-matched asymptomatic group. The asymptomatic group comprises patients that are not experiencing any form of pain or discomfort. It was found that more than 70% of the asymptomatic patients exhibited some form of disc herniation.

Back pain is almost inevitably related to structural disruption; stress concentration exhibited in the pressure profiles (Adams et al. (2006) and references therein) have been related to pain (McNally et al., 1996). In the case of severe herniation, NP matter can stimulate nociceptive nerve endings and cause inflammation to the root nerve or even cause sciatica (sometimes called "pinched nerve"). Structural changes associated with degeneration adversely affect the behaviour of spinal structures adjacent to the disc (Raj, 2008) and predispose them to pain in the long term: narrowing of the spinal canal called spinal stenosis (a major cause of pain in the elderly Urban and Roberts (2003)), abnormal loading of the neural arch leading to osteoarthritis, muscle and ligament remodelling.

II.4 Conclusion

This chapter has presented a very general description of the intervertebral disc, from an engineering perspective, detailing the structure of the IVD as well as its internal mechanisms. These were presented together with the main pathologies and potential disruptions.

The degenerative process and its relation to pain are not fully understood. The objective of this thesis is to participate in the understanding of the disc's behaviour, both at short- and long-term time scales, by offering biologists and surgeons a different viewpoint on the tissue and potentially new data. This could have impacts in the following areas:

- In the case of a severely disrupted disc, implants are often considered. This can involve the replacement of the nucleus pulposus (e.g. Fig. II.9a) or the replacement of the whole intervertebral disc (e.g. Fig. II.9b-II.9c). It is crucial to understand the behaviour of the real disc, which includes stability, ranges of motion and load transfer, in order to design a replacement device that will be able to mimic the original structure.

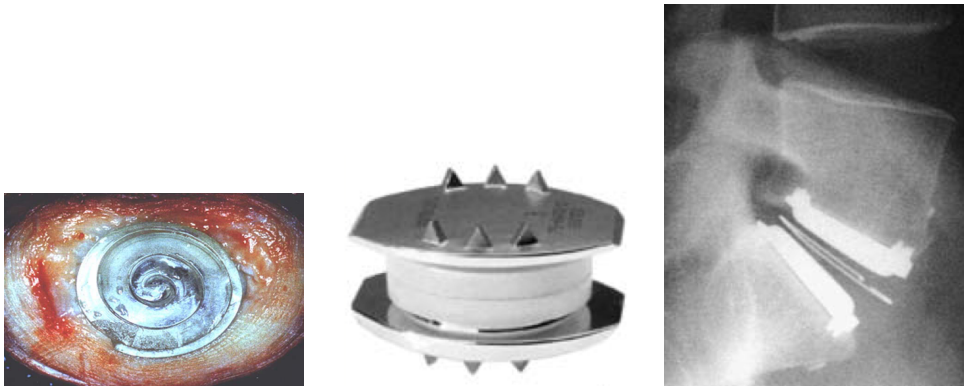

(a) (b) (c)

Figure II.9: (a) Nuclear replacement (Goins et al., 2005) (b) A design of IVD full disc replacement (adapted from Geisler et al. (2004)) (c) Radiography of the implanted disc under flexion (adapted from Geisler et al. (2004))

- Another surgical intervention to treat back problem is segment fusion (e.g. Fig. II.10). This involves the insertion of screws in two or more adjacent vertebrae, that are rigidly connected and relies on the surgeon's experience to choose the position of the screws and the number of segments to fuse. A complete patient specific spinal model could help the surgeon optimise its decision process. Numerical models could also help understand why fusion is often associated with stenosis and degeneration of adjacent discs (Lee, 1988).

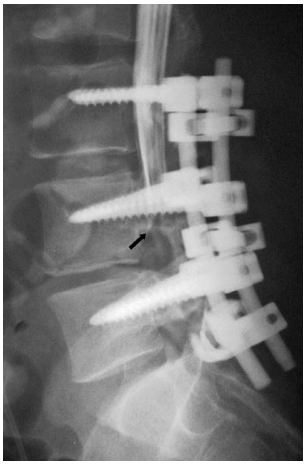

Figure II.10: Lumbar fusion: pedicle screws are positioned in vertebrae surrounding the symptomatic region and fused together with a metallic rod (Kreichati et al., 2006)

- Although it seems that exercise impacts the movements of nutrients (see Raj (2008) and references therein) and their concentrations in the tissue, the benefits

of physical activity on back pain are still under conflict (see results of 13 studies compared in Sitthipornvorakul et al. (2011)). Computational models could participate in the understanding of the fluid flow mechanisms and nutritional pathway, and potentially design patient specific exercise to help slow down degeneration.

- Mechano-biologists are trying to understand how stresses affect the biology of the tissue (e.g. matrix synthesis). Computational models represent a non-invasive alternative to estimate local stress levels within the tissue, as valuable information is hard to obtain *in-vivo*.

The observations made in this chapter are an essential prerequisite, which will enable the definition of a modelling framework in the following chapter.

Chapter III

The biphasic swelling model

In this chapter, historical highlights of the theory of porous media are presented, followed by a literature review on the trends in soft tissue modelling. The proposed modelling strategy is discussed in the context of the intervertebral disc, with particular attention to the osmotic effects, the strain-dependent permeability and rate-dependent phenomena. Finally, the theory of porous media is derived for a biphasic medium, enriched with swelling capabilities.

III.1 Motivations for a biphasic swelling model

In the following, the preference for a biphasic swelling model as a framework to study the mechanical behaviour of the intervertebral disc is motivated. First, developments regarding the modeling of porous media and more specifically soft tissues are reviewed. Second, in light of the previous chapter, key features that the formulation must exhibit in order to meet the objectives are identified.

III.1.1 Modelling of porous media: a few milestones

Although it is not the intention here to recount the historical developments of multiphasic theories (other authors have written excellent contributions on the topic, e.g. Atkin and Craine (1976), de Boer (1996, 1998, 2000, 2005), de Boer and Ehlers (1988), Ehlers (2002), Karajan (2009)), a selection of milestones that are particularly relevant to this work is presented.

The first publications to treat porous medium as mixtures of several constituents can be traced back to the mid-nineteenth century with, for example Fick (1855) studying

diffusion of mixtures through porous membranes and Darcy (1856) who was interested in fluid flow through porous solids. The first fundamental postulate of mixture theory was established in another publication on diffusion Stefan (1871) (see de Boer (1996) for a translation from German):

> "If the true processes in a mixture should be calculated, it is not sufficient anymore, to consider the mixture as a uniform body as common mechanics does; equations must be set up which contain the condition of equilibrium and the laws of motion for every individual constituent in the mixture"

This is a significant concept in mixture theory, which allows one to consider that at any time, each particle of the multi-phase continuum can be thought of as the superposition of all its constituents.

Diffusion models were augmented by the addition of a solid phase during the twentieth century with a main focus on soil mechanics. Terzaghi with contributions on saturated deformable medium and the introduction of the effective stress (Terzaghi (1925, 1923)), and Biot with the development of poro-elasticity, e.g. Biot (1941, 1956, 1972), were two major contributors. Other considerable milestones in the development of mixture theories are attributed to Truesdell: in Truesdell and Toupin (1960), it was stipulated that the governing equations of the mixture should take the same form as the ones of its constituents. He also authored the metaphysical principles in Truesdell (1984) [1].

It is also generally admitted, cf. de Boer (1996) and Ehlers et al. (2006), that the theory of porous media (TPM) is based on the theory of mixtures enriched with the concept of volume fractions as described in Morland (1972), which allows us to define the mixture as a smeared average of its constituents.

Another key contributor in the developments of TPM is Bowen, in particular for introducing restrictions on the entropy inequality (Bowen, 1967) (refining Truesdell (1957) where the local balance equations of mass, momentum and energy were initially introduced) and also his work on compressible and incompressible mixtures, cf. Bowen (1982, 1980).

Bowen's work on mixture theory and Biot's development of poro-elasticity represent the theoretical basis for most of the modern models of soft tissues (cartilage,

[1] "Truesdell's metaphysical principles": 1) All properties of the mixture must be mathematical consequences of properties of the constituents; 2) So as to describe the motion of a constituent, we may in imagination isolate it from the rest of the mixture, provided we allow properly for the actions of the other constituents upon it; 3) The motion of the mixture is governed by the same equations as is a single body.

intervertebral disc, brain, eye ...).

III.1.2 A short review of soft tissue models

It has long been recognised that the intervertebral disc - and soft tissues in general - cannot simply be modelled as linear elastic solids: more advanced models are required to capture the salient features and internal mechanisms of the disc.

In early full-disc models, the nucleus pulposus was considered to behave either like a viscous solid in order to replicate the fluid viscous drag as it flows through the solid matrix (e.g. Wang et al. (1997)) or like a fluid and as such modelled by an hydrostatic contribution, therefore neglecting tissue deformations. Non-porous models of the nucleus were initially linear elastic, e.g. Natarajan et al. (1994), and evolved to more complex models including finite deformations and the anisotropy of the annulus fibrosus. The contribution of fibres was initially represented by non-linear spring elements, e.g. Shirazi-Adl et al. (1986b,a) Shirazi-Adl (1994) and later refined with continuum models, e.g. Elliott and Setton (2000) (small strain) and Eberlein et al. (2001, 2004) (hyperelastic).

In the meantime, other researchers focused on developing understanding of the fluid-solid interaction and the electro-mechanical coupling (proteoglycans, anion, cations, etc.). In Mow et al. (1980), a biphasic model based on mixture theory was derived for articular cartilage for the small deformation regime, and is often seen as the precursor of all multi-phase models. It was later extended to take into account the strain-dependency of the permeability (Lai et al. (1981); Holmes (1985)) and finite deformations (Kwan et al. (1990); Suh et al. (1991)). The biphasic model was then enhanced to include charge-induced phenomena. The first model of the kind is the tri-phasic model of Lai et al. (1991) derived for infinitesimal strains. It describes both the ion diffusion and convection: an ionic phase (including anions and cations) is added to the negatively charged solid and the neutral fluid by means of ionic balance of concentrations. Note that the swelling due to chemical expansion, a load induced by charge-charge repulsion was also included. The models comprise three primary fields: displacements, chemical potentials of both the neutral salt and the interstitial fluid. In order to take electrical fluxes into account, the triphasic model was later extended by Snijders et al. (1995), Huyghe and Janssen (1997), Frijns (2000) and more recently by Chen et al. (2006) to a quadri-phasic finite deformation model. This time anions and cations are accounted for as separate phases. This model was implemented in 1D by Frijns et al. (1997) (and tested against uni-axial experiments).

Although van Loon et al. (2003) made use of the quadri-phasic model in 3D, most

publications have been restricted to 1D or 2D isotropic simulations, probably due to a prohibitive model size and the impossibility to solve for accurate 3D meshes (the quadri-phasic has 15 governing equations in 3D, resulting from the mass and momentum balances for each constituent, as well as the neutrality and saturation conditions).

Following this race to include the highest number of phases in the governing equations, a more recent trend has been, on the contrary, to reduce the number of independent phases, yet without compromising on a given model's capabilities. The "swelling models", based on the so-called Lanir hypothesis (Lanir, 1987) that will be described in details in Sec. III.4, neglect the diffusive effects of the almost volume-free proteoglycans and constitutively model the osmotic effects. This approach was compared with the tri-phasic one in Wilson et al. (2005a) with promising results and used by other contributors, e.g. Schroeder et al. (2006, 2007) and Ehlers et al. (2006, 2008). Note that the following chapters are based on this approach.

Poro-elasticity, a phenomenological approach to the modeling of porous media, is the other major framework that has been used to analyse soft tissues (see Sec. III.1.1). Although it has received criticism because it is not derived from thermodynamical principles (e.g. de Boer (1996, 2005), Ehlers et al. (2008, 2009)), it shares some similarities with the theory of mixture. For example Bowen (1982) shows that poro-elasticity can be retrieved from linearisation of the biphasic model of Mow et al. (1980). A similar comparison is also drawn in Simon (1992), where the model is also extended to finite deformations, based on Biot (1972). In Simon et al. (1996), a poro-elastic framework that includes diffusive and swelling effects is presented and compared with the tri-phasic model of Lai et al. (1991). Cowin (1999) advocates that the difference between poro-elasticity and mixture theories merely lies in the homogenisation process. Although the present work will be focusing on mixture theory, it is worth mentioning some of the first full lumbar models based on poro-elasticity. Simon actively published on the topic with an axi-symmetric linear poro-elastic model Simon et al. (1985), extended to include swelling in Simon et al. (1996). Laible et al. (1993) proposed a 3D swelling linear elastic model, Argoubi and Shirazi-Adl (1996) proposed a strain-dependent linear elastic motion segment model where the detailed geometry includes facet joints. Li et al. (1999, 2003) proposed an axi-symmetric poro-elastic model for finite deformation, including strain-dependent permeability but leaving osmotic effects aside, while anisotropy was modelled with springs. Other studies have used poro-elastic models to model the IVD, including Lanir-type swelling, e.g. Hsieh et al. (2005) with linear axi-symmetric rebar elements for annulus, Natarajan et al. (2007) for a nonlinear model of a motion segment. Models such as Iatridis et al.

(2003) and Olsen et al. (2004) also include concentration gradients.

III.1.3 Objectives and modelling strategy

One of the most crucial steps in computational modeling effectively takes place before the modeling itself: the selection of a framework that can reasonably be trusted to produce the sought results. This step, which cannot be done arbitrarily, requires a clear definition of the objectives one wants to achieve. In the special case of the intervertebral disc and in view of observations made in Chapter II, the modelling strategy is defined by finding the best compromise between the following points:

- *The physics.* All physical phenomena taking place in the intervertebral disc cannot realistically be accounted for. In order to identify the salient mechanisms that predominantly affect the mechanical behaviour of the intervertebral disc, modelling scales (both in time and space) need to be defined.

- *The material parameters.* Experimental work on soft tissues is particularly difficult. This is due on the one hand to the fact that only a limited number of experiments can be carried out *in-vivo*, and on the other hand to the fact that the properties of soft tissues evolve once they are taken from the natural environment. It is therefore essential to not only limit the number of material parameters, but also choose constitutive models that reflect the nature of the media. This indeed ensures that a physical interpretation of the material parameters is possible and eases the design of universal experimental protocols.

- *The size of the mathematical problem.* The IVD has a very intricate geometry that needs to be modelled accurately, requiring fine three dimensional meshes. It is important to keep the system of equations at a reasonable size. This point, which is highly related to the first one, plays an essential role in the choosing of the governing equations (and variables) that are essential to describe the disc's behaviour.

In the present work, the aim is to perform a quasi-static macro-scale analysis of the disc. Our interest lies in the understanding of the biomechanical behaviour of the IVD, e.g. the deformations and load transfer mechanisms within the disc under physiological loading. This implies that small-scale mechanisms such as nutrients or molecular flow will not be investigated. The description in Chapter II about the nature of the intervertebral disc (i.e. loading mechanisms and the biological constituents) enables the disc to be considered from a modelling perspective: in a

simplified manner, the IVD can be seen as a mixture of interacting constituents, comprised of an extra-cellular matrix of collagen fibres saturated by a charged interstitial fluid, with proteoglycans playing the essential role of offering swelling capabilities to the disc by regulating its fluid content.

As far as the solid part is concerned, the disc undergoes large strains and exhibits strong anisotropy in the annulus fibrosus. Although strains can physiologically reach up to 10%, soft tissue can sometimes exhibit a linear elastic behaviour up to 20% (small) strain under equilibrium conditions (Holmes et al., 1985); the necessity to use finite deformation theory is justified by the fact that high deformations during moderate to fast loading may occur *locally* (Holmes (1986), Wang et al. (2009)). This is usually due to the coupling with the nonlinear fluid flow (see Sec. III.5 and V.5).

In light of the previous points, a biphasic swelling model is chosen for the intervertebral disc. It offers an acceptable balance between simplicity (limited number of degrees of freedom, few material parameters) without neglecting the most salient features of the IVD: coupling between the solid and the fluid, osmotic effects, strain dependent phenomenon, etc. Furthermore, the theory of porous media offers a very modular framework (Ehlers et al., 2008). As the mixture is defined as the superposition of its constituents, it makes it straightforward to enhance the physics of the model (e.g. mass exchange, chemical reactions, viscosity or electrochemical phenomena), or material laws (e.g. anisotropy or viscosity) when needed.

III.2 The TPM framework

The theory of porous media (TPM) is a homogenized macroscopic representation of the porous medium. Although it will only be used to model the intervertebral disc in the following chapters, it has been successfully used for other applications (e.g. brain, cartilage, soil). It is a continuum-based approach, which fully couples the fluid and solid phases. It overcomes the difficulty of modelling the complex internal geometry of the microstructure by using the concept of volume fractions to "smear" the constituent properties over a control space to obtain an *effective* homogeneous representation of the overall mixture: the averaging is done at the micro level whereas the mechanical and thermo-dynamical equations are written at the macro level (de Boer, 1996). In this section, the general definitions and concepts of the theory of porous media are presented. The special case of a two-constituent mixture (i.e. biphasic) comprised of a fluid F and a solid S is derived. The model is based on Almeida and Spilker (1998), de Boer (1998) and Ehlers (2002). It is worth

mentioning at this stage that in the context of the IVD, the solid phase is comprised of the matrix of collagen fibres and the proteoglycans.

Firstly, the following simplifying assumptions are made in the current model:

- the constituents are immiscible, i.e. they are not forming an homogeneous mixture when mixed together
- no density supply is allowed to the closed system, i.e. neither growth nor resorption of the tissue is taking place
- the constituents are not reacting chemically
- the medium is fully saturated, i.e. the whole space is occupied by either of the constituents
- quasi-static loading conditions: inertial terms are ignored given the small size of the disc
- isothermal conditions and adiabatic behaviour
- both constituents are intrinsically incompressible (see for example Bachrach et al. (1998) and Miller (2001) and references within)

The most fundamental concept of mixture theory - established as early as Stefan (1871)- asserts that at any time t and at each spatial point $\mathbf{x}$ of the continuum, particles of both constituents α coexist (see Fig. III.1). Therefore any elementary volume dv is simultaneously occupied by both phases and is split into partial elementary volumes dv^α. The volume fractions can then be defined as:

$$n^\alpha(\mathbf{x},t) = \frac{dv^\alpha}{dv}(\mathbf{x},t) \qquad \alpha = \{S,F\} \tag{III.2.1}$$

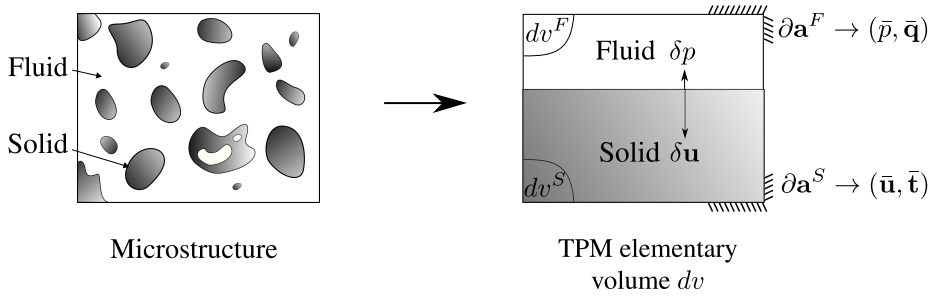

Figure III.1: The TPM representation with volume fraction averaging (right) of the microstructure (left): at each material point, fluid and solid coexist. Displacement and pressure fields are coupled.

Assuming that there is no gas in the mixture (which is relevant for the IVD), the saturation condition, sometimes referred to as the equipresence principle, is:

$$n^S + n^F = 1 \tag{III.2.2}$$

The useful relationship between the apparent density ρ^α and true density ρ_T^α of each constituent is:

$$\rho^\alpha = \frac{dm^\alpha}{dv} = \frac{dm^\alpha}{dv^\alpha}\frac{dv^\alpha}{dv} = \rho_T^\alpha n^\alpha \tag{III.2.3}$$

From a kinematic point of view, Stefan's concept together with *"Truesdell's metaphysical principles"* (see Footnote 1 on page 20) imply that each constituent α of the mixture can be described by its own and independent motion $\boldsymbol{\chi}^\alpha$. The motion can be thought of as the trajectory in time of a given particle. Eq. III.2.4 shows that at any given time t, the motion is a function relating the position $\mathbf{X}^\alpha$ of that particle in the reference configuration, to the position of the same particle in the current configuration $\mathbf{x}^\alpha$.

$$\mathbf{x}^\alpha = \boldsymbol{\chi}^\alpha\left(\mathbf{X}^\alpha, t\right) \tag{III.2.4}$$

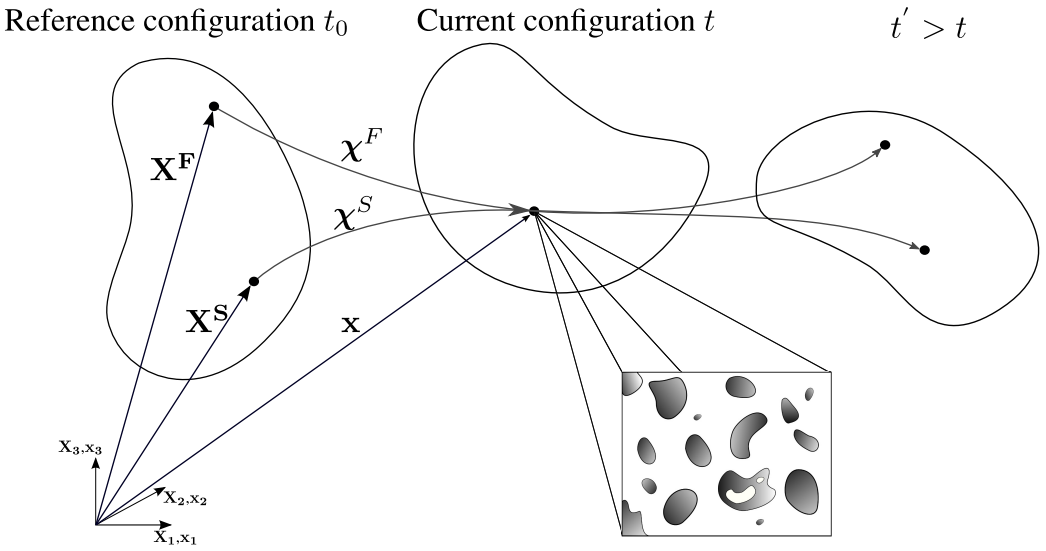

Figure III.2: Kinematics of the biphasic model

The reference configuration, often chosen as the undeformed state of the continuum, is an arbitrary initial configuration at time t_0. At time t, the deformed body is referred to as the current configuration. The position $\mathbf{x}$ in the current configuration

represents a mixture's elementary volume made of fluid particles (in proportion n^F) that were occupying the position $\mathbf{X}^F$ in the reference configuration, and solid particles (in proportion n^S) that were occupying the position $\mathbf{X}^S$ in the reference configuration. The particle's position history is illustrated on Fig. III.2.

The definition of the position field enables us to define displacements and velocities, two fields that will turn useful in the following derivations. In finite deformation theory, each quantity can be expressed either in the reference configuration or in the current configuration. In the Eulerian description (or sometimes called the spatial description), a field is characterised with respect to the current coordinates system $\mathbf{x}^\alpha$. For example, the Eulerian description of the displacements is:

$$\mathbf{u}^\alpha\left(\mathbf{x}^\alpha, t\right) = \mathbf{x}^\alpha - \mathbf{X}(\mathbf{x}^\alpha, t) \tag{III.2.5}$$

The above definition describes the displacements that are taking place at the specific position $\mathbf{x}^\alpha$ in the current configuration. It can be interpreted as follows: at the position $\mathbf{x}^\alpha$ in the current configuration lies a particle that was located at $\mathbf{X}(\mathbf{x}^\alpha, t)$ in the reference configuration and displaced by $\mathbf{u}^\alpha\left(\mathbf{x}^\alpha, t\right)$.

For the Lagrangian description (or sometimes called the material description), a field is described with respect to the reference coordinates $\mathbf{X}^\alpha$. Similarly, the Lagrangian description of the displacements, tracking the displacements of the particle $\mathbf{X}^\alpha$, is:

$$\mathbf{U}^\alpha\left(\mathbf{X}^\alpha, t\right) = \mathbf{x}^\alpha(\mathbf{X}, t) - \mathbf{X}^\alpha \tag{III.2.6}$$

Subsequently, the velocity field $\mathbf{v}^\alpha$ is defined for each constituent:

$$\mathbf{v}^\alpha = \frac{\partial \boldsymbol{\chi}^\alpha}{\partial t} \tag{III.2.7}$$

It is also useful to define the material time derivative with respect to the motion α, which measures the time rate of change of a quantity $(\bullet)$. When this quantity is expressed in the current configuration, it takes the form:

$$\frac{D^\alpha}{Dt}\left(\bullet\right) = \frac{\partial}{\partial t}\left(\bullet\right) + \frac{\partial}{\partial \mathbf{x}}\left(\bullet\right) \cdot \mathbf{v}^\alpha \tag{III.2.8}$$

In the above equation, the first term corresponds to the rate of change of the quantity $(\bullet)$ experienced by the particle when its spatial position is fixed while the second term accounts for the convective change of that quantity resulting from the motion of the same particle.

The gradient of deformation $\mathbf{F}_S$ of the solid is a crucial measure in finite deformation analysis, as it relates the infinitesimal line $d\mathbf{X}^S$ in the reference configuration to its deformed state $d\mathbf{x}^S$ in the current configuration. It is defined as the material gradient of the position $\mathbf{x}^S$ (see Eq. III.2.9), i.e. the gradient with respect to the coordinates system in the reference configuration $\mathbf{X}$. It should also be noted that $\mathbf{F}_S$ also controls the deformation of the proteoglycans, which are considered attached to the solid skeleton.

$$\mathbf{F}_S = \mathrm{Grad}\,\mathbf{x}^S = \frac{\partial \mathbf{x}}{\partial \mathbf{X}^S} \tag{III.2.9}$$

In the above, the material gradient is denoted Grad with upper case G. In the following, the spatial gradient (i.e. derivative with respect to the coordinate system of the current configuration $\mathbf{x}$) is denoted grad with a lower case g. Similar notations will be used for the divergence operator, Div and div.

Let us now define an elementary volume of mixture delimited by the porous solid in the reference configuration (cf interpretation on Fig. III.3). This volume can be thought of as delimited by infinitesimal segments of solid constituent and can be calculated as: $dV = (d\mathbf{X}_1^S \times d\mathbf{X}_2^S) \cdot d\mathbf{X}_3^S$. Note here that, although the elementary volume dV is delimited by the solid phase, $dV \neq dV^S$ as dV also encompasses some fluid.

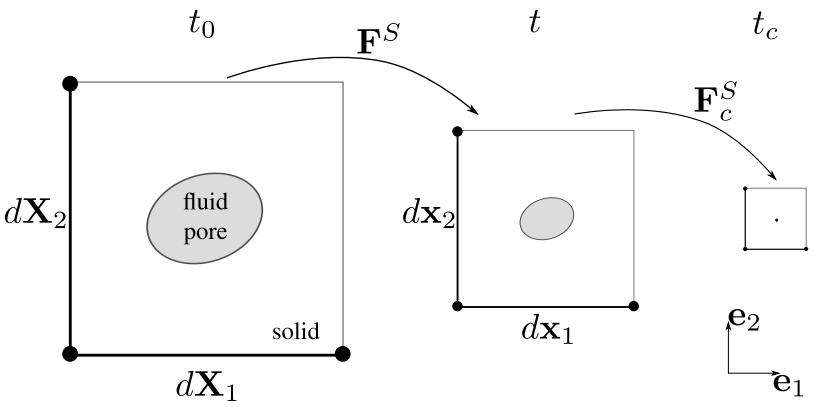

Figure III.3: 2D illustration of the volume change of the porous solid between the reference configuration (time t_0) and the current configuration (time t). The compaction point is represented at time t_c

In the current configuration, the volume dV is mapped to $dv = (d\mathbf{x}_1^S \times d\mathbf{x}_2^S) \cdot d\mathbf{x}_3^S$. If the elementary segments can be chosen, without loss of generality, to be aligned with the orthogonal reference system ($\mathbf{e}_1$,$\mathbf{e}_2$,$\mathbf{e}_3$), it is possible to show using the transformation $d\mathbf{x}_i^S = \mathbf{F}_S d\mathbf{X}_i^S$ that:

$$dv = JdV \qquad \text{where} \quad J = \det \mathbf{F}_S \tag{III.2.10}$$

This means that the determinant of the gradient of deformation of the solid J can be used to map elementary volumes of mixture between the current and the reference configurations. It is important to realise that intrinsic incompressibility of each constituent does not imply incompressibility of the mixture as fluid is allowed to leave the elementary volume. This also establishes the existence of a compaction point, illustrated by $\mathbf{F}_c^S$ in Fig. III.3 when all the fluid has left the mixture, that is reached when J is equal to the solid volume fraction in the reference configuration dv^S/dV .

Finally, it proves convenient to describe the fluid velocity as a velocity relative to the solid constituent, leading to the introduction of the seepage velocity $\mathbf{w}$ (as illustrated on Fig. III.4):

$$\mathbf{w} = n^F \left(\mathbf{v}^F - \mathbf{v}^S \right) \tag{III.2.11}$$

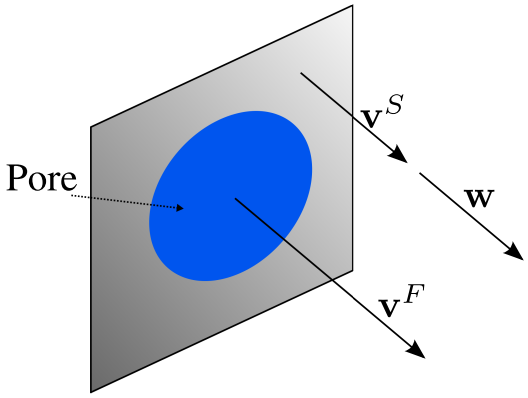

Figure III.4: Seepage illustration

It is interesting to realise that as a result of the "smearing" introduced by the mixture theory, the seepage velocity $\mathbf{w}$ represents a macro-level average of the fluid velocity with respect to the solid phase rather than an actual fluid velocity at the scale of the tissue pores (Cowin, 1999).

III.3 Balance relationships

Stemming from concepts found in Truesdell and Toupin (1960), TPM is built on the assumption that the mixture can be seen as the superposition of its constituents. Furthermore, the governing equations of the mixture as a whole must take the same

form as those of each constituent. To this end, the relative contribution of each constituent of the mixture is accounted for, weighed by its corresponding volume fraction. In the following sections, the governing equations of each constituents are derived and combined together using the concept of volume fractions in order to obtain the governing equation of the total mixture.

III.3.1 Balance of linear momentum

The balance of linear momentum, first expressed for each constituent independently, is derived in the current configuration. The rate at which momentum is locally transmitted by one constituent to the other is accounted for with the vector of momentum supply $\mathbf{p}^\alpha$. The stress $\mathbf{T}^\alpha$ is called apparent stress, because it has the unit of a force per unit *mixture area* (i.e. not unit area of constituent α). $\mathbf{g}$ is the gravity acceleration.

$$\operatorname{div}\left(\mathbf{T}^\alpha\right) + \mathbf{p}^\alpha + \rho^\alpha \mathbf{g} = \rho^\alpha \frac{D^\alpha \mathbf{v}^\alpha}{Dt} \qquad \alpha = \{S, F\} \tag{III.3.1}$$

As we are focusing on quasi-static problems, and ignoring wave propagation through the tissue, the inertial terms are neglected. The balance of linear momentum of the whole mixture is obtained by summation of Eq. III.3.1 over both constituents, yielding:

$$\operatorname{div}\left(\mathbf{T}^F + \mathbf{T}^S\right) + \mathbf{p}^F + \mathbf{p}^S + \left(\rho_T^F n^F + \rho_T^S n^S\right)\mathbf{g} = \mathbf{0} \tag{III.3.2}$$

As previously mentioned, Truesdell's third metaphysical principle implies that the sum over all constituents of the partial balance relations should take the same form as the balance of the single-phase material, that is for the balance of momentum:

$$\operatorname{div}\mathbf{T} + \rho\mathbf{g} = \mathbf{0} \tag{III.3.3}$$

As a direct consequence, it can be identified from Eq. III.3.2 and Eq. III.3.3 that:

$$\mathbf{p}^F = -\mathbf{p}^S \tag{III.3.4}$$

In an attempt to further simplify the problem, the body forces are neglected in comparison to other forces. This offers the advantage of cancelling the volume fractions from the system of equations and consequently the need to input an initial porosity in the problem. Finally, the balance of linear momentum is:

$$\operatorname{div}\left(\mathbf{T}^F + \mathbf{T}^S\right) = \mathbf{0} \tag{III.3.5}$$

III.3.2 Balance of mass

In a similar fashion to the balance of momentum, the balance of mass is first expressed for constituent α:

$$\frac{\partial \rho^\alpha}{\partial t} + \operatorname{div}\left(\rho^\alpha \mathbf{v}^\alpha\right) = 0 \qquad \alpha = \{S, F\} \tag{III.3.6}$$

The balances of mass of both constituents are then superimposed. Using Eq. III.2.3 and the assumption of intrinsic incompressibility (i.e. the true density ρ_T^α is constant), the balance mass of the whole mixture can be written as:

$$\frac{\partial\left(n^S + n^F\right)}{\partial t} + \operatorname{div}\left(n^S \mathbf{v}^S + n^F \mathbf{v}^F\right) = 0 \tag{III.3.7}$$

The saturation condition (Eq. III.2.2) together with the definition of the seepage velocity (Eq. III.2.11) mean that the balance of mass of the mixture can be simplified:

$$\operatorname{div}\left(\mathbf{v}^S + \mathbf{w}\right) = 0 \tag{III.3.8}$$

In the context of the constituents' intrinsic incompressibility, as solid matter can neither enter nor leave the mixture elementary volume defined on the solid matrix (see discussion at the end of Sec. III.2), Eq. III.3.8 shows that fluid is squeezed out when the elementary volume is compressed and flows back in when it expands. This implies that the volume change of the mixture is directly related to the flux of fluid relative to the solid, but also that J measures the amount of fluid flowing from and into the mixture.

III.3.3 Thermodynamical and constitutive considerations

This section derives the entropy and energy balances of the mixture and presents how previous assumptions affect the model's constitutive relationships. The derivation, largely based on principles established in Truesdell et al. (1965) and Bowen (1980), is, for example, presented in de Boer (1996), Ehlers (2002) and Karajan (2009) and references therein.

The first law of thermodynamics imposes the rate of internal energy $\mathcal{E}$ to be equal to the sum of the rates of mechanical and thermal work. In the context of mixture theory, the first law is written in the local form for each constituent α in Eq. III.3.9. The rate of mechanical energy is expressed as a function of the apparent stress $\mathbf{T}^\alpha$ and the spatial velocity gradient $\mathbf{l}^\alpha = \operatorname{grad} \mathbf{v}^\alpha$, while the rate of thermal work depends on the heat flux $\mathbf{q}^\alpha$ and the rate of external heat supply r^α. The extra terms $\mathbf{p}^\alpha \cdot \mathbf{v}^\alpha$ and e^α are specific to inter-phase energy exchanges; they respectively account for the rate of momentum and energy supply transmitted by constituent α to the other constituent.

$$\rho^\alpha \frac{D^\alpha \mathcal{E}^\alpha}{Dt} = \mathbf{T}^\alpha : \mathbf{l}_\alpha - \operatorname{div}\mathbf{q}^\alpha + \rho^\alpha r^\alpha - \mathbf{p}^\alpha \cdot \mathbf{v}^\alpha + e^\alpha \tag{III.3.9}$$

The second law of thermodynamics postulates that the total production of entropy of a closed system cannot be negative. The production of entropy $\hat{\eta}^\alpha$ is defined as the difference between the rate of change of entropy η^α and the rate of entropy input Q^α (θ^α is temperature of the constituent α), which is written for the mixture:

$$\begin{aligned} \hat{\eta} = \sum_\alpha \hat{\eta}^\alpha = \sum_\alpha \left(\rho^\alpha \frac{D^\alpha \eta^\alpha}{Dt} - Q^\alpha \right) \geq 0 \\ \text{with} \quad Q^\alpha = \operatorname{div}\left(\frac{-1}{\theta^\alpha} \mathbf{q}^\alpha \right) + \frac{1}{\theta^\alpha} \rho^\alpha r^\alpha \end{aligned} \tag{III.3.10}$$

Introducing the Helmhotz free-energy ψ^α as a function of the internal energy and the entropy:

$$\psi^\alpha = \mathcal{E}^\alpha - \theta^\alpha \eta^\alpha \tag{III.3.11}$$

allows to perform the Legendre transformation. Using Eq. III.3.9 and Eq. III.3.11 while making the assumption of an isothermal (θ^α = constant) process allows to rewrite the Clausius-Plank inequality Eq. III.3.10 as:

$$\sum_\alpha \left(\mathbf{T}^\alpha : \mathbf{l}_\alpha - \mathbf{p}^\alpha \cdot \mathbf{v}^\alpha - \rho^\alpha \frac{D^\alpha \psi^\alpha}{Dt} \right) \geq 0 \tag{III.3.12}$$

Note that in the same manner as in previous sections, the principle of mixture stating that the governing equations of the mixture should take the same form as those of a single constituent has been used to impose that $\sum_\alpha e^\alpha = 0$, (see for example de Boer (2005)).

The introduction of the volume fractions has the consequence of introducing one extra variable for each phase of the mixture, which implies that the "closure problem" is not

fulfilled (de Boer, 1998), i.e. a greater number of unknowns than equations available. In order to overcome this problem, the saturation condition (Eq. III.2.2) is imposed as a kinematic constraint onto the entropy inequality, introducing a Lagrange multiplier p:

$$p \frac{D^S}{Dt} \left(n^S + n^F \right) = 0 \tag{III.3.13}$$

Using the definition of the material time derivative (Eq. III.2.8), and the identity $\operatorname{div}(\varphi \mathbf{u}) = \varphi \operatorname{div} \mathbf{u} + \mathbf{u} \cdot \operatorname{grad} \varphi$ as well as the saturation condition, Eq. III.3.13 yield:

$$- p \left(n^S \operatorname{div} \mathbf{v}^S + n^F \operatorname{div} \mathbf{v}^F + \operatorname{grad} n^F \cdot \mathbf{w} \right) = 0 \tag{III.3.14}$$

Since $\operatorname{div} \mathbf{v}^\alpha = \mathbf{l}_\alpha : \mathbf{I}$, adding Eq. III.3.14 to Eq. III.3.12 and remembering that $\mathbf{p}^S = -\mathbf{p}^F$ leads to:

$$\underbrace{\left(\mathbf{T}^S + n^S p \mathbf{I} \right)}_{\mathbf{T}_E^S} : \mathbf{l}_S + \underbrace{\left(\mathbf{T}^F + n^F p \mathbf{I} \right)}_{\mathbf{T}_E^F} : \mathbf{l}_F - \underbrace{\left(\mathbf{p}^F - p \operatorname{grad} n^F \right)}_{\mathbf{p}_E^F} \cdot \mathbf{w} - \sum_\alpha \rho^\alpha \frac{D^\alpha \psi^\alpha}{Dt} \geq 0 \tag{III.3.15}$$

The final expression of the Clausius-Plank inequality (Eq. III.3.15) allows to introduce the concept of effective stress:

$$\mathbf{T}^\alpha = \mathbf{T}_E^\alpha - n^\alpha p \mathbf{I} \tag{III.3.16a}$$

$$\mathbf{p}^F = \mathbf{p}_E^F + p \operatorname{grad} n^F \tag{III.3.16b}$$

Each partial stress $\mathbf{T}^\alpha$ is a function of the constituent's effective stress $\mathbf{T}_E^\alpha$, which must be determined constitutively and the kinematic constraint p enforcing the saturation condition, which can be identified as the fluid hydraulic pressure. It is common (see for example discussion in Ehlers et al. (2008)) to consider the fluid as ideal and also to neglect the dissipative stress $\mathbf{T}_E^F$ (i.e. the fluid viscosity) in comparison to the drag generated by fluid-solid interactions $\mathbf{p}_E^F$, which is accounted for in Darcy's law, which is generally high for biological tissues because of their very small pores. Consequently, summing the partial stresses over constituents, the mixture stress $\mathbf{T}$ is defined in terms of the mixture effective stress $\mathbf{T}_E$:

$$\mathbf{T} = \mathbf{T}^S + \mathbf{T}^F = \mathbf{T}_E^{\mathrm{S}} - p \mathbf{I} \tag{III.3.17}$$

With the assumption of a purely (hyper)elastic solid, an incompressible inviscid fluid and an isothermal process, we have:

$$\psi^S = \psi^S(\mathbf{C}_S) \quad \text{and} \quad \psi^F = \psi^F(-) \tag{III.3.18}$$

where the right Cauchy-Green tensor is defined as:

$$\mathbf{C}_S = \mathbf{F}_S^{\mathrm{T}}\mathbf{F}_S \tag{III.3.19}$$

Eq. III.3.18 implies that:

$$\sum_\alpha \rho^\alpha \frac{D^\alpha \psi^\alpha}{Dt} = \rho^S \frac{\partial \psi^S}{\partial \mathbf{C}_S} : \frac{D^S \mathbf{C}_S}{Dt} \tag{III.3.20}$$

The time rate of change of the right Cauchy-Green tensor can be derived:

$$\frac{D^S \mathbf{C}_S}{Dt} = \frac{D^S \left(\mathbf{F}_S^{\mathrm{T}}\mathbf{F}_S\right)}{Dt} = 2\,\mathbf{F}_S^{\mathrm{T}}\mathbf{l}_S\mathbf{F}_S \tag{III.3.21}$$

Taking into account the above and the assumption $\mathbf{T}_E^F \approx 0$, Eq. III.3.15 can be written in the alternative form:

$$\left(\mathbf{T}_E^S - 2\rho^S \mathbf{F}_S \frac{\partial \psi^S}{\partial \mathbf{C}_S}\mathbf{F}_S^{\mathrm{T}}\right) : \mathbf{l}_S - \mathbf{p}_E^F \cdot \mathbf{w} \geq 0 \tag{III.3.22}$$

The above inequality must hold for any arbitrary motion and in particular in the absence of fluid motion relative to the solid, i.e. when $\mathbf{v}^S = \mathbf{v}^F$ and therefore $\mathbf{w} = \mathbf{0}$. In this case, the dissipative term $\mathbf{p}_E^F \cdot \mathbf{w}$ disappears and the inequality must hold for the purely elastic process. This can be achieved by enforcing the bracketed term in Eq. III.3.22 to zero, which allows, together with the definition of the strain energy defined per unit reference volume $W^S = \rho_0^S \psi^S$, to express the Cauchy stress as a function of the strain energy:

$$\mathbf{T}_E^S = 2\,\rho^S\,\mathbf{F}_S \frac{\partial \psi^S}{\partial \mathbf{C}_S}\mathbf{F}_S^{\mathrm{T}} = \,2\,J^{-1}\,\mathbf{F}_S \frac{\partial W^S}{\partial \mathbf{C}_S}\mathbf{F}_S^{\mathrm{T}} \tag{III.3.23}$$

Finally, a possible way to ensure dissipative energy (i.e. $-\mathbf{p}_E^F \cdot \mathbf{w} \geq 0$) is positive at all time, is to postulate that the momentum supply $\mathbf{p}_E^F$ is proportional to the seepage velocity $\mathbf{w}$. In Ehlers (2002), a relation stemming from Lai and Mow (1980) is proposed:

$$\mathbf{p}_E^F = -\frac{n^F}{k}\mathbf{w} \tag{III.3.24}$$

In the case of isotropic permeability, the hydraulic permeability k (which has units of $\mathrm{mm}^4\ \mathrm{N}^{-1}\ \mathrm{s}^{-1}$) is reduced to a scalar form and is defined as the ratio of the intrinsic permeability of the porous medium to the fluid's viscosity. Combining this relationship with Eq. III.3.16b, inserting the result in the balance of momentum of the fluid (Eq. III.3.1 for $\alpha = F$) and taking advantage of the neglected fluid dissipative stress ($\mathbf{T}_E^F \approx 0$) leads to:

$$\mathbf{w} = -k \operatorname{grad} p \tag{III.3.25}$$

It is interesting to notice that it was possible to retrieve the generalised Darcy's law for the mixture from thermodynamical considerations.

III.4 The osmotic contribution

The class of "swelling models" is based on the so-called Lanir hypothesis, which stems from the following statement Lanir (1987):

> "The magnitude of the concentration forces depends on the density of the negative group of the GAG - the fixed charge density. Hence, for any given specimen, these forces will depend on n^F (or n^S). The effect of time can be ignored here since the chemical potential responds to changes in local ionic environment with a time constant which is orders of magnitude shorter than the diffusional or mechanical time constants."

Lanir makes the assumption that, from a mechanical perspective, since anions and cations flow instantly to fulfil local electronic equilibrium across the continuum at all time, the ionic *diffusive* process can be neglected. As a result of this timescale separation, the swelling effects are assumed to solely depend on the imbalance in concentration of Na^+ ions between the inside and the outside of the tissue, and not the transient (at the electro-chemical timescale) ionic diffusive process (see Chapter II for details on the mechanisms of osmosis). Remembering that the concentration of sodium ions is directly related to the concentration of proteoglycans, and that these large molecules are trapped in the matrix of collagen fibre (Heneghan and Riches, 2008a), enables the osmotic effects to be evaluated, based on the fixed charge density, which is in turn related to the deformations of the mixture.

In terms of modelling, the Lanir hypothesis implies that the proteoglycan-driven swelling can be constitutively computed from volume changes in the mixture, thus

disregarding any ionic kinematics. This greatly reduces the complexity of the model by decreasing the number of governing equations, but equally importantly the number of material parameters. This hypothesis has been compared to triphasic models in 1D and 2D simulations in Wilson et al. (2005a), generally showing good agreement. Although results are not as good for rapid change in boundary concentrations, this is not considered an issue, as this situation does not manifest itself for soft tissues, (Karajan, 2009).

It is interesting to note that the osmotic effects have sometimes been modelled as a contribution to the solid (e.g. Ehlers et al. (2008)) and in other publications as a contribution to the overall pore pressure (e.g. Ehlers et al. (2009) or Schroeder et al. (2006)). In the first approach, the osmotic pressure is acting as a volumetric solid stress on the mixture (the proteoglycans only have little shear resistance). The resulting volume change of the mixture induces fluid flow, as can be seen in the balance of mass Eq. III.3.8. The latter approach considers the osmotic pressure as a contribution to the overall fluid pressure, driving fluid from and into the mixture through pressure gradients (i.e. Darcy's flux).

In the present work, we choose the first approach based on Ehlers et al. (2008). Following Lanir's hypothesis, the osmotic contribution is exclusively modelled as a solid contribution and swelling effects are induced by volume change of the mixture only. This implies that, in Darcy's law as defined in Eq. III.3.25, the pressure term is not enhanced with an osmotic term. This is reflected in Eq. III.4.1, where the solid effective stress is now split between a mechanical contribution $\boldsymbol{\sigma}^e$ (described by Eq. III.3.23) and an osmotic contribution $\Delta\pi$, which will subsequently be constitutively defined.

$$\begin{aligned} \mathbf{T}^{\mathrm{S}}_E &= \mathbf{T}^{\mathrm{S}}_{E,MECH} + \mathbf{T}^{\mathrm{S}}_{E,OSMO} \\ &= \boldsymbol{\sigma}^e - \Delta\pi\mathbf{I} \end{aligned} \tag{III.4.1}$$

III.5 Permeability

Fluid flow plays a paramount role in the behaviour of soft tissues (Mow and Mansour (1977); Lai and Mow (1980); Mow et al. (1980)). As seen in previous sections, the fluid's ability to flow through the porous solid is described by Darcy's law (Eq. III.3.25), and in particular controlled by the permeability of the tissue k. From a biological perspective, movement of fluid is responsible for the nutrition of the avascular disc. From a mechanical perspective, the low permeability of soft tissues (e.g.

magnitude of 10^{-3} mm^4 N^{-1} s^{-1}for the intervertebral disc permeability) has the function to protect the extra-cellular matrix under rapid loading by fluid pressurization. Moreover, as the tissue undergoes compressive strains, the geometry of the interstitial spaces evolves (compaction) and the intrinsic value of the permeability tends to decrease rapidly in order to further protect the solid skeleton (Olsen et al., 2004).

The relationship between permeability and tissue deformation is a crucial aspect of soft tissue modeling, as it is considered as one of the main source of nonlinearities (Holmes et al., 1985). The inhomogeneous compaction of the tissue, due to the frictional drag of the fluid on the solid, cannot be captured properly if the permeability is treated as a constant that represents the average of local permeabilities throughout the tissue. More recently, Hussain et al. (2011) proposed a comparative diurnal numerical analysis of a disc under compression in order to highlight the importance of the permeability strain dependency. It is argued that in some cases (e.g. change of disc height), strain dependency of the permeability plays a more significant role than the strain dependency of the osmotic pressure.

Models that exponentially relate the permeability to volumetric changes (e.g. Lai and Mow (1980); Holmes and Mow (1990); Argoubi and Shirazi-Adl (1996); Riches et al. (2002)) have shown better performance than linear models (Eisenfeld et al., 1978) in capturing the stiffening properties of the tissue (e.g. see Lai et al. (1981) for discussion on the behaviour under confined compression). Therefore, strain-dependent permeability will be considered in the current work, using exponential laws that will be defined in subsequent chapters. However, the anisotropy exhibited by the permeability (e.g. Gu et al. (1999); Ateshian and Weiss (2010)) will not be considered therein as it would appear inconsistent with the level of refinement of the current model.

III.6 A note on rate effects

There is no doubt that the intervertebral disc exhibits a rate-dependent behaviour. This results on the one hand from fluid flowing from and into the disc, and on the other hand because of the viscoelasticity of the collagen fibres. However, it is difficult to apportion the rate-dependent deformations between viscoelasticity and fluid flow.

Broberg (1993) argues that fibres' viscoelasticity plays an important part in the mechanical behaviour of the IVD under rapid loading (i.e. time constants of the order of two minutes), whereas fluid flow has a more significant role when the IVD is subjected to much slower loading (several hours). However, it is also admitted that

these observations were made under compression only and that it might not be valid under more complex loading, as fluid flow has been reported to be more dominant during flexure in Adams and Hutton (1983). It was also reported that 25% of diurnal creep deformations could be attributed to viscoelasticity within the annulus. This last point has been contested in Adams et al. (2006), where it is argued that the deformations "may simply be a structural effect arising from the annulus bulging more when the volume and the pressure of the disc is reduced", and therefore not arising from viscoelastic effects.

In Iatridis et al. (1997) and Iatridis et al. (1996), samples of nucleus pulposus were subjected to shearing in an attempt to demonstrate that the creep response of the solid arise from visco-elastic behaviour (i.e. without inducing volumetric changes to the tissue). While it is conceivable that, although 10% compressive strain were applied, the loading conditions are close to pure-shear, one can question whether a linear viscoelastic model is able to capture the local deformations arising during the dynamic loading under finite deformation and the impact of these deformations on on fluid flow.

In Holzapfel et al. (2005), small viscoelastic effects are observed in the annulus: tensile stiffnesses measured on single lamellae are found to reduce by less than 30% when the loading rate increases from 0.1 to 10 mm.s^{-1}.

Generally, it is very complicated to apportion the creep effects between fluid flow and viscosity. The consistent philosophy of the present model is to limit the number of model parameters to a strict minimum, and in particular to parameters that can be easily obtained experimentally. It therefore appears inappropriate to add complexity (i.e. constitutive relations and associated material parameters) in order to account for phenomena that are difficult to measure. Therefore, viscous effects are neglected and all time-dependent phenomena are considered to be resulting from fluid flow through the porous solid skeleton. This simplification implies that stiffnesses that should be attributed to viscous effects will be artificially "hidden" in the intrinsic permeability and shear modulus, which might be respectively under- and over-estimated. Given the high variability in the properties of biological tissues, one can argue that the impact will not be noticeable (see conclusions in Sec. V.6).

III.7 Conclusions

In this chapter, a theoretical framework for the modelling of the intervertebral disc was set out. The strategic decision to derive a biphasic swelling model based on

the theory of porous media was motivated from the disc's description provided in Chapter II, as well as a review of existing soft tissue models. Particular attention was given to the treatment of osmotic and rate-dependent effects, but also to define a consistent level of complexity for the model. The numerical procedure to solve the derived governing equations of the biphasic swelling model is provided in the following chapter.

Chapter IV

Finite Element Formulation

This chapter is concerned with the numerical treatment of the biphasic swelling model. The preliminary stage towards the construction of a finite element framework is the derivation of the variational problem, together with the clear definition of boundary conditions for each phase of the mixture. The resulting set of equations is linearised, to allow the nonlinear set of coupled equations to be solved with a Newton-Raphson procedure. Special care was taken in designing the termination criteria of the iterative scheme.

IV.1 Weak formulation

The governing equations of the biphasic swelling model were derived in Chapter III. The balances of momentum and mass, recalled in Eq. IV.1.1, represent the strong form of the problem.

$$\operatorname{div}\Big(\boldsymbol{\sigma}^e - (\Delta\pi + p)\,\mathbf{I}\Big) = \mathbf{0} \tag{IV.1.1a}$$

$$\operatorname{div}\Big(\mathbf{v}^S + \mathbf{w}\Big) = 0 \tag{IV.1.1b}$$

To be complete, the strong form requires a set of boundary conditions to be clearly established. Preliminarily to this step, it is necessary to select the primary variables. It could appear tempting to introduce a new variable that combines both the osmotic pressure and the hydraulic fluid pressure to obtain an overall pressure: $\mathfrak{p} = \Delta\pi + p$. However, as the osmotic pressure only exists within the mixture, the field $\mathfrak{p}$ could potentially be discontinuous at the pressure boundary (i.e. the essential boundary for

pressure as defined in the following), while it is required (even in the weak form) to be strongly fulfilled to avoid numerically unstable solutions (e.g. Ehlers and Acarturk (2009) and Ateshian et al. (2011)). Therefore, the set of primary variables is chosen as the couple $\{\mathbf{u}^S,\mathrm{p}\}$, where $\mathbf{u}^S$ is the vector of solid displacements and p the hydraulic fluid pressure.

The domain's boundary $\partial\Omega$, defined together with its outward normal $\mathbf{n}$, is split between essential and natural boundaries, which are independently defined for both variables. On the one hand, displacements $\bar{\mathbf{u}}^s$ are prescribed on the essential boundary $\Gamma_{\mathbf{u}^S}$ and tractions $\bar{\mathbf{t}}$ are prescribed on the natural boundary $\Gamma_{\mathbf{t}}$. On the other hand, pressures $\bar{p}$ are prescribed on the essential boundary Γ_p and the fluid flux $\bar{q}$ is defined on the natural boundary Γ_q. This is summarised in Eq. IV.1.2, where traction and flux are also defined.

$$\mathbf{u}^S = \bar{\mathbf{u}}^S \quad \text{on}\,\Gamma_{\mathbf{u}^S} \tag{IV.1.2a}$$

$$p = \bar{p} \quad \text{on}\,\Gamma_p \tag{IV.1.2b}$$

$$\Big(\boldsymbol{\sigma}^e - (p + \Delta\pi)\,\mathbf{I}\Big)\mathbf{n} = \bar{\mathbf{t}} \quad \text{on}\,\Gamma_{\mathbf{t}} \tag{IV.1.2c}$$

$$\mathbf{w}\cdot\mathbf{n} = \bar{q} \quad \text{on}\,\Gamma_q \tag{IV.1.2d}$$

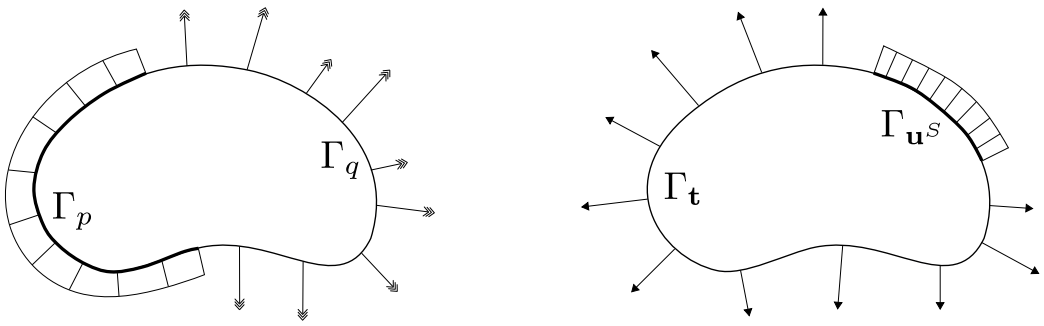

Figure IV.1: The domain's boundary $\partial\Omega$ is split between essential and natural boundary conditions relative to the fluid (left) and the solid (right)

Natural and essential boundary conditions cannot be simultaneously prescribed at a given point to the same degree of freedom, but either of them must always be prescribed. This is mathematically summarised as follows:

$$\begin{aligned} \partial\Omega &= \Gamma_{\mathbf{u}^S} \cup \Gamma_{\mathbf{t}} \quad \text{and} \quad \Gamma_{\mathbf{u}^S} \cap \Gamma_{\mathbf{t}} = \emptyset \\ \partial\Omega &= \Gamma_p \cup \Gamma_q \qquad \text{and} \quad \Gamma_p \cap \Gamma_q = \emptyset \end{aligned} \tag{IV.1.3}$$

However, essential and natural boundaries of the solid and the fluid are not required to coincide. This is illustrated on Fig. IV.1, showing that $\Gamma_{\mathbf{u}^S} \neq \Gamma_p$ and $\Gamma_{\mathbf{t}} \neq \Gamma_q$.

The boundary value problem is now fully defined by the governing equations Eq. IV.1.1 and the boundary conditions Eq. IV.1.2 and will be solved using a finite element formulation. In order to subsequently allow for discretisation, the weak form of the problem is derived using a standard Galerkin procedure. The governing equations Eq. IV.1.1a and Eq. IV.1.1b are respectively weighed by a vector of trial functions $\mathbf{f}$ and a scalar trial function g, and integrated over the domain Ω. Expressed in the current configuration, this results in the system:

$$\int_\Omega \mathbf{f} \cdot \operatorname{div}\Big(\boldsymbol{\sigma}^e - (\Delta\pi + p)\,\mathbf{I}\Big)\, dv = 0 \tag{IV.1.4a}$$

$$\int_\Omega g \operatorname{div}\Big(\mathbf{v}^S + \mathbf{w}\Big)\, dv = 0 \tag{IV.1.4b}$$

Using the identities:

$$\begin{aligned} \mathbf{f} \cdot \operatorname{div}(\boldsymbol{\sigma}^e) &= \operatorname{div}(\boldsymbol{\sigma}^e \mathbf{f}) - \boldsymbol{\sigma}^e : \operatorname{grad}\mathbf{f} \\ g \operatorname{div}(\mathbf{w}) &= \operatorname{div}(g\mathbf{w}) - \mathbf{w} \cdot \operatorname{grad} g \end{aligned} \tag{IV.1.5}$$

together with the Gauss-Theorem ($\int_a \mathbf{u}\cdot\mathbf{n}\, da = \int_v \operatorname{div}(\mathbf{u})\, dv$) allows the derivation of the weak form of the biphasic swelling model expressed in the current configuration:

$$\int_\Omega (\operatorname{grad}\mathbf{f}) : \Big(\boldsymbol{\sigma}^e - (\Delta\pi + p)\,\mathbf{I}\Big)\, dv - \int_{\Gamma_{\mathbf{t}}} \mathbf{f} \cdot \bar{\mathbf{t}}\, da = 0 \tag{IV.1.6a}$$

$$\int_\Omega \Big(g \operatorname{div}(\mathbf{v}) - k \operatorname{grad} p \cdot \operatorname{grad} g\Big)\, dv - \int_{\Gamma_q} g\, \bar{q}\, da = 0 \tag{IV.1.6b}$$

In solid mechanics, the weak form is often referred to as the principle of virtual work. This stems from the fact that the trial functions $\mathbf{f}$ and g are arbitrary functions, only required to vanish at the essential boundaries, which can be physically interpreted as

virtual displacements and pressure. This implies that Eq. IV.1.6 can be physically interpreted as residuals R_u and R_p, where trial displacements $\mathbf{u}^S$ and pressures p are sought to balance internal and external work. This can be rewritten as:

$$R_u(\mathbf{u}^S, p) = W_u^{int} - W_u^{ext} = 0 \tag{IV.1.7}$$

$$R_p(\mathbf{u}^S, p) = W_p^{int} - W_p^{ext} = 0 \tag{IV.1.8}$$

Note that, although the strong and weak forms are equivalent for sufficiently smooth trial functions (see for example Belytschko et al. (2000) for demonstration), continuity requirements on the trial functions $\mathbf{u}^S$ are lower in the weak form (i.e. C^0) than in the strong form (i.e. C^1).

IV.2 Linearisation

The previously derived weak form is a set of highly nonlinear equations. The source of nonlinearities are multiple:

- *Material nonlinearities.* The constitutive properties of the solid phase, the osmotic pressure and the permeability are all nonlinear functions of strains
- *Geometric nonlinearities.* In the finite deformation regime, the strains are nonlinear functions of displacements
- *Phase coupling.* Displacement and pressure fields are fully coupled

In the following, a Newton-Raphson scheme is formulated in order to solve the nonlinear problem. This consists in solving the problem in a sequence of linearised (i.e. approximated) problems. Linearisation, which allows the derivation of the tangent operator $\mathbf{K}$, relies on the first order (truncated) Taylor expansion of the residuals in the direction of the vector of incremental degrees of freedom $\delta\mathbf{q} = \left\{\delta\mathbf{u}^S, \delta p\right\}$ about the previously known state $\mathbf{q} = \left\{\mathbf{u}^S, p\right\}$. The directional derivative operator on the functional R, in the direction of $\delta\mathbf{q}$ and about $\mathbf{q}$, $DR(\mathbf{q})\left[\delta\mathbf{q}\right]$, is introduced (see for example de Souza Neto et al. (2008) and Bonet and Wood (2008) for more details on the directional derivative):

$$R(\mathbf{q} + \delta\mathbf{q}) \approx R(\mathbf{q}) + DR(\mathbf{q})\left[\delta\mathbf{q}\right] \tag{IV.2.1}$$

$$\approx R(\mathbf{q}) + \mathbf{K}\delta\mathbf{q} = \mathbf{0} \tag{IV.2.2}$$

Generally, $\mathbf{q}$ represents the solution obtained at the end of the previous increment and $\delta\mathbf{q}$ is the correction estimated at the current iteration as:

$$\delta\mathbf{q} = -\mathbf{K}^{-1}\mathbf{q} \tag{IV.2.3}$$

The Newton-Raphson algorithm, and in particular the criteria for stopping the iterative loop, will be investigated in greater details in the following section, as the linearisation process (i.e. the determination of the tangent operator $\mathbf{K}$) is herein considered.

In Sec. III.3, it was discussed that all quantities can be either expressed in the current configuration (i.e. the Eulerian description, expressed in terms of the current coordinates $\mathbf{x}$) or in the reference configuration (i.e. the Lagrangian description, expressed in terms of the reference coordinates $\mathbf{X}$). This equally applies to the governing equation, which have so far been expressed in the current configuration, but also to the linearisation process. Although the outcome is equivalent, the linearisation can be performed either using the Lagrangian description or the Eulerian description.

In the following, although the Eulerian description is sought, the linearisation will be performed on the Lagrangian description as it induces simpler derivations. This is mainly due to the fact that in the Lagrangian description, the domain's boundary is fixed (i.e. dV is constant), which is not the case for the Eulerian description. This is done in a three-step process:

1. pull-back: all quantities in Eq. IV.1.6 expressed in the current configuration are transformed to their Lagrangian counterpart in order to obtain the Lagrangian description of the weak form

2. linearisation: the directional derivative of the weak form is performed in the reference configuration

3. push-forward: all quantities in the resulting system of equations are transformed to their Eulerian counterpart in order to obtain Eulerian formulation

The first step requires to transform all used quantities from the current configuration to the reference configuration. The volume is simply transformed using the jacobian defined in Sec. III.3 and recalled in Eq. IV.2.4a. With Nanson's formula (Eq. IV.2.4b), the infinitesimal surface element da and its normal $\mathbf{n}$ are mapped back to the material frame. Finally, the Cauchy stress is pulled back in Eq. IV.2.4c, which

allows the introduction of the second Piola-Kirchhoff stress tensor $\mathbf{S}^e$, which is a symmetrical Lagrangian measure of stress:

$$dv = J dV \tag{IV.2.4a}$$
$$\mathbf{n}\, da = J\mathbf{F}_S^{-\mathrm{T}}\mathbf{N} dA \tag{IV.2.4b}$$
$$\boldsymbol{\sigma}^e = J^{-1}\mathbf{F}_S\mathbf{S}^e\mathbf{F}_S^{\mathrm{T}} \tag{IV.2.4c}$$

Notations introduced in Sec. III.2 are used to describe the divergence and gradients operators in the reference configuration:

$$\begin{aligned} \mathbf{grad}(\bullet) &= \mathbf{Grad}(\bullet)\mathbf{F}_S^{-1} \\ \mathrm{div}(\bullet) &= \mathrm{Div}(\bullet)\cdot\mathbf{F}_S^{-1} \end{aligned} \tag{IV.2.5}$$

Inserting the identities Eq. IV.2.4 and Eq. IV.2.6a enables us to perform the pull-back operation on (Eq. IV.1.6) and obtain the Lagrangian description of the weak form:

$$\int_\Omega (\mathrm{Grad}\,\mathbf{f}\,) : \left(\mathbf{S}^e\mathbf{F}_S^{\mathrm{T}} - (\Delta\pi + p)\, J\mathbf{F}_S^{-1}\right) dV_0 = \int_{\Gamma_\mathbf{t}} \mathbf{f}\bar{\mathbf{t}}_0\, dA_0 \tag{IV.2.6a}$$
$$\int_\Omega J\left(g\,\mathrm{Div}\,(\mathbf{v})\,\mathbf{F}_S^{-1} + k\,\mathrm{Grad}\,p\,\mathbf{F}_S^{-1}\mathrm{Grad}\,g\,\mathbf{F}_S^{-1}\right) dV_0 = \int_{\Gamma_q} g\,\bar{q}_0\, dA_0 \tag{IV.2.6b}$$

where:

$$\begin{cases} \bar{\mathbf{t}}_0 = \left(\mathbf{F}_S\mathbf{S}^e - J\,(p + \Delta\pi)\,\mathbf{F}_S^{-\mathrm{T}}\right)\mathbf{N} \\ \bar{q}_0 = Jk\,\mathrm{Grad}\,p\,\mathbf{F}_S^{-1}\mathbf{F}_S^{-\mathrm{T}}\mathbf{N} = J\mathbf{w}_0\mathbf{F}_S^{-1}\mathbf{F}_S^{-\mathrm{T}}\mathbf{N} \end{cases} \tag{IV.2.7}$$

The second step is the linearisation process. It consists in assuming that the solution of the displacement and pressure fields at time step $t + \Delta t$ can be expressed as an estimate at time t plus a perturbation term (Eq. IV.2.8):

$$\begin{cases} \mathbf{u}^S(t + \Delta t) = \mathbf{u}^S(t) + \delta\mathbf{u}^S = \hat{\mathbf{u}}^\mathbf{S} + \delta\mathbf{u}^S \\ p(t + \Delta t) = p(t) + \delta p = \hat{p} + \delta p \end{cases} \tag{IV.2.8}$$

More generally, Eq. IV.2.8 allows to linearise each quantity $(\bullet)$, which can be expressed using the same notations, i.e. $(\bullet) = \hat{(\bullet)} + \delta\,(\bullet)$. (e.g. de Borst et al. (2006)):

$$\begin{cases} \mathbf{F}_S = \hat{\mathbf{F}}_S + \delta\mathbf{F}_S & J = \hat{J} + \delta J \\ \mathbf{S}^e = \hat{\mathbf{S}}^e + \delta\mathbf{S}^e & \mathbf{v} = \hat{\mathbf{v}} + \delta\mathbf{v} \\ k = \hat{k} + \delta k & \Delta\pi = \hat{\Delta\pi} + \delta\left(\Delta\pi\right) \end{cases} \tag{IV.2.9}$$

In order to account for the material nonlinearities, it is necessary to introduce the Green-Lagrange strain tensor:

$$\mathbf{E} = \frac{1}{2}\left(\mathbf{F}_S^{\mathrm{T}}\mathbf{F}_S - \mathbf{I}\right) \tag{IV.2.10}$$

The Green-Lagrange tensor, a Lagrangian strain measure, is the work conjugate of the second Piola-Kirchhoff $\mathbf{S}^e$, which allows to define the Lagrangian elasticity tensor $\mathcal{C} = \frac{\partial \mathbf{S}^e}{\partial \mathbf{E}}$ that relates incremental stress changes of the solid phase to incremental displacement. This leads to the perturbation terms:

$$\begin{cases} \delta\mathbf{F}_S = \mathrm{Grad}\,\delta\mathbf{u}^S & \delta J = \det\left(\hat{\mathbf{F}}_S\right)\hat{\mathbf{F}}_S^{-1} : \delta\mathbf{F}_S \\ \delta\mathbf{v} = \delta\dot{\mathbf{u}} & \delta\mathbf{S}^e = \frac{\partial \mathbf{S}^e}{\partial \mathbf{E}} : \left(\hat{\mathbf{F}}_S^{\mathrm{T}}\,\delta\mathbf{F}_S\right) = \mathcal{C} : \left(\hat{\mathbf{F}}_S^{\mathrm{T}}\,\delta\mathbf{F}_S\right) \end{cases} \tag{IV.2.11}$$

It is common to estimate the linearised inverse of the deformation gradient (see for example derivation in Henderson and Searle (1981)) by taking only the first order terms into account:

$$\begin{cases} \mathbf{F}_S^{-1} \approx \hat{\mathbf{F}}_S^{-1} + \delta\mathbf{F}_S^{-1} \\ \delta\mathbf{F}_S^{-1} = -\hat{\mathbf{F}}_S^{-1}\delta\mathbf{F}_S\hat{\mathbf{F}}_S^{-1} \end{cases} \tag{IV.2.12}$$

The linearised problem is finally obtained by inserting the linearised quantities from Eq. IV.2.9 to IV.2.12 into the weak form (Eq. IV.2.6):

$$\int_\Omega \left(\mathrm{Grad}\,\mathbf{f}\right) : \Big[\left(\hat{\mathbf{S}}^e + \delta\mathbf{S}^e\right)\left(\hat{\mathbf{F}}_S + \delta\mathbf{F}_S\right)^T - \left(\hat{p} + \delta p + \hat{\Delta\pi} + \delta\left(\Delta\pi\right)\right) \left(\hat{J} + \delta J\right)\left(\hat{\mathbf{F}}_S^{-1} + \delta\mathbf{F}_S^{-1}\right)\Big]\, dV_0 = \int_{\Gamma_\mathbf{t}} \mathbf{f}\bar{\mathbf{t}}_0\, dA_0 \tag{IV.2.13a}$$

$$\int_\Omega \left(\hat{J} + \delta J\right)\Big[\left(g\,\mathrm{Div}\left(\hat{\mathbf{v}} + \delta\mathbf{v}\right)\left(\hat{\mathbf{F}}_S^{-1} + \delta\mathbf{F}_S^{-1}\right) + \left(\hat{k} + \delta k\right)\mathbf{Grad}\left(\hat{p} + \delta p\right) \left(\hat{\mathbf{F}}_S^{-1} + \delta\mathbf{F}_S^{-1}\right)\mathrm{Grad}\, g\,\left(\hat{\mathbf{F}}_S^{-1} + \delta\mathbf{F}_S^{-1}\right)\Big]\, dV_0 = \int_{\Gamma_q} g\,\bar{q}_0\, dA_0 \tag{IV.2.13b}$$

The linearisation is performed to the first order, therefore neglecting multiplicative inter-perturbation terms. In addition, following Vankan et al. (1997), the perturbations δJ and $\delta\mathbf{F}_S^{-1}$, corresponding to variations of internal energy due to volume and

geometry changes are neglected. Moving the internal and external force terms to the right hand-side leads to the linearised weak form in the reference configuration:

$$\int_\Omega (\mathrm{Grad}\,\mathbf{f}) : \left[\hat{\mathbf{S}}^e \delta\mathbf{F}_S^{\mathrm{T}} + \left(\frac{\partial \mathbf{S}^e}{\partial \mathbf{E}} : \left(\hat{\mathbf{F}}_S^{\mathrm{T}}\,\delta\mathbf{F}_S\right)\right)\hat{\mathbf{F}}_S^{\mathrm{T}} - \hat{J}\,(\delta p + \delta\,(\Delta\pi))\,\hat{\mathbf{F}}_S^{-1}\right] dV_0 = \int_{\Gamma_{\mathbf{t}}} \mathbf{f}\bar{\mathbf{t}}_0\, dA_0 - \int_\Omega (\mathrm{Grad}\,\mathbf{f}) : \left[\hat{\mathbf{S}}\hat{\mathbf{F}}_S^{\mathrm{T}} - \hat{J}\left(\hat{p} + \hat{\Delta\pi}\right)\hat{\mathbf{F}}_S^{-1}\right] dV_0 \tag{IV.2.14a}$$

$$\int_\Omega \hat{J}\left[\left(g\,\mathrm{Div}\,(\delta\mathbf{v})\,\hat{\mathbf{F}}_S^{-1} + \left(\hat{k}\,\mathrm{Grad}\,\delta p + \delta k\,\mathrm{Grad}\,\hat{p}\right)\hat{\mathbf{F}}_S^{-1}\mathrm{Grad}\,g\,\hat{\mathbf{F}}_S^{-1}\right] dV_0 = \int_{\Gamma_q} g\,\bar{q}_0\, dA_0 - \int_\Omega \hat{J}\left(g\,\mathrm{Div}\,(\hat{\mathbf{v}})\,\hat{\mathbf{F}}_S^{-1} + \hat{k}\,\mathrm{Grad}\,\hat{p}\,\hat{\mathbf{F}}_S^{-1}\mathrm{Grad}\,g\,\hat{\mathbf{F}}_S^{-1}\right) dV_0 \tag{IV.2.14b}$$

In a third step, the Eulerian formulation is recovered by a push-forward operation on Eq. IV.2.14, and using the inverse of identities Eq. IV.2.4 and Eq. IV.2.6a. For more details about the term regarding the material nonlinearity of the solid phase in Eq. IV.2.15a, the reader is referred to the derivation in Bonet and Wood (2008).

$$\int_\Omega \frac{1}{2}\left(\mathrm{grad}\,\mathbf{f} + \mathrm{grad}\,\mathbf{f}^{\mathrm{T}}\right) : \boldsymbol{c} : \left(\mathbf{grad}\,\delta\mathbf{u} + (\mathbf{grad}\,\delta\mathbf{u})^{\mathrm{T}}\right) + (\mathrm{grad}\,\mathbf{f}) : \left(\hat{\boldsymbol{\sigma}}^{\mathbf{e}}\,(\mathrm{grad}\,\delta\mathbf{u})^{\mathrm{T}}\right) - (\mathrm{grad}\,\mathbf{f}) : \left((\delta p + \delta\,(\Delta\pi))\,\mathbf{I}\right) dv = \int_{\Gamma_{\mathbf{t}}} \mathbf{f}\bar{\mathbf{t}}\, da - \int_\Omega (\mathrm{grad}\,\mathbf{f}) : \left(\boldsymbol{\sigma}^e - \left(\hat{p} + \hat{\Delta\pi}\right)\right) dv \tag{IV.2.15a}$$

$$\int_\Omega \left[g\,\mathrm{div}\,(\delta\mathbf{v}) + \left(\hat{k}\,\mathrm{grad}\,\delta p + \delta k\,\mathrm{grad}\,\hat{p}\right)\mathrm{grad}\,g\right] dv = \int_{\Gamma_q} g\,\bar{q}\, da - \int_\Omega \left(g\,\mathrm{div}\,(\hat{\mathbf{v}}) + \hat{k}\,\mathrm{grad}\,\hat{p}\,\mathrm{grad}\,g\right) dv \tag{IV.2.15b}$$

The right hand sides of the above equations are measuring imbalances between external forces applied on the essential (i.e. traction and flux) boundary conditions:

$$\begin{cases} \int_{\Gamma_{\mathbf{t}}} \mathbf{f}\bar{\mathbf{t}}\, da \\ \int_{\Gamma_q} g\,\bar{q}\, da \end{cases} \tag{IV.2.16}$$

and the internal forces:

$$\begin{cases} \int_\Omega g\,\mathrm{div}\,(\hat{\mathbf{v}}) + \mathrm{grad}\,\hat{\mathbf{w}}\,\mathrm{grad}\,g\, dv \\ \int_\Omega (\mathrm{grad}\,\mathbf{f}) : \left(\boldsymbol{\sigma}^e - \left(\hat{p} + \hat{\Delta\pi}\right)\mathbf{I}\right) dv \end{cases} \tag{IV.2.17}$$

that are arising from the loading of the mixture (external load, flux or osmosis) and the transient deformations related to fluid flow or volume changes. The left hand-side defines the tangent operator that will operate on the residual to estimate the perturbations $\delta\mathbf{q} = \left\{\delta\mathbf{u}^S, \delta p\right\}$, which will restore the balance between internal and external forces. In Eq.IV.2.15a, the first two terms are respectively measuring the geometric and material nonlinearities, while the third one evaluates the nonlinear coupling between both phases and the last one accounts for the osmotic contribution. In Eq. IV.2.15b, the first term is the counter part of the coupling term in Eq.IV.2.15a while the last two account for the nonlinearities in the fluid flow.

IV.3 Discretisation

In this section, the linearised equilibrium equations previously derived are discretised. This involves the introduction of a numerical time integration scheme, splitting the time-continuum into time increments and the introduction of a finite element discretisation of the domain, where spatial interpolation functions are defined on subdivisions of the domain's continuum.

IV.3.1 Time discretisation

An integration scheme needs to be defined in order to express the solid velocity $\mathbf{v}^S$ as a function of the solid displacements $\mathbf{u}^S$. The unconditionally stable backward finite difference scheme is chosen (see for example Hughes (1987)). It is implicit in the sense that the derivative of the primary variable $\mathbf{u}^S$ at time $t + dt$ is expressed as a function of its derivative at $t + dt$ rather than t:

$$\mathbf{v}^S_{t+\Delta t} = \dot{\mathbf{u}}^S_{t+\Delta t} = \frac{\mathbf{u}^S_{t+\Delta t} - \mathbf{u}^S_t}{\Delta t} \tag{IV.3.1}$$

where Δt is the time increment. As a consequence,:

$$\delta\mathbf{v}^S = \frac{\delta\mathbf{u}^S}{\Delta t} \tag{IV.3.2}$$

IV.3.2 Spatial discretisation

Finally, the standard Galerkin formulation is obtained by discretising the linearised weak form in space. In order to fulfil the inf-sup condition (see Brezzi and Fortin

(1991) and Chapelle and Bathe (1993)), Taylor-Hood elements are employed (named after Taylor and Hood (1973)). Quadratic shape functions are used to approximate the solid displacements and linear shape functions for the pressure. The weighting functions are discretised using the same shape functions as those used for displacement and pressure. In Eq. IV.3.3, the discretised quantities are expressed in matrix form using the vectors of shape functions $\mathbf{N}^u$ and $\mathbf{N}^p$, for displacements and pressure respectively. $(\bullet)^e$ denotes the vector of nodal unknowns for the field $(\bullet)$.

$$\begin{cases} \mathbf{u}^S = \mathbf{N}^u \mathbf{u}^e \\ \mathbf{v}^S = \mathbf{N}^u \mathbf{v}^e \\ p = \mathbf{N}^p \mathbf{p}^e \end{cases} \qquad \begin{cases} \mathbf{f} = \mathbf{N}^u \mathbf{f^e} \\ g = \mathbf{N}^p \mathbf{g}^e \end{cases} \tag{IV.3.3}$$

Inserting the discretisation (Eq. IV.3.3) into linearised weak form (Eq. IV.2.15) allows to express the linearized weak form in vector format.

$$\begin{bmatrix} 0 & 0 \\ \mathbf{K}_{p\dot{u}} & 0 \end{bmatrix} \begin{Bmatrix} \delta\dot{\mathbf{u}} \\ \delta\dot{\mathbf{p}} \end{Bmatrix} + \begin{bmatrix} \mathbf{K}_{uu} & \mathbf{K}_{up} \\ 0 & \mathbf{K}_{pp} \end{bmatrix} \begin{Bmatrix} \delta\mathbf{u} \\ \delta\mathbf{p} \end{Bmatrix} = \begin{Bmatrix} \mathbf{F}_u^{ext} \\ \mathbf{F}_p^{ext} \end{Bmatrix} - \begin{Bmatrix} \mathbf{F}_u^{int} \\ \mathbf{F}_p^{int} \end{Bmatrix} \tag{IV.3.4}$$

Substituting Eq. IV.3.2 into the above yields:

$$\mathbf{K}_{p\dot{u}} \delta\mathbf{u} + \Delta t \, \mathbf{K}_{pp} \delta\mathbf{p} = \Delta t \left(\mathbf{F}_p^{ext} - \mathbf{F}_p^{int} \right) \tag{IV.3.5}$$

Eq. IV.3.4 is then rewritten in the more convenient form, introducing $\mathbf{K}_{pu} = \mathbf{K}_{p\dot{u}}$:

$$\begin{bmatrix} \mathbf{K}_{uu} & \mathbf{K}_{up} \\ \mathbf{K}_{pu} & \Delta t \, \mathbf{K}_{pp} \end{bmatrix} \begin{Bmatrix} \delta\mathbf{u} \\ \delta\mathbf{p} \end{Bmatrix} = \begin{Bmatrix} \mathbf{F}_u^{ext} \\ \Delta t \, \mathbf{F}_p^{ext} \end{Bmatrix} - \begin{Bmatrix} \mathbf{F}_u^{int} \\ \Delta t \, \mathbf{F}_p^{int} \end{Bmatrix} \tag{IV.3.6}$$

Although the constitutive models for the strain-dependent permeability and the osmotic pressure will be selected in subsequent sections, the following notations are introduced without any loss of generality, using the fact that $k = k(\mathbf{u})$ and $\Delta\pi = \Delta\pi(\mathbf{u})$:

$$\begin{aligned} \delta k &= \tilde{k} \delta\mathbf{u} \\ \delta(\Delta\pi) &= \tilde{\Delta\pi} \delta\mathbf{u} \end{aligned} \tag{IV.3.7}$$

This allows to collect their linearised terms into the appropriate block of Eq. IV.3.6

to explicitly specify the elemental stiffness tensor and force vectors. Note the introduction of the notation $\nabla(\bullet) = \text{grad}(\bullet)$ for clarity:

$$\mathbf{K}_{uu} = \int_v \{\nabla \mathbf{N}^u\}^{\mathrm{T}} \mathbf{D} \nabla \mathbf{N}^u + \{\nabla \mathbf{N}^u\}^{\mathrm{T}} \boldsymbol{\sigma}^e \nabla \mathbf{N}^u + \{\nabla \mathbf{N}^u\}^{\mathrm{T}} \tilde{\Delta\pi}\, dv \tag{IV.3.8a}$$

$$\mathbf{K}_{up} = \int_v \nabla \mathbf{N}^u \{\mathbf{N}^p\}^{\mathrm{T}}\, dv \tag{IV.3.8b}$$

$$\mathbf{K}_{pu} = \int_v \mathbf{N}^p \{\nabla \mathbf{N}^u\}^{\mathrm{T}} + \nabla \mathbf{N}^p \hat{\mathbf{p}}^e \tilde{k} \nabla \mathbf{N}^p\, dv \tag{IV.3.8c}$$

$$\mathbf{K}_{pp} = \int_v \{\nabla \mathbf{N}^p\}^{\mathrm{T}} k \nabla \mathbf{N}^p\, dv \tag{IV.3.8d}$$

$$\mathbf{F}_u^{int} = \int_v \{\nabla \mathbf{N}^u\}^{\mathrm{T}} \hat{\boldsymbol{\sigma}}^e - \{\nabla \mathbf{N}^u\}^{\mathrm{T}} \left(\mathbf{N}^p \hat{\mathbf{p}}^e + \mathbf{N}^u \hat{\Delta\pi}^e\right) dv \tag{IV.3.8e}$$

$$\mathbf{F}_p^{int} = \int_v \{\nabla \mathbf{N}^p\}^{\mathrm{T}} k \nabla \mathbf{N}^p \hat{\mathbf{p}}^e + \mathbf{N}^p \nabla \mathbf{N}^u \hat{\mathbf{v}}^e\, dv \tag{IV.3.8f}$$

$$\mathbf{F}_u^{ext} = \int_a \{\mathbf{N}^u\}^{\mathrm{T}} \bar{\mathbf{t}}\, da \tag{IV.3.8g}$$

$$\mathbf{F}_p^{ext} = \int_a \{\mathbf{N}^p\}^{\mathrm{T}} \bar{q}\, da \tag{IV.3.8h}$$

where $\mathbf{D}$ is the matrix representation of the fourth-order elasticity tensor.

$\mathbf{K}_{uu}$ is the sum of the geometric, material and osmotic contributions respectively. The tangent matrix is not symmetrical due to the strain dependent permeability. When the permeability k is constant, $\mathbf{K}_{up} = \mathbf{K}_{pu}^{\mathrm{T}}$ and the tangent matrix is symmetrical.

Eq. IV.3.6-IV.3.8 can be directly used for an Eulerian formulation. These relationships can easily be pulled back to the reference configuration for a Lagrangian formulation using the relationships Eq. IV.2.4.

IV.4 Termination criterion for the Newton-Raphson algorithm

All requirements for the implementation of the Newton-Raphson procedure have now been derived. However, the algorithm, which is summarised in Fig. IV.2, requires the definition of a termination criterion for the iterative Newton loop. The objective is to define a criterion that ensures the procedure only stops once an acceptable balance between the external and internal forces is found. For example, a criterion minimising the energy flow to the system from the residual, was initially envisaged:

$$e \leq \varepsilon \max\left(W^{ext}, W^{int}\right) \tag{IV.4.1}$$

e, W^{ext} and W^{ext} are defined as follows, where $\sum_{dof}$ indicates the sum over the degrees of freedom of the relevant vector:

$$e = \sqrt{\sum_{dof} \delta q_j^2 \cdot R_j^2} \tag{IV.4.2}$$

$$W^{ext} = \sqrt{\sum_{dof} (\Delta q_j)^2 \cdot (F^{ext})^2} \tag{IV.4.3}$$

$$W^{int} = \sqrt{\sum_{dof} (\Delta q_j)^2 \cdot (F^{int})^2} \tag{IV.4.4}$$

This ensures that the iterative process will only stop when the incremental work done during the i-th increment is large enough (i.e. constrained by ε) compared to the iterative work done by the out of balance force during the j-th iteration.

This criterion usually performs well in the particular case of single phase problems. However, the biphasic problem is defined by a set of two equations, each of which describes a very specific physical process. The magnitude of residuals and associated degrees of freedom emerging from these equations can span several orders depending on the material parameters and the type of loading. This is, for example, the case for a highly permeable mixture experiencing slow loading: residuals associated with the continuity equation may be considerably smaller than those associated to the momentum balance, even during the first increment. It may in turn result in condition IV.4.1 being met even if the residuals associated with the solid phase are still large. In addition, the rate of convergence of the system can be different for the two equations.

It is therefore crucial to treat the residuals $\mathbf{R}_j^{\mathbf{u}}$ and $\mathbf{R}_j^p$, respectively derived from of the balance of momentum and the balance of mass, separately. This leads to the following system:

$$\begin{cases} e_{\mathbf{u}} \leq \varepsilon \max\left(W_{\mathbf{u}}^{ext}, W_{\mathbf{u}}^{int}\right) \\ e_p \leq \varepsilon \max\left(W_p^{ext}, W_p^{int}\right) \end{cases} \tag{IV.4.5}$$

where:

$$e_{\mathbf{u}} = \sqrt{\sum_{dof} (\delta q_j^{\mathbf{u}})^2 \cdot (R_j^{\mathbf{u}})^2} \qquad e_p = \sqrt{\sum_{dof} (\delta q_j^p)^2 \cdot (R_j^p)^2} \tag{IV.4.6}$$

$$W_{\mathbf{u}}^{ext} = \sqrt{\sum_{dof} (\Delta q_j^{\mathbf{u}})^2 \cdot (F_{\mathbf{u}}^{ext})^2} \qquad W_p^{ext} = \sqrt{\sum_{dof} (\Delta q_j^p)^2 \cdot (F_p^{ext})^2} \tag{IV.4.7}$$

$$W_{\mathbf{u}}^{int} = \sqrt{\sum_{dof} (\Delta q_j^{\mathbf{u}})^2 \cdot (F_{\mathbf{u}}^{int})^2} \qquad W_p^{int} = \sqrt{\sum_{dof} (\Delta q_j^p)^2 \cdot (F_p^{int})^2} \tag{IV.4.8}$$

This scheme proves to work well under most circumstances, with the exception of ramp-hold types of loading. In this case, energy flows $e_{\mathbf{u}}$ and e_p as well as the incremental work done ($W_{\mathbf{u}}^{ext}$ and W_p^{ext}) may be small during the relaxation phase, leading to termination criteria that may never be met. This issue is circumvented by defining the termination criteria as a set decrease of the energy flow, either in a relative or absolute capacity:

$$\max(e_{\mathbf{u}}, e_p) \leq \varepsilon_r \max(e_{\mathbf{u}}^0, e_p^0) \tag{IV.4.9}$$

$$\max(e_{\mathbf{u}}, e_p) \leq \varepsilon_a \tag{IV.4.10}$$

The drawback of this criteria is that the choice of ε_r and ε_a is problem specific and requires special care.

For *Increment* i **do**

Initialise

- The vector of degrees of freedom: $\mathbf{q}_i = \mathbf{q}_{i-1} + \bar{\mathbf{q}}_i$;
- The incremental vector of degrees of freedom: $\Delta\mathbf{q}_i = \mathbf{0}$;
- The incremental force vector: $\mathbf{F}^{ext} = \mathbf{F}^{ext}(i)$;
- The iterative counter j=0;

Evaluate

- The internal force vector using Eq. IV.3.8e-f: $\mathbf{F}^{int} = \mathbf{F}^{int}(\mathbf{q}_i)$;
- The residual: $\mathbf{R}_0 = \mathbf{F}^{ext} - \mathbf{F}^{int}$;
- The problem specific norm of the residual: $||\mathbf{R}|| = F(\mathbf{R}_0)$;

Do *Iterative Newton loop* j **while** $||R|| < \varepsilon$

Evaluate

- The global stiffness matrix using Eq. IV.3.8a-d: $\mathbf{K} = \mathbf{K}(\mathbf{q}_i)$;
- The iterative correction: $\delta\mathbf{q}_j$ = -$\mathbf{KR}$;

Update

- The incremental vector of degrees of freedom: $\Delta\mathbf{q}_i = \sum_{k=1}^{j} \delta\mathbf{q}_k$;
- The vector of degrees of freedom: $\mathbf{q}_i = \mathbf{q}_{i-1} + \bar{\mathbf{q}}_i + \Delta\mathbf{q}_i$;
- The internal force vector: $\mathbf{F}^{int} = \mathbf{F}^{int}(\mathbf{q}_i)$;
- The residual: $\mathbf{R}_j = \mathbf{F}^{ext} - \mathbf{F}^{int}$;
- The norm of the residual: $||\mathbf{R}|| = F(\mathbf{R}_j)$;
- $j = j + 1$;

end

end

Figure IV.2: The Newton-Raphson algorithm for a single increment i

IV.5 Conclusion

In this chapter, the numerical procedure to solve the previously derived set of governing equations was developed. This involved the definition of boundary conditions for both the solid and the fluid, the transformation of the strong form to the weak form, which was ultimately linearised in order to derive the tangent operator, and discretised in both time and space. This procedure enabled us to use a Newton-Raphson iterative scheme to solve the nonlinear problem. Additionally, a specific termination criterion was defined for the iterative solver. In the following sections, this scheme will be first tested for the one dimensional isotropic problem, before embarking on the three dimensional fibre reinforced problem.

Chapter V

The 1D model: confined compression test

The biphasic swelling model is initially reduced to the one-dimensional case in order to investigate the behaviour of the nucleus pulposus subjected to confined compression. The derived equations are coded in Matlab, together with carefully chosen constitutive relationships in order to test the model's performance against experimental data. Finally, results of the 1D model are used to study and gain understanding of the coupled mechanisms within the disc, to provide a foundation for the work that follows in Chapter VI.

V.1 Confined compression: the reduced model

This chapter aims on the one hand to evaluate the appropriateness of the biphasic swelling model when applied to a relatively simple problem and on the other hand to facilitate familiarity with the mechanics of porous and charged tissues. Reducing the preceding derivation to one dimension enables the modelling of an idealisation of the confined compression test. In the whole of this chapter, our interest will focus on the experiment described in Fig. V.1: a cylindrical sample of nucleus pulposus (the isotropic part of the IVD) is placed in a confining chamber and subjected to axial displacements. The impermeable and rigid lateral membrane prohibits any lateral expansion and fluid flow, while the above and below porous platens enforce uni-axial displacements and fluid flow. To some extent, this can be viewed as a crude approximation of an intervertebral disc subjected to compression, with an infinitely stiff annulus pulposus.

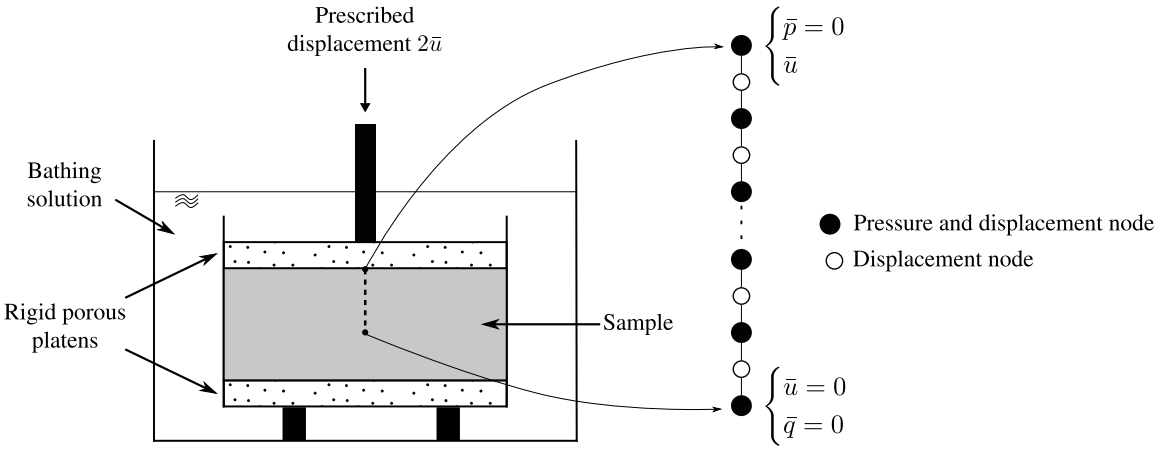

Figure V.1: Confined compression apparatus with associated mesh taking advantage of the symmetry

In order to take advantage of the symmetry of this problem and therefore only model the upper half of the sample, fluid flow and displacements at the centre of the sample are constrained and only half of the prescribed displacements are applied to the top node. Following Sec. IV.3.2, 2-node linear elements are used for the pressure field and 3-node quadratic elements for the displacement field (see Fig. V.1). The shape functions expressed in the local iso-parametric coordinate system $\xi \in [-1; 1]$ are:

$$\begin{cases} N_1^u(\xi) = & -\frac{\xi}{2}(1-\xi) \\ N_2^u(\xi) = & (1-\xi)(1+\xi) \\ N_3^u(\xi) = & \frac{\xi}{2}(1+\xi) \end{cases} \qquad \begin{cases} N_1^p(\xi) = \frac{1}{2}(1-\xi) \\ N_2^p(\xi) = \frac{1}{2}(1+\xi) \end{cases} \tag{V.1.1}$$

In 1D, the mathematical problem simplifies drastically due to the fact that all vectorial and tensorial quantities reduce to scalars. This is for example the case for the position vector:

$$\mathbf{X} = \mathbf{X}(X_1, X_2, X_3) \xrightarrow{1D} X_1 = X \tag{V.1.2}$$

For clarity, three dimensional quantities that are usually referred to with bold characters will be reduced to scalar in 1D by discarding the boldface (e.g. $\boldsymbol{\sigma}^e \xrightarrow{1D} \sigma^e$). Conveniently in 1D, the gradient of deformation reduces to the stretch, which is a strain measure that evaluates the elongation at a given material point:

$$\mathbf{F} \xrightarrow{1D} F(X,t) = \frac{\partial x(X,t)}{\partial X} = 1 + \frac{\partial u(X,t)}{\partial X} = \lambda(X,t) \tag{V.1.3}$$

As Eq. V.1.3 shows, the stretch is a Lagrangian strain measure (i.e. expressed in

terms of the Lagrangian position X). This makes is particularly practical to derive the 1D model using a total-Lagrangian formulation as all quantities are naturally expressed in terms of the stretch.

In the special case of confined compression, the axial stretch $\lambda = \lambda_1$ directly measures the level of compression, while lateral stretches remain constant since the section of the sample cannot expand (i.e. $\lambda_2 = \lambda_3 = 1$). This yields the following simplifications:

$$\begin{cases} J = \lambda_1 \lambda_3 \lambda_3 = \lambda \\ dv = JdV = \lambda A dX \\ da = dA \\ S^e = \frac{1}{\lambda} \sigma^e \end{cases} \tag{V.1.4}$$

V.2 Constitutive relations

Up to this point, the modelling framework remained very general and could be equally used to model a number of problems such as brain tissues or articular cartilage. In this section, constitutive models for each phase and the osmotic pressure are selected for the particular case of nucleus pulposus tissues.

V.2.1 Strain dependent permeability

The well established exponential model proposed by Lai and Mow (1980) is used to describe the dependence on the permeability to the volume change:

$$k = k_0 \, e^{M(\lambda - 1)} \tag{V.2.1}$$

It is consistent with remarks made in Sec. III.5 as it implies that compression rapidly hinders fluid flow with the intrinsic permeability k decreasing from its value k_0 in the undeformed state. The positive and dimensionless material parameter M controls the curvature of the nonlinear change in the permeability when the mixture experiences volume change. The interested reader can refer to Lai et al. (1981) for a study investigating the sensitivity of the biphasic model to various permeability parameters. For illustration purposes, Fig. V.2 shows how the permeability varies for various values of M.

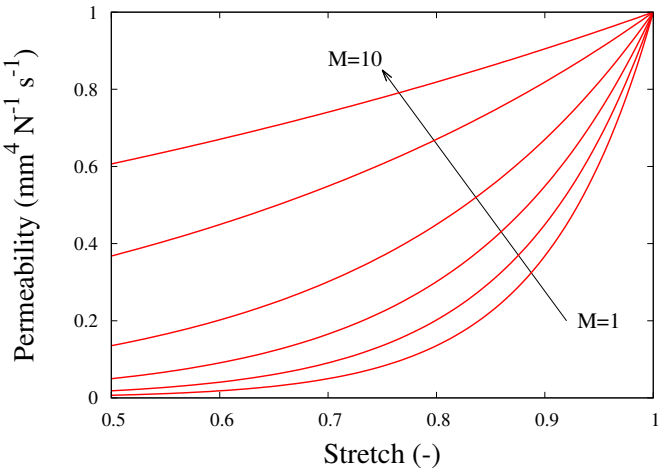

Figure V.2: Sensitivity of the strain dependent permeability on the parameter M ($k_0 = 1$)

The strain-dependent permeability is linearised in order to evaluate the tangent stiffness matrix:

$$\delta k = \hat{k} M \nabla_0 \delta u \tag{V.2.2}$$

V.2.2 Swelling pressure and reference state

Whether *in-vitro* or *in-vivo*, defining a physiological reference state for the strain of the tissue is a recurring issue (see for example discussion in Karajan (2009) or later in Sec. VI.1.1). The nucleus is predominantly governed by the fluid flow through the solid matrix and its water content, which makes the state of the tissue highly dependent on the loading history. Additionally, the tissue is always under pre-stressed conditions in order to accommodate:

- the confining loads of the adjacent vertebrae and annulus fibrosus
- the swelling effects of the osmotic pressure
- the fluid pressure (except in the virtually impossible case, due to low permeability, of time-dependent equilibrium)

In order to preserve a close to physiological state, experiments are conducted *in-vitro* on samples harvested from spines that have been frozen soon after death. These are typically bovine tissues. Then, a possible way to define a reference state is to

choose this "preserved" state as the initial strain-free condition (which is obviously not accurate due to the physiological pre-straining, which is impossible to measure). The associated pre-stress can be taken into account by defining a swelling pressure σ_0, which represents the sum of the osmotic pressure and the elastic stress on the solid at equilibrium (Yao et al., 2002):

$$\sigma_0 = \pi_0 + \sigma_0^e \tag{V.2.3}$$

Experimentally, σ_0 represents the load that needs to be applied onto the thawed sample to maintain it at the physiological strain state (i.e. the frozen state). It is estimated in Heneghan and Riches (2007) that at any level of compression, the initial ionic osmotic pressure π_0 represents about 70% of the swelling pressure. Therefore, the initial solid stress σ_0^e (which also includes the non-ionic osmotic pressure) accounts for the remaining 30% and we have:

$$\begin{cases} \sigma_0^e & = 0.3\sigma_0 \\ \pi_0 & = 0.7\sigma_0 \end{cases} \tag{V.2.4}$$

This assumption allows the number of material parameters of the model to be reduced.

V.2.3 Osmotic pressure

Most publications using biphasic swelling models (e.g. Schroeder et al. (2006), Wilson et al. (2005b), Ehlers et al. (2008)) derive the osmotic contribution from the Donnan equation, the electro-neutrality condition and Van't Hoff osmotic law, to obtain:

$$\Delta\pi = \left(\sqrt{\bar{c}_m^2 + \left(\frac{c_{0S}^{fc} n_{0S}^F}{2\left(\lambda - n_{0S}^S\right)} \right)^2} - \bar{c}_m \right) \tag{V.2.5}$$

This model requires the following material parameters: the initial porosity n_{0S}^F (or solidity n_{0S}^S), the initial molar concentration c_{0S}^{fc} and the molar concentration of the external monovalent solution surrounding the tissue $\bar{c}_m$.

However, in the present formulation, we propose the use of a simpler power law derived from confined compression tests in Heneghan and Riches (2008a):

$$\Delta\pi = \frac{\pi_0}{\lambda^m} \tag{V.2.6}$$

where π_0 represents the ionic osmotic pressure in the initial state, which is determined according to Eq. V.2.4. The dimensionless parameter m controls the non-linearity. This law is phenomenologically motivated by the fact that osmotic effects arise from changes of concentration of proteoglycans (see Chapter II). The biphasic swelling model relies on the assumptions that these are attached to the solid matrix (this is the Lanir hypothesis described in Sec. III.4) and as such, the volume changes measured by λ in 1D are representative of changes in concentrations of proteoglycans.

In Heneghan and Riches (2008a), it appears that using m=2 is an acceptable approximation. This implies that the osmotic contribution can be determined with only one parameter (π_0), which is derived from σ_0^e measured at equilibrium.

The corresponding linearised term is:

$$\delta\left(\Delta\pi\right) = -\frac{m\hat{\Delta\pi}}{\lambda}\nabla_0\delta\mathbf{u} \tag{V.2.7}$$

V.2.4 Solid phase

The solid phase is modelled using the well established strain energy function proposed in Holmes and Mow (1990). In 1D, the Cauchy stress takes the form:

$$\sigma^e(\lambda) = \frac{1}{2}H_m\left(\frac{\lambda^2-1}{\lambda^{2\beta+1}}\right)e^{\beta\left(\lambda^2-1\right)} + \sigma_0^e \tag{V.2.8}$$

Note that the initial solid stress $\sigma^e(\lambda=1) = \sigma_0^e$ is accounted for. β is a dimensionless parameter that controls the degree of nonlinearity and H_m is the stiffness modulus of the solid phase at zero strain (i.e. the shear modulus in the small strain regime):

Following the arguments made in the previous section, obtaining a set of material parameters (H_m,β) for the solid phase in a consistent manner represents a significant challenge since the state $\lambda = 1$ is itself, to some extent, unknown.

$$H_m = \frac{\partial\sigma^e}{\partial\lambda}_{|\lambda=1} \tag{V.2.9}$$

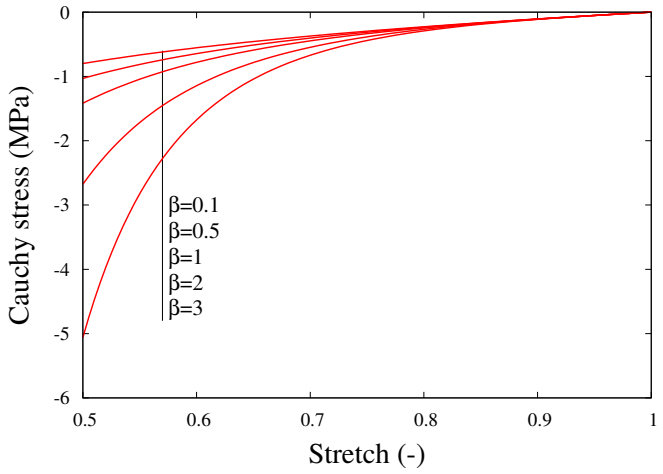

Figure V.3: Sensitivity of the Cauchy stress to the parameter β ($H_m = 1$)

Finally, the elasticity tensor is derived to account for the material nonlinearities. In the context of a total-Lagrangian formulation, the Lagrangian elasticity tensor is defined as:

$$\mathcal{C} = 2\frac{\partial \mathbf{S}^e(\mathbf{C})}{\partial \mathbf{C}} \xrightarrow{1D} \mathcal{C} = 2\frac{\partial S^e(C)}{\partial \lambda^2} \tag{V.2.10}$$

In Eq. V.2.10, the right Cauchy-Green strain tensor was reduced for the 1D problem as follows:

$$\mathbf{C} = \mathbf{F}^{\mathrm{T}}\mathbf{F} \xrightarrow{1D} C = \lambda^2 \tag{V.2.11}$$

Eq. V.2.10 also requires the derivation of the second Piola-Kirchhoff stress, which is simply obtained from Eq. V.2.8 using Eq. V.1.4:

$$S^e = \frac{1}{2}H_m\left(\frac{\lambda^2-1}{\lambda^{2\beta+2}}\right)e^{\beta\left(\lambda^2-1\right)} + \frac{\sigma_0^e}{\lambda} \tag{V.2.12}$$

Finally, the Lagrangian elasticity tensor takes the form:

$$\mathcal{C} = \frac{\beta\left(\lambda^2+\lambda^{-2}-2\right)+\lambda^2}{\lambda^{2\beta+2}}H_n e^{\beta\left(\lambda^2-1\right)} - \frac{\sigma_0^e}{\lambda^3} \tag{V.2.13}$$

V.3 The 1D updated-Lagrangian formulation

Finally, the full set of equations required for the Newton-Raphson implementation of the biphasic swelling problem in 1D is presented. The system of equation is the same

as presented in Chapter IV and recalled here:

$$\begin{bmatrix} \mathbf{K}_{uu} & \mathbf{K}_{up} \\ \mathbf{K}_{pu} & \Delta t\,\mathbf{K}_{pp} \end{bmatrix} \begin{Bmatrix} \delta\mathbf{u} \\ \delta\mathbf{p} \end{Bmatrix} = \begin{Bmatrix} \mathbf{F}_u^{ext} \\ \Delta t\,\mathbf{F}_p^{ext} \end{Bmatrix} - \begin{Bmatrix} \mathbf{F}_u^{int} \\ \Delta t\,\mathbf{F}_p^{int} \end{Bmatrix} \tag{V.3.1}$$

Subsequently, the elemental stiffness matrix and elemental force vectors are obtained by a pull-back operation (i.e. the inverse transformation of Eq. IV.2.4) on Eq. IV.3.8, and the relationships derived in the current chapter. Remembering that displacements and pressure are respectively approximated by quadratic 3-node elements and linear 2-node elements, these can be expressed in index notation as:

$${}^eK_{uu}(i,j) = \int_L \frac{dN_i^u}{dX}\left(\hat{S}^e + \mathcal{C}\lambda^2 - \frac{m\pi_0}{\lambda^{m+1}}\right)\frac{dN_j^u}{dX}A\,dX \quad i,j \in \{1,2,3\} \tag{V.3.2a}$$

$${}^eK_{up}(i,j) = \int_L \frac{dN_i^u}{dX}N_j^p A\,dX \quad i \in \{1,2,3\}\ j \in \{1,2\} \tag{V.3.2b}$$

$${}^eK_{pu}(i,j) = \int_L \left(N_i^p + \frac{1}{\lambda^3}\frac{dN_i^p}{dX}\frac{d\hat{p}^e}{dX}\right)\frac{dN_j^u}{dX}A\,dX \quad i \in \{1,2\}\ j \in \{1,2,3\} \tag{V.3.2c}$$

$${}^eK_{pp}(i,j) = \int_L \frac{1}{\lambda}\frac{dN_i^p}{dX}\hat{k}\frac{dN_j^p}{dX}A\,dX \quad i,j \in \{1,2\} \tag{V.3.2d}$$

$${}^eF_u^{int}(i) = \int_L \frac{dN_i^u}{dX}\left(\hat{S}^e\lambda - (\hat{p}^e + \hat{\Delta\pi}^e)\right)A\,dX \quad i \in \{1,2,3\} \tag{V.3.2e}$$

$${}^eF_p^{int}(i) = \int_L \left(N_i^p\frac{d\hat{v}^e}{dX} + k\frac{d\hat{p}^e}{dX}\frac{dN_i^p}{dX}\frac{1}{\lambda}\right)A\,dX \quad i \in \{1,2\} \tag{V.3.2f}$$

$${}^eF_u^{ext}(i) = \int_A N_i^u\bar{t_0}dA \quad i \in \{1,2,3\} \tag{V.3.2g}$$

$${}^eF_p^{ext}(i) = \int_A N_i^p\bar{g_0}dA \quad i \in \{1,2\} \tag{V.3.2h}$$

For completeness, it should be mentioned that numerical integrations are performed using a 3-point Gaussian quadrature.

V.4 Correlation with experimental data

The aim of this section is to show that, with carefully chosen parameters, the 1D biphasic swelling model can replicate experimental confined compression tests. The performances are assessed by fitting the numerical model to experimental data, courtesy of Dr Riches (from data published in Riches (2010) and Riches (2012)). Bovine tail intervertebral discs (non-degenerated) were harvested within hours of slaughter and frozen with the intention of preserving a close to physiological state. Samples

of diameter 10mm and approximate thickness 1mm were punched from the nucleus pulposus and placed in the apparatus described in Fig. V.1, where the bathing solution is an isotonic saline solution (0.15 mol/L NaCl). During the thawing process, the force applied onto the top platen to maintain the sample thickness was recorded and represents the swelling force $\sigma_0 A$ in the reference configuration. The samples are then subjected to a 10% ramp-hold compression test at a rate of $\sim$1 μm.s^{-1}(see Fig. V.4a).

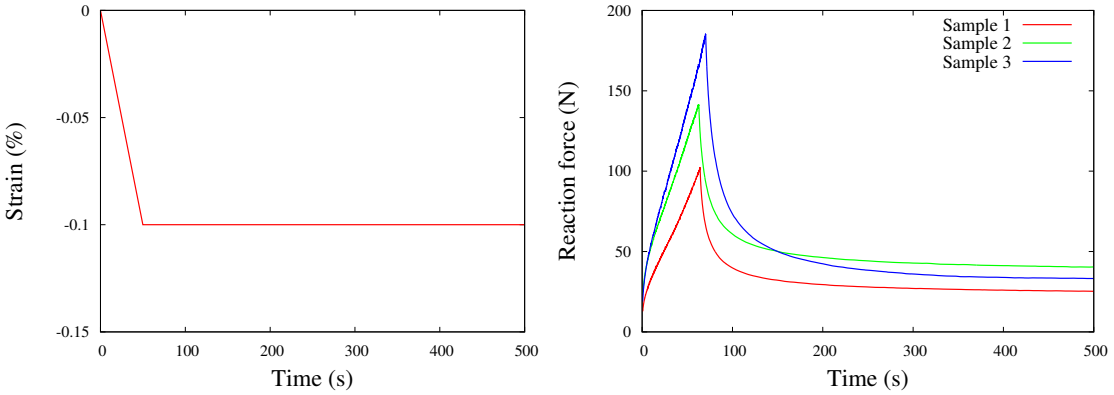

(a) Imposed loading

(b) Recorded reaction force

Figure V.4: Experimental reaction force for 3 typical bovine tail samples subjected to 10% compression followed by hold events

Fig. V.4b plots, for a selection of three samples, the force that was applied to the top platen in order to obtain the linear strain ramp loading. The nonlinearity of the response, typical of soft tissues under compression (e.g. Holmes et al. (1985), Iatridis et al. (1998)), will be further analysed in the following section. The large discrepancies (see Fig. V.4b) in swelling force (13-24N), peak force (102-185N) and equilibrium force (23-37N) are not unusual in the experimental analysis of soft tissues and can be explained in numerous ways (see for example Perie et al. (2005) and Recuerda et al. (2011)). These include the difficulty to obtain samples of even thickness (1014-1267 μm in the present case), the repeatability of the experiment, the impact of the sample's preparation but also the intrinsic properties of the sample (e.g. water and GAG content, age ...).

In order to tune the model to fit the experimental data, the set of material parameters is determined as follows: π_0 is derived from the initial swelling force, and then H_m is chosen to accommodate the equilibrium force (i.e. at steady state), that is when the pressure has dropped to zero and the fluid flow (and therefore the permeability) is not impacting on the mixture's total stress. Ideally, the solid properties (H_m,β) would be determined together using a plot of force vs strain at equilibrium; fortunately,

in the range of 10%, the solid nonlinearities are limited, minimising the role of β, which was then chosen from the literature. Finally, the parameters k_0 and M are chosen to fit both the peak load and the curvatures, with the help of the sensitivity study undertaken by Lai et al. (1981) to understand the relative influence of β and k_0 on the curvature and peak load. Note that a mesh convergence study revealed that 20 elements were sufficient in order to accurately capture smooth pressure gradients across the sample.

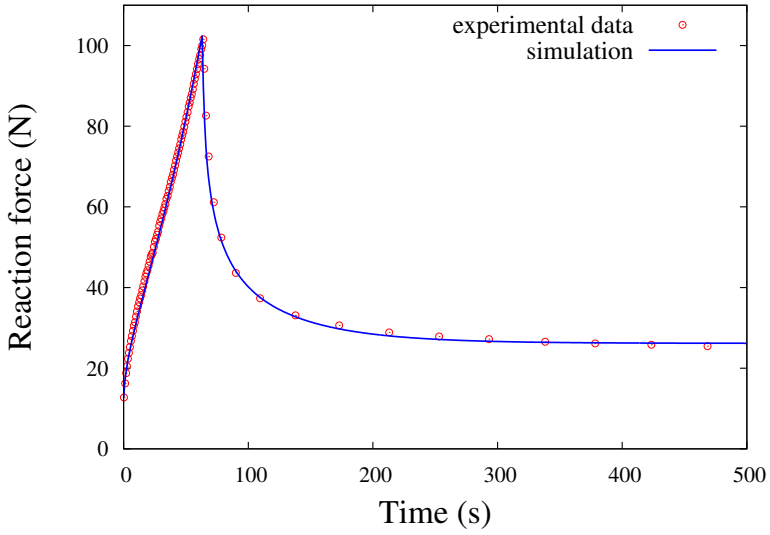

k_0=0.56×10^{-3} mm^4 N^{-1} s^{-1}
M=6.2
H_m=1.2 MPa
β=0.31
π_0=0.111 MPa

Figure V.5: Correlation between experimental and numerical reaction for Sample 1

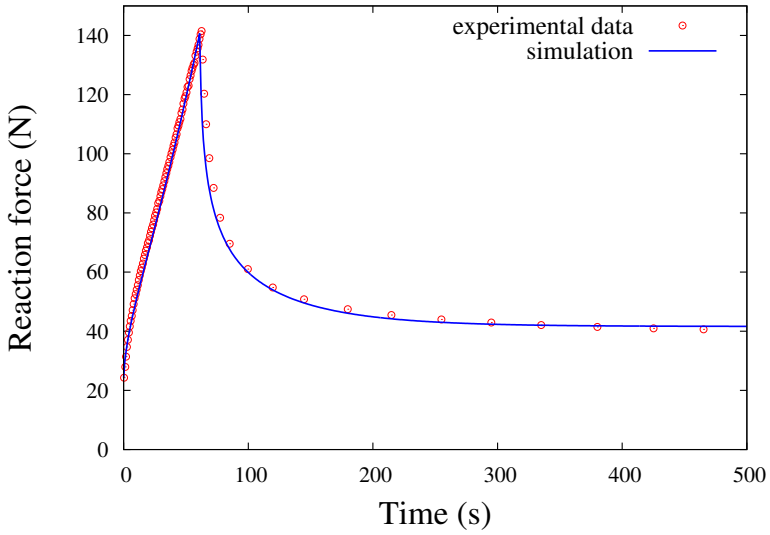

k_0=0.36×10^{-3} mm^4 N^{-1} s^{-1}
M=5.6
H_m=1.4 MPa
β=0.3
π_0=0.212 MPa

Figure V.6: Correlation between experimental and numerical reaction for Sample 2

The set of chosen parameters falls into the range found in the literature (see for exam-

ple Heneghan and Riches (2008b) and references therein). However, it is important to bear in mind that the proposed set of parameters represents only *one* solution among a larger space of possible sets. Riches (2012) warns that in this type of inverse analysis, contrasting combinations of parameters, including parameter without physiological ground, can produce comparable results.

V.5 Internal mechanisms in confined compression

This section aims to illustrate how simple computational models can complement experimental work to understand the internal processes of the intervertebral disc and provide valuable information, for example, in mechano-biology. In particular, emphasis is placed on the understanding of the prevalence of the fluid flow on the overall behaviour of the mixture, as suggested throughout Chapter III. To do so, the "Sample 1" described previously (Fig. V.5) is analysed in more details.

A possible approach to understanding what makes the response of the tissue nonlinear and why the peak force can be three times larger than the equilibrium force, is to start by relating the volume change of the mixture to the imposed loading. In confined compression, the prescribed displacement indirectly measures the volume change of the whole sample (as $J = \lambda$) which, in the context of constituent intrinsic incompressibility, also accounts for the volume of fluid expelled from the sample (see Sec. III.3.2). This is illustrated in Fig. V.7, where the flux of fluid at the free-flow boundary (top of the sample) is equal to the rate of loading, i.e. is constant.

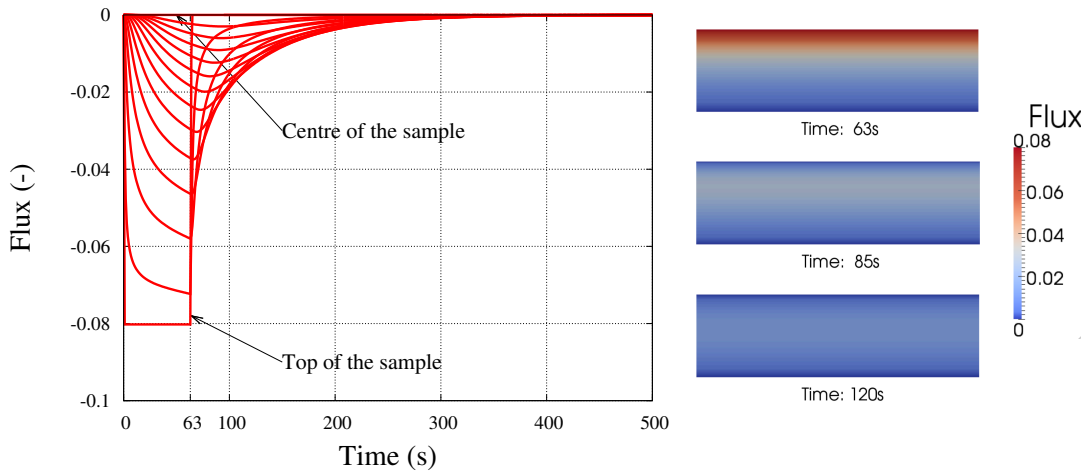

Figure V.7: Flux vs time in sample 1

The low (in relation to the loading rate and the sample's length) permeability hinders

the ability of the fluid to flow from the centre to the top, resulting in different levels of hydration throughout the depth of the sample. This defines two distinct regions associated with the load transfer mechanism. The first region, located near the free-flow boundary at the top, is dominated by high local solid deformation (Fig. V.8): the fluid does not have the ability to pressurize as it is squeezed out of the cylinder. At the end of the loading ramp, the top 30% of the sample experience stretches that are larger than the overall 10% applied, reaching a maximum of 55% at the top.

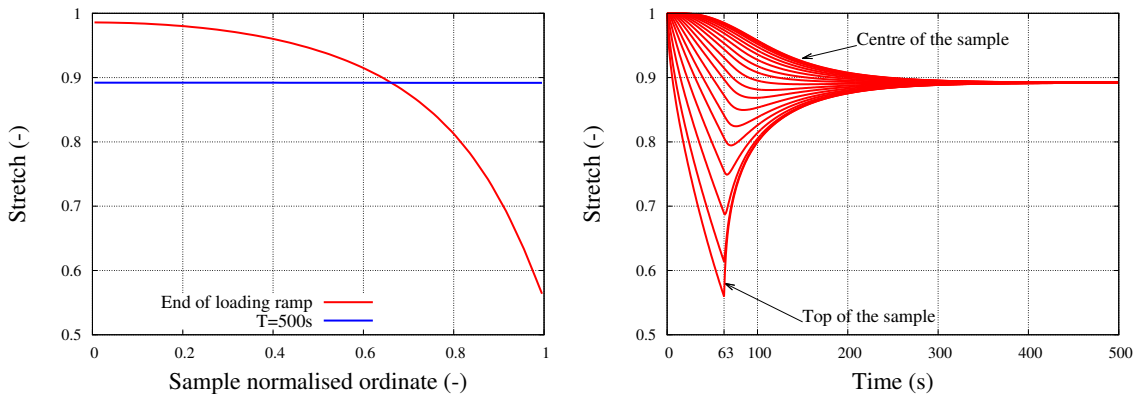

(a) Stretch along sample

(b) Stretch at different positions in the sample

Figure V.8: Stretches in sample 1

The second region, situated at the centre of the cylinder, is predominantly subjected to fluid pressurisation due to the fact that the low permeability is confining the fluid at the centre of the cylinder. Note that this results in relatively high gradients of pressure near the boundary (Fig. V.9a), requiring sufficiently dense meshes to capture this behaviour.

Due to this behaviour, material nonlinearities related to strains are locally triggered at the top of the sample, which experiences an increase of osmotic pressure and a decrease of permeability. Physiologically, these two mechanisms aim at protecting the tissue from experiencing excessive strain levels: the swelling increase locally offers extra stiffness to the mixture, while a decreased permeability induces higher levels of fluid pressurisation.

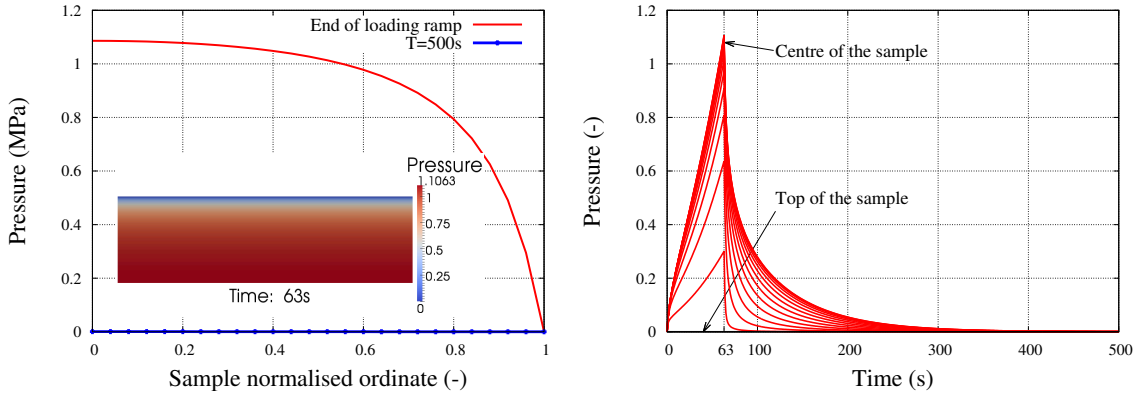

(a) Pressure along sample

(b) Pressure across sample

Figure V.9: Hydrostatic pressure distribution in sample 1

During the relaxation phase ($t \geq 63s$), the fluid flows internally from the highly hydrated and pressurised centre of the specimen toward the boundary, and slowly the fluid and strain distributions adjust across the sample, until equilibrium is reached ($p = 0$, $q = 0$, $\lambda = 0.9$ throughout). At every time t and for each cross-section of the sample, the total stress (i.e. the reaction force divided by the cross section area) is apportioned between the fluid pressure, the osmotic pressure and solid stress:

$$\sigma(x,t) = \sigma^e(x,t) - p(x,t) - \Delta\pi(x,t) \tag{V.5.1}$$

In order to analyse the load carrying mechanisms across the sample, the solid stress, fluid pressure and osmotic pressure are normalised by the total stress σ (see Fig. V.10b and V.10c) during the ramp and creep events. Although the magnitude of these results must be taken with care, as they highly depend on the choice of constitutive equations and parameters (see Fig. V.10a), they highlight observations made in previous sections: under dynamic loading, the response of the highly hydrated IVD is dominated by fluid pressurisation, which protect the solid matrix under rapid/shock loading. The low permeability delays the time at which steady state is reached, which occurs when equilibrium is achieved between external forces, solid stress and osmotic pressure. The high compressive strains at the top induce compaction of the solid phase, which is equivalent to increasing the concentration of proteoglycans and therefore increasing the osmotic pressure.

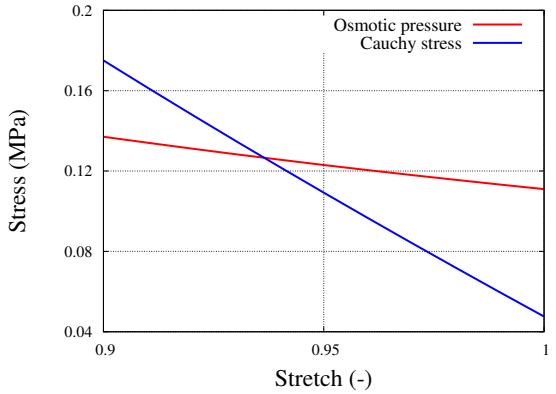

(a) Constitutive models

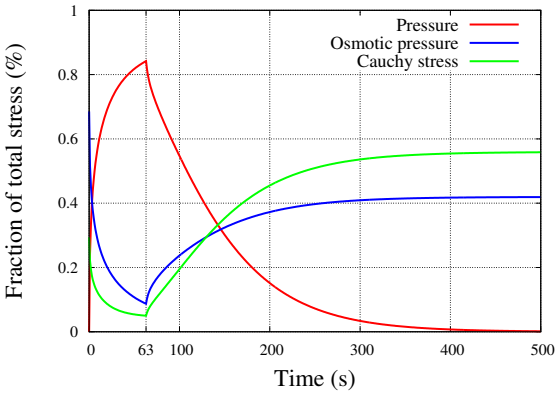

(b) Sample centre

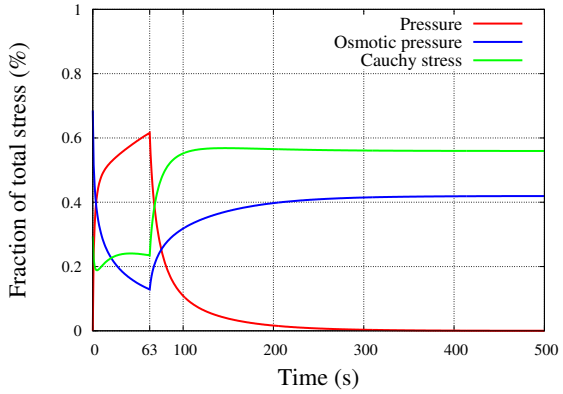

(c) 20% length from top

Figure V.10: Cauchy stress and osmotic pressure vs time (a), evolution of the stress distribution over time at the centre of the sample (b) and near the top surface (c)

V.6 Conclusions

The biphasic swelling model derived in previous sections was formulated for the one dimensional case. This allowed validation of the proposed model and demonstration of its capabilities to replicate experimental confined compression tests, as well as understand some of the internal mechanisms of the disc. It also highlighted the difficulty in obtaining material parameters (7 in the 1D case) and supports the modelling choice of the biphasic swelling model, but also neglecting visco-elastic phenomena. This paved the way for the more complex three dimensional implementation of the model, and in particular for the introduction of anisotropy.

Chapter VI

The 3D Biphasic Swelling Model

The focus of this section is the development of the three dimensional biphasic swelling model. Constitutive relationships for each constituent are presented, with particular emphasis on the transversely isotropic annulus fibrosus. Following a brief description of the C/C++ code specifically written for the current application, a methodology to verify the correct implementation of the biphasic swelling model is designed. Finally, convergence of the Newton-Raphson iterative solver is illustrated on simple benchmark tests.

VI.1 Constitutive relations

In a similar fashion to the 1D model, the biphasic swelling model is specialised in this section to the particular case of the intervertebral disc, by selecting a set of constitutive relationships characterising the solid phase, the strain dependent permeability and the osmotic pressure. The solid phase, which comprises the isotropic ground matrix and the collagen fibres of the annulus fibrosus, is described by an additive decomposition of its strain energy functions (Spencer, 1984):

$$W^S = W^S_{\text{matrix}} + W^S_{\text{fibre}} + W^S_{\text{interactions}} \tag{VI.1.1}$$

The term $W^S_{\text{interactions}}$ accounts for the energy generated by potential interactions between the solid matrix and the fibres. This automatically implies (see Eq. III.3.23) a similar split for for the stress tensor:

$$\boldsymbol{\sigma}^e = \boldsymbol{\sigma}^e_{\text{matrix}} + \boldsymbol{\sigma}^e_{\text{fibre}} + \boldsymbol{\sigma}^e_{\text{interactions}} \tag{VI.1.2}$$

VI.1.1 The isotropic part

(a) The solid matrix

In this work, the nucleus pulposus, the ground substance embedding the fibres of the annulus and the endplates are assumed to be perfectly isotropic, i.e. $W^S_{\text{fibre}} = W^S_{\text{interactions}} = 0$. The solid phase is simply described by a Neo-Hookean model (see Bonet and Wood (2008)):

$$W^S_{\text{matrix}} = \frac{\mu}{2}(I_1 - 3) - \mu \ln J + \frac{\lambda}{2}(\ln J)^2 \tag{VI.1.3}$$

where $I_1 = \text{tr}(\mathbf{C}_S)$ is the first invariant of the Cauchy-Green tensor $\mathbf{C}_S = \mathbf{F}_S^{\text{T}}\mathbf{F}_S$. This expression is usually used for compressible single phase materials. However, here J measures the volume change of the mixture and the last two terms are interpreted as the response of the solid matrix to volumetric changes of the mixture (i.e. the hydrated porous solid).

Following the derivation in Eq. III.3.23, the associated Cauchy stress tensor is evaluated as follows (with $\mathbf{b} = \mathbf{F}_S\mathbf{F}_S^{\text{T}}$):

$$\boldsymbol{\sigma}^e_{\text{matrix}} = 2J^{-1}\mathbf{F}_S\frac{\partial W^S_{\text{matrix}}}{\partial \mathbf{C}_S}\mathbf{F}_S^{\text{T}} = \frac{\mu}{J}(\mathbf{b} - \mathbf{I}) + \frac{\lambda}{J}(\ln J)\,\mathbf{I} \tag{VI.1.4}$$

(b) The permeability

As suggested in Sec. III.3.3 and further motivated in Sec. III.3.3, the permeability is described by a strain-dependant isotropic tensor $\mathbf{K} = k\mathbf{I}$, and the chosen model:

$$k = k_0\, e^{M(J-1)} \tag{VI.1.5}$$

is a simple extension of the one dimensional relationship derived in Lai and Mow (1980). The axial stretch is generalised in 3D by the volume change of the mixture J. This can be physically interpreted as a permeability that is exponentially decreasing as the level of compaction increases.

The linearised permeability term that is required in Eq. IV.3.8c, is derived:

$$\begin{aligned}\delta k &= k_0 \exp^{M(J-1)}\delta J \\ &= MkJ\left[\mathbf{F}_S^{-1} : (\text{grad}\,\delta\mathbf{u})\,\mathbf{F}_S\right]\end{aligned} \tag{VI.1.6}$$

where use was made of the linearised jacobian δJ derived in Eq. IV.2.11.

(c) The osmotic contribution

Stemming from two physical observations made in Chapter II, namely that:

1. the osmotic pressure is directly related to gradients of concentration of proteoglycans
2. proteoglycans are large molecules that are trapped in the matrix of collagen fibres and cannot leach out of the intervertebral disc

and further motivated in Sec. III.4, the biphasic swelling model is built on the assumption that the osmotic pressure can be constitutively derived, and expressed as a function of solid deformations (Sec. III.4). We therefore propose to relate the osmotic pressure to the volume change of the mixture $J = \det \mathbf{F}_S$, thus extending the 1D model derived in Heneghan and Riches (2008a) in a similar manner to the permeability:

$$\Delta\pi = \frac{\pi_0}{J^m} \tag{VI.1.7}$$

Analogously, the linearised osmotic pressure term required in Eq. IV.3.8a is derived:

$$\begin{aligned} \delta\Delta\pi &= \frac{-m\pi_0}{J^{m+1}}\delta J \\ &= -\Delta\pi \left[\mathbf{F}_S^{-1} : (\operatorname{grad}\delta\mathbf{u})\,\mathbf{F}_S\right] \end{aligned} \tag{VI.1.8}$$

Remembering the derivation of Chapter III.3, together with $\boldsymbol{\sigma}^e = \boldsymbol{\sigma}^e_{\text{matrix}} + \boldsymbol{\sigma}^e_{\text{fibre}}$, the total stress writes:

$$\mathbf{T} = \boldsymbol{\sigma}^e - \Delta\pi\mathbf{I} - p\mathbf{I} \tag{VI.1.9}$$

Eq. VI.1.9 clearly shows that the proposed osmotic law gives rise to an initial total stress in the reference state (i.e. when $\mathbf{u}^S = \mathbf{0}$ and p=0):

$$\mathbf{T}_{|\mathbf{u}^S=\mathbf{0},p=0} = \pi_0\mathbf{I} \tag{VI.1.10}$$

The definition of an initial state for the tissue that is physiologically meaningful is a recurring issue in the modelling of soft tissues and of the intervertebral disc in particular (see discussions in Chapters V and VIII). At this stage, there are essentially two strategies to tackle this problem, which are discussed in more depth in Karajan (2009). It is possible to:

1. Consider that the initial geometry (e.g. mesh obtained from *in-vivo* medical imagery) is in a stress- and deformation-free configuration. This is artificially enforced by subtracting the initial osmotic pressure from the total stress. This can, for example, be interpreted as a volumetric prestress of the solid:

$$\mathbf{T} = (\boldsymbol{\sigma}^e - \pi_0\mathbf{I}) - \Delta\pi\mathbf{I} - p\mathbf{I} \quad \rightarrow \quad \mathbf{T}_{|\mathbf{u}^S=\mathbf{0},p=0} = \mathbf{0} \tag{VI.1.11}$$

2. Assume that the initial geometry, is a virtual temporary configuration that is stress-, deformation- but also osmotic pressure-free. In this case, prior to any mechanical loading, the model is first solved for an incremental increase of osmotic pressure, up to the required level, allowing to find a set of solid stresses balancing the osmotic distribution.

Unfortunately, tissues within the intervertebral disc always are (and have been) subjected to a certain level of loading. This is due to a combination of the compressive loads imposed by adjacent vertebral bodies, the distribution of fluid pressure resulting from low permeability of the tissue, the osmotic pressure distribution and the complex interaction between the annulus fibrosus and the nucleus pulposus. Therefore, defining a stress- *and* deformation-free configuration is physiologically not possible; it would require the separation of each sub-constituent of the IVD followed by relaxation and swelling until some non-physiological equilibrium is reached. This means that neither of the above approaches is fundamentally fully acceptable.

The main disadvantage of the first strategy is the lack of information about the stress state in the reference configuration; labelling this configuration as the strain-free configuration results in a shift of the origin of solid constitutive laws (matrix, fibres, osmotic pressure). However, it offers the advantage of conserving the initial *in-vivo* geometry.

The second approach is based on letting the tissues swell until a certain equilibrium is reached, obviously implying that the initial geometry is not preserved. Although it probably offers a more realistic initial stress-state within the disc (one can for example think of the state of the fibres confining the swelling isotropic nucleus, which are not stressed in the first approach as reported in Michalek et al. (2012)), one can also argue that the nonlinear swelling process is path dependant and can lead to a variety of equilibrium states. Furthermore, this approach is computationally more expensive.

Although imperfect, the first approach is implemented in this work, on the ground that it is physiologically more relevant than the second option, and simpler to implement. In practice, it implies the definition of an initial configuration for each

problem; all strain measures are then defined with respect to this reference configuration, which makes the concept of absolute strain not applicable. As a consequence, material parameters must be calibrated with respect to this configuration.

Note that the approach used in the 1D model was a variation of the first option, in the sense that the initial total stress is also imposed, but instead of to zero, to a pre-stress that is measurable in the laboratory. Indeed, in the case of confined compression (see Eq. V.2.3-Eq. V.2.8), the initial osmotic pressure could be physically interpreted as a *swelling* pressure and conveniently be converted to an axial compressive load at the boundaries, allowing a more refined initial state to be defined.

VI.1.2 The anisotropic annulus fibrosus

Chapter II shed light on the paramount role played by the annulus fibrosus in the overall behaviour of the intervertebral disc. The ability of the annulus fibrosus to sustain high pressurisation of the nucleus pulposus stems both from the arrangement of collagen fibres and their superior tensile properties. The annulus fibrosus was not accounted for in Chapter V but it is crucial to include a faithful representation of AF's fibres in a 3D model.

Further to early models that assigned stiffer properties to elements comprising the annulus fibrosus in an iso- or ortho-tropic manner (e.g. Martinez et al. (1997), Polikeit et al. (2004)), a vast amount of full disc models use reinforced composite elements made of discrete fibres modelled as springs that are superimposed on an isotropic matrix (e.g. Shirazi-Adl (1994), Noailly et al. (2005), Schmidt et al. (2010), Tang and Rebholz (2011)). Mesh dependency for the fibre representation and fibre discontinuity between elements are the two main limitations of these models, stemming from the fact that the stiffness of the springs is usually defined between two adjacent nodes.

In the context of the intervertebral disc, the mesh dependency associated with the fibres was bypassed in Schroeder et al. (2006, 2008), by using a model originally developed for articular cartilage in Wilson et al. (2005b,c): in the so-called fibril-reinforced model, the linear visco-elastic stress contribution of the fibres is evaluated at the continuum level and also takes into account the change of fibre orientation.

In an attempt to simplify the very general 9-parameter model of Klisch and Lotz (1999) based on 11 invariants, the first constitutive models were derived using experimental work performed on single lamellae of annulus fibrosus. This allows the strain energy to be only expressed as a function of the fourth invariant of the right Cauchy-Green tensor, defined as:

$$I_4 = \mathbf{a}_0 \cdot \mathbf{C}_S \mathbf{a}_0 = \lambda_a^2 \tag{VI.1.12}$$

where $\mathbf{a}_0$ is the unit vector characterising the direction of a single family of fibres in the reference configuration (see Fig. VI.1). I_4 can be physically interpreted as the square of the fibre stretch. A notable example is the exponential function proposed in Eberlein et al. (2001) and initially used with constant material properties on a FE motion segment but later refined in Eberlein et al. (2004) and Holzapfel et al. (2005) with further experimental work. One can also cite the polynomial law developed by Markert et al. (2005) and validated against the experimental work of Holzapfel et al. (2005), later used for two families of fibres in Ehlers et al. (2008).

Naturally, the models previously described have recently been enhanced to include several levels of refinement, such as the fibre-matrix interaction or potential failure mechanisms as described in Chapter II. For example, the fibril-reinforced model used in Schroeder et al. (2006) was enhanced in Schroeder et al. (2010) to account for the inter-lamellar connection through a secondary network of collagen fibrils as described in Pezowicz et al. (2006) and Schollum et al. (2008). As opposed to the model developed in Eberlein et al. (2001), where the strain-energy function was built from experiments on a single lamella of annulus fibrosus, the model presented in Wagner and Lotz (2004) was established based on experiments performed on cuts of annulus in all possible directions. This results in additional terms in the strain energy function to capture the aforementioned interactions. The interaction terms were further refined to specifically represent the shearing interaction between the matrix and the fibres (e.g. deBotton et al. (2006), Guo et al. (2007)) or both the inter-lamellar and fibre shearing phenomenon (Guerin and Elliott (2007), Hollingsworth and Wagner (2011)).

Based on arguments similar to Sec. III.6 for the visco-elasticity, the fibre-matrix and lamellae-lamellae shearing are neglected in a first approach, therefore implying $W^S_{\text{interactions}} = 0$ and $\boldsymbol{\sigma}^e_{\text{interactions}} = \mathbf{0}$ in the present formulation. The most recent models inevitably require additional parameters, which goes against the general philosophy of the present study. The model developed in Eberlein et al. (2001) is chosen, not for any particular physical reason as it is not the most advanced model, but rather because it has been successfully used in many studies (e.g. Nerurkar et al. (2008), Ayturk et al. (2010)), and served as a basis for more complex formulations (e.g. Guerin and Elliott (2007), Hollingsworth and Wagner (2011)). It also offers consistency with experimental data in Holzapfel et al. (2005) that is also being used to extract material parameters (see Chapter VIII).

As described in Chapter II and illustrated in Fig. VI.1a, the annulus is made up of

multiple lamellae, which comprise fibres organised in an alternating fashion ($\mathbf{a}_0$, $\mathbf{b}_0$, $\mathbf{a}_0$ ...). The selected model describes the behaviour of two consecutive lamellae as illustrated on Fig. VI.1b) with the following strain energy function:

$$W^S_{\text{fibre}}(I_4, I_6) = \sum_{\alpha=4,6} \frac{k_{1_\alpha}}{2k_{2_\alpha}} \left(\exp\left[2k_{2_\alpha} \left(I_\alpha - 1 \right)^2 \right] - 1 \right) \tag{VI.1.13}$$

In the above, I_6 is the sixth invariant of the right Cauchy-Green tensor and, similarly to I_4, measures the square of the fibre stretch of the second family of fibres:

$$I_6 = \mathbf{b}_0 \cdot \mathbf{C}_S \mathbf{b}_0 = \lambda_b^2 \tag{VI.1.14}$$

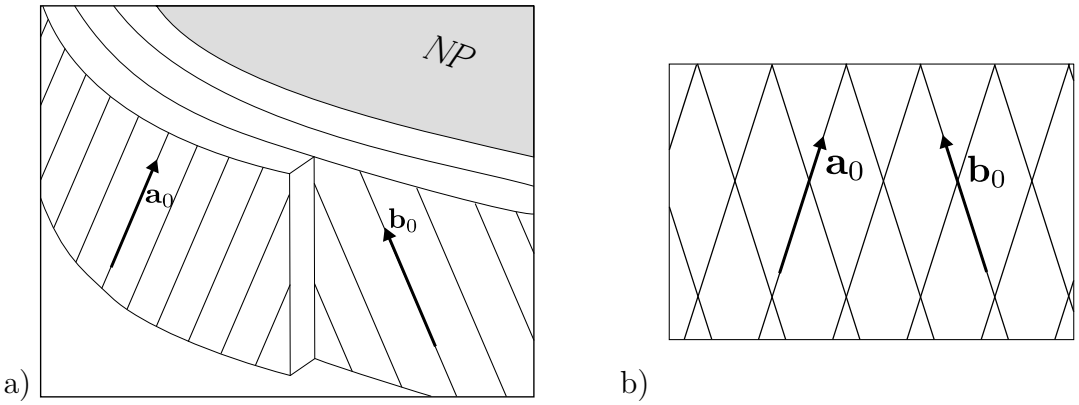

Figure VI.1: Two successive lamellae (a) and representation of two families of fibres (b)

It is reasonable to consider that two consecutive lamellae have similar properties: we therefore assume that $\mathbf{a}_0$ and $\mathbf{b}_0$ are symmetrical with respect to the axis of the disc and that their constitutive parameters are identical ($k_{1_4} = k_{1_6} = k_1$ and $k_{2_4} = k_{2_6} = k_2$). This assumption allows Eq. VI.1.13 to be reduced to:

$$W^S_{\text{fibre}}(I_4, I_6) = \frac{k_1}{2k_2} \left(e^{k_2 (I_4 - 1)^2} + e^{k_2 (I_6 - 1)^2} - 2 \right) \tag{VI.1.15}$$

Additionally, the collagen fibres are slender and crimped (see Chapter II) and, as such, are prone to buckling (e.g. Eberlein et al. (2001)). It is therefore appropriate to neglect their contribution under compressive strain; it is therefore additionally required that:

$$\begin{aligned} W^S_{\text{fibre}} &= 0 \qquad \text{if } I_i \leq 1, i \in \{4,6\} \\ &\geq 0 \qquad \text{if } I_i > 1, i \in \{4,6\} \end{aligned} \tag{VI.1.16}$$

The fibre strain energy function defined in Eq. VI.1.15 allows the Cauchy stress tensor of the fibres to be derived using Eq. III.3.23:

$$\begin{aligned} \boldsymbol{\sigma}^e_{\text{fibre}} =& 2J^{-1}\mathbf{F}\frac{\partial W^S_{\text{fibre}}}{\partial \mathbf{C}_S}\mathbf{F}^{\mathrm{T}} \\ =& J^{-1}\sum_{\alpha=4,6} 2k_1\left(\exp\left[k_2\left(I_\alpha-1\right)^2\right]\left(I_\alpha-1\right)\mathbf{F}\mathbf{a}_\alpha\otimes\mathbf{a}_\alpha\mathbf{F}^{\mathrm{T}}\right) \end{aligned} \tag{VI.1.17}$$

It is interesting to note in VI.1.17 that the Cauchy stress, which is a measure of the fibre stress in the current configuration, takes into account the rotation of the fibres as the mixture deforms with the term $\mathbf{F}\mathbf{a}_\alpha \otimes \mathbf{a}_\alpha\mathbf{F}^{\mathrm{T}}$.

VI.2 Implementation

A C/C++ code was specifically written for the implementation of the biphasic swelling model. The use of a few computational libraries alleviated this process:

The popular packages CBLAS and LAPACK are particularly efficient to manage small scale linear algebra. This involves all operations at the element level, starting from transformations to the iso-parametric space (e.g. handling of the shape functions and their derivatives, the evaluation of the jacobian matrix, its determinant and inverse), to the evaluation of quantities at the gauss-points (e.g. deformation and stress tensors) and the assembly of the elemental tangent stiffness matrices and force vectors.

The mesh oriented database MOAB (Tautges et al., 2004) is a very efficient and robust interface, optimised to handle metadata associated to meshes. Once provided with a mesh file, MOAB automatically generates a database containing nodes and their coordinates, as well as element connectivities. One of MOAB's main feature is the possibility to define any number of tags that can be attributed to chosen entities, whether it is a node, an element face or an element. This, for example, proves very useful to assign boundary conditions to a set of nodes or material properties to elements. MOAB is a very valuable tool for the evaluation of elemental tangent stiffness matrices and force vectors; it is typically used to iterate over all elements of

the mesh and for each of them, retrieve the nodal connectivities, nodal coordinates and any tag associated with this particular element. This data can then be passed on to other sub-routines and eventually determine $\mathbf{K}$ and $\mathbf{F}^{int}$.

Additionally, PETSc libraries (Balay et al., 2011a,b, 1997) are used to handle large scale computations, i.e. to solve the global (assembled) system of equations. PETSc includes an iterative solver that can be tuned (e.g. GMRES, LU) for our specific problem. It simply requires the definition of the tangent operator and the residual function as defined in Sec. IV.3 and a termination criterion as defined in Sec. IV.4.

Finally, a substantial number of post-processing routines were written, both in the main C/C++ code by defining tags with MOAB (e.g. matrix and fibre stress, principal stretches, Darcy's flux) and in python, in order to visualise and analyse the results.

VI.3 Verification procedure

The implementation of a full three-dimensional finite element code is a long and complex, tedious at times, task. It is likely that even the most conscientious developer will make mistakes during this process. Therefore, the design of a verification methodology is of crucial importance in order to track and isolate these inevitable implementation errors. The aim of this section is to formulate a strategic series of tests that are recommended to be followed to ensure a correct implementation of the biphasic swelling model. Interestingly, this process also offers a unique opportunity to gain understanding of the coupling mechanisms.

$$\begin{bmatrix} \mathbf{K}_{uu} & \mathbf{K}_{up} \\ \mathbf{K}_{pu} & \Delta t\,\mathbf{K}_{pp} \end{bmatrix} \begin{Bmatrix} \delta\mathbf{u} \\ \delta\mathbf{p} \end{Bmatrix} = \begin{Bmatrix} \mathbf{F}_u^{ext} - \mathbf{F}_u^{int} \\ \Delta t \left(\mathbf{F}_p^{ext} - \mathbf{F}_p^{int}\right) \end{Bmatrix} \tag{VI.3.1}$$

The discretised and linearised model is recalled in its most compact form in Eq. VI.3.1. In simple words, the tangent stiffness matrix operates on the right hand side until a set {$\mathbf{u}$,p}, that sufficiently minimises the residuals to meet the termination criteria defined in Sec. IV.4, is found. Unfortunately, achieving convergence only means that internal forces balance external forces, but it cannot guarantee a correct implementation of the problem. It is indeed possible to meet the termination criteria with an ill-defined $\mathbf{F}^{int}$, in which case the "converged solution" does not satisfy the governing equations. $\mathbf{F}^{int}$ is undoubtedly the most critical term to implement as it governs the quality of the solution, and as such will receive the main focus in this section. The tangent operator, is only responsible for the rate of convergence and

will be deemed correctly implemented upon acceptable rate of convergence.

The validation work is performed on a unit length cube (1mm) comprised of 261 tetrahedral elements (Fig. VI.2), with 508 nodes to describe the displacements and 88 nodes for the pressure (resp. quadratic and linear elements). The solid matrix is modelled with $\mu = 0.5$ MPa and $\lambda = 0.2$, the fibres with $k_1 = 1$MPa and $k_2 = 40$MPa. Tests are presented here in one direction, but have been performed in all three directions.

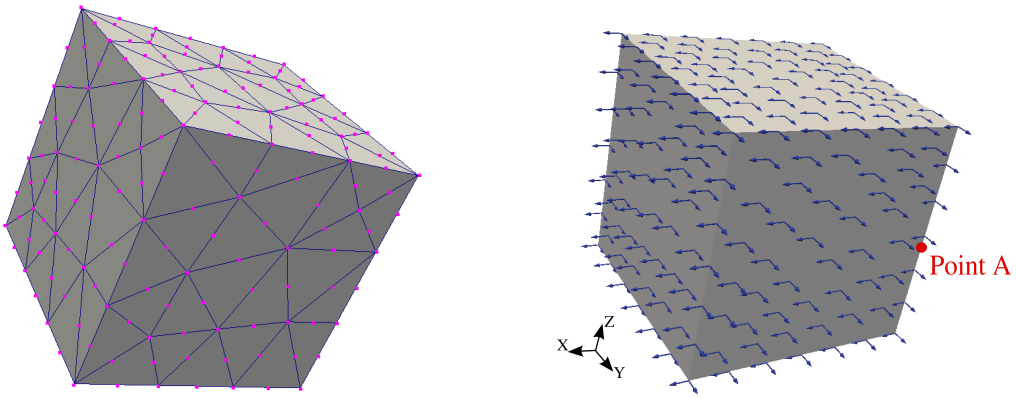

(a) Discretised cube (b) Orthogonal fibre distribution

Figure VI.2: Unit cube used for the verification procedure: a) discretisation with quadratic tetrahedrons - b) reinforced with two families of fibres: $\mathbf{a}_0$ in the X-direction, $\mathbf{b}_0$ in the Y-direction

Note that the preliminary tests performed on a single element (e.g. shape function implementation, jacobians, volume, surface area, etc.), although essential prior embarking on further verifications, are not presented here.

VI.3.1 The "right hand side"

The objective of this section is the verification of the implementation of the residuals, and in particular of the internal force vector. This is achieved by constraining the full state of the mixture, i.e. by imposing the primary variables $\mathbf{u}$ and p at every node, rather than at the essential boundaries only. As all degrees of freedom are prescribed, iterative calculations are not required, which effectively "turns off" the Newton-Raphson solver.

Let us first decompose the internal force vector into five contributions which can be interpreted as follows:

- $\mathbf{F}^{int}_{u,\text{solid}} = \int_v \{\nabla \mathbf{N}^u\}^{\mathrm{T}} \hat{\boldsymbol{\sigma}}^e \, dv$: solid contribution to the linear momentum balance

resulting from elastic deformations of the porous solid matrix.

- $\mathbf{F}^{int}_{u,\text{fluid}} = \int_v - \{\nabla \mathbf{N}^u\}^{\mathrm{T}} (\mathbf{N}^p \hat{\mathbf{p}}^e)\, dv$: fluid contribution to the momentum balance accounting for the fluid pressurisation (coupling term).
- $\mathbf{F}^{int}_{u,\text{osmo}} = \int_v \{\nabla \mathbf{N}^u\}^{\mathrm{T}} \left(\mathbf{N}^u \hat{\Delta\pi}^e\right) dv$: osmotic contribution to the momentum balance.
- $\mathbf{F}^{int}_{p,\text{fluid}} = \int_v - \{\nabla \mathbf{N}^p\}^{\mathrm{T}} k \nabla \hat{\mathbf{p}}^e\, dv$: force resulting from the fluid flow, driven by pressure gradients, through the solid matrix.
- $\mathbf{F}^{int}_{p,\text{solid}} = \int_v \mathbf{N}^p \nabla \cdot \hat{\mathbf{v}}^e\, dv$: force resulting from the fluid flow, induced by volume changes in the mixture, through the solid matrix (coupling term).

The key idea of the verification methodology is to strategically choose sets {**u**,p} that will decouple the above contributions and allow independent validation of each of them. Four mixture states are defined in the following sub-sections.

(a) Rigid body motion

In this preliminary test, the pressure is set to a non-zero constant (e.g. $p = 1$ at all pressure nodes) and the displacement degrees of freedom are chosen to describe an arbitrary rigid body motion:

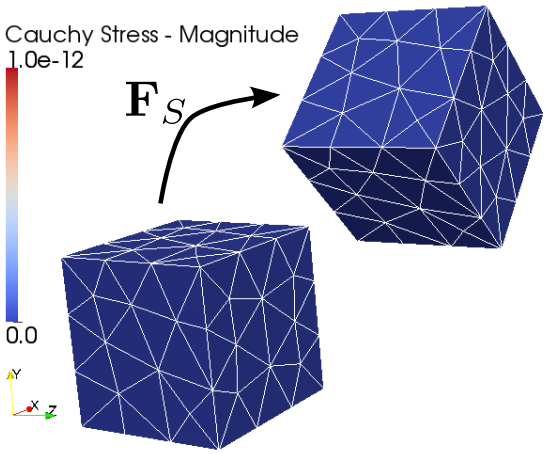

Figure VI.3: Unit cube subjected to a rigid body motion - Contour plot: norm of the stress tensor $\boldsymbol{\sigma}^e$

This test verifies that, when $\Delta\pi_0 = 0$:

- rotations and translations are not inducing any straining, therefore the deformation for the mixture are equal to the identity $\mathbf{F}_S = \mathbf{C}_S = \mathbf{b} = \mathbf{I}$, as well as the stretch of both families of fibres $\lambda_a = \lambda_b = 1$.
- the strain-free configuration is also stress-free: $\boldsymbol{\sigma}^e = \boldsymbol{\sigma}^e_{\text{matrix}} = \boldsymbol{\sigma}^e_{\text{fibre}} = \mathbf{0}$
- without any deformation or fluid flow, the internal force vectors are zero: $\mathbf{F}^{int}_u = \mathbf{F}^{int}_p = \mathbf{0}$

(b) Shearing

In this test, the cube is subjected to shearing with the intention to investigate the properties of an isochoric motion on the biphasic swelling model. At each node with coordinate (X, Y, Z), the pressure degrees of freedom are set to a constant and each material point is subjected to the motion defined in Eq. VI.3.2. This motion corresponds to simple shear in the XY-plane, γ defining the shearing angle.

$$\mathbf{x} = \chi(\mathbf{X}) = \begin{Bmatrix} X \\ Y \\ Z \end{Bmatrix} + \begin{Bmatrix} Y \tan\gamma \\ 0 \\ 0 \end{Bmatrix} \tag{VI.3.2}$$

The deformed geometry is illustrated on Fig. VI.4.

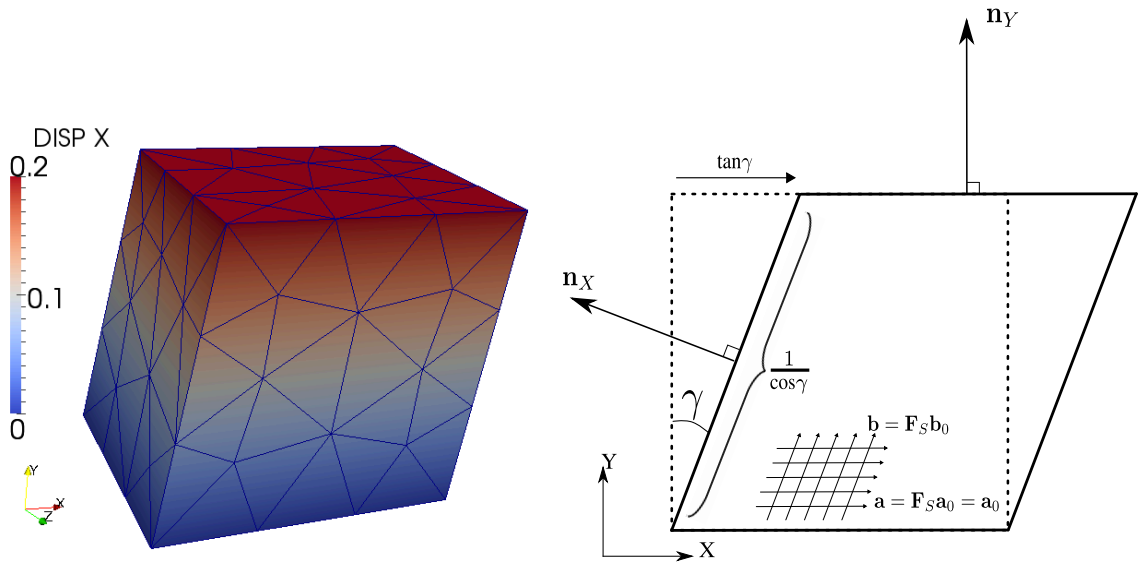

Figure VI.4: Sheared cube in XY-plane

Firstly, this test verifies that at every gauss point of every element:

- $\mathbf{F}^{int}_{p,\text{solid}} = \mathbf{0}$ as the isochoric motion does not induce any fluid flow resulting from solid deformation
- $\mathbf{F}^{int}_{p,\text{fluid}} = \mathbf{0}$ as no Darcy flow is induced in the absence of pressure gradients
- in the special case where the constant pressure is set to zero, solid and fluid phases are not interacting and $\mathbf{F}^{int}_{u,\text{fluid}} = \mathbf{0}$

In the particular case $\tan\gamma = 0.2$, we verify that at any point $\mathbf{X}$ of the cube, the gradient of deformation takes the form:

$$\mathbf{F}_S(\mathbf{X}) = \mathbf{I} + \frac{\partial \mathbf{x}}{\partial \mathbf{X}} = \begin{bmatrix} 1 & \tan\gamma & 0 \\ 0 & 1 & 0 \\ 0 & 0 & 1 \end{bmatrix} = \begin{bmatrix} 1 & 0.2 & 0 \\ 0 & 1 & 0 \\ 0 & 0 & 1 \end{bmatrix} \tag{VI.3.3}$$

After verifying that the volume is preserved at any gauss point ($J = \det \mathbf{F}_S = 1$), the Cauchy stress tensor of the matrix is evaluated using Eq. VI.1.4:

$$\boldsymbol{\sigma}^e_{\text{matrix}}(\mathbf{X}) = \frac{\mu}{J}\left(\mathbf{F}_S\mathbf{F}_S^{\mathrm{T}} - \mathbf{I}\right) + \frac{\lambda}{J}(\ln J)\,\mathbf{I} = \begin{bmatrix} 0.02 & 0.1 & 0 \\ 0.1 & 0 & 0 \\ 0 & 0 & 0 \end{bmatrix} \tag{VI.3.4}$$

As illustrated on Fig. VI.4, fibres oriented in the X-direction experience a body motion and are therefore neither stretched ($\lambda_a = \sqrt{I_4} = 1$) nor stressed ($\boldsymbol{\sigma}^e_{\text{fibre},a} = \mathbf{0}$). However, the fibres initially oriented in the Y-direction are stretched by a factor:

$$\lambda_b = \sqrt{I_6} = \sqrt{\mathbf{b}_0 \cdot \mathbf{C}_S\mathbf{b}_0} = 1.04 \tag{VI.3.5}$$

The fibre Cauchy stress tensor is evaluated owing to Eq. VI.1.17:

$$\boldsymbol{\sigma}^e_{\text{fibre},b} = 2k_1 J^{-1} \exp\left[k_2\left(I_6 - 1\right)^2\right](I_6 - 1)\left(\mathbf{F}\mathbf{b} \otimes \mathbf{b}\mathbf{F}^{\mathrm{T}}\right) \tag{VI.3.6}$$

$$= \begin{bmatrix} 0.0034 & 0.0171 & 0 \\ 0.0171 & 0.0853 & 0 \\ 0 & 0 & 0 \end{bmatrix} \tag{VI.3.7}$$

The above result can finally be projected in the fibres' direction in the current configuration as follows:

$$\sigma_b = \frac{1}{\left|\left|\mathbf{F}_S\mathbf{b}_0\right|\right|^2}\mathbf{F}_S\mathbf{b}_0 \cdot \boldsymbol{\sigma}^e_{\text{fibre},b}\left(\mathbf{F}_S\mathbf{b}_0\right) = 0.0887\,\text{MPa} \tag{VI.3.8}$$

Additionally, the resultant force can be analytically evaluated on each face by integrating the traction (see Eq. IV.1.2c) over the face area. The resultant force is a function of the face outward normal $\mathbf{n}$ and the face section a, both evaluated in the current configuration:

$$\mathbf{R} = \int_a \bar{\mathbf{t}}\, da = (\boldsymbol{\sigma}^e \cdot \mathbf{n})\, a \tag{VI.3.9}$$

This resultant force is then compared to its numerical counterpart, which is determined by summing the internal forces over all nodes of the face of concern:

$$\mathbf{R} = \sum_{\text{nodes on face}} \mathbf{F}^{int}_{u,\text{solid}} \tag{VI.3.10}$$

For example, the normal to the face X=-0.5mm is $\mathbf{n}_X = \{-\cos\gamma, \sin\gamma, 0\}$. This face section area, expressed in the current configuration is $a_X = 1/\cos\gamma$. With $\boldsymbol{\sigma}^e = \boldsymbol{\sigma}^e_{\text{matrix}} + \boldsymbol{\sigma}^e_{\text{fibre},b}$, it is found that the reaction force is:

$$\mathbf{R}_X = (\boldsymbol{\sigma}^e \cdot \mathbf{n}_X)\, a_X = \begin{bmatrix} 0.0234 & 0.1171 & 0 \\ 0.1171 & 0.0853 & 0 \\ 0 & 0 & 0 \end{bmatrix} \begin{Bmatrix} -\cos\gamma \\ \sin\gamma \\ 0 \end{Bmatrix} \frac{1}{\cos\gamma} = \begin{Bmatrix} 0 \\ -0.1 \\ 0 \end{Bmatrix} \tag{VI.3.11}$$

and we therefore verify that:

$$\sum_{\text{nodes (0.5,Y,Z)}} \mathbf{F}^{int}_{u,\text{solid}} = \begin{Bmatrix} 0 \\ -0.1 \\ 0 \end{Bmatrix} \tag{VI.3.12}$$

Similarly, the normal for the faces Y=0.5mm and Z=0.5mm are respectively $\mathbf{n}_Y = \{0, 1, 0\}$ and $\mathbf{n}_Z = \{0, 0, 1\}$, and the respective face areas in the current configuration are $a_Y = a_Z = 1$ mm^2. We verify that:

$$\sum_{\text{nodes (X,0.5,Z)}} \mathbf{F}^{int}_{u,\text{solid}} = (\boldsymbol{\sigma}^e \cdot \mathbf{n}_Y)\, a_Y = \begin{Bmatrix} 0.1171 \\ 0.0853 \\ 0 \end{Bmatrix} \tag{VI.3.13a}$$

$$\sum_{\text{nodes (X,Y,0.5)}} \mathbf{F}^{int}_{u,\text{solid}} = (\boldsymbol{\sigma}^e \cdot \mathbf{n}_Z)\, a_Z = \begin{Bmatrix} 0 \\ 0 \\ 0 \end{Bmatrix} \tag{VI.3.13b}$$

The above test was performed without any osmotic contribution (i.e. setting $\pi_0 = 0$). We can also verify, for example with $\pi_0 = 0.5$ MPa, that:

- the solid prestress defined in Eq. VI.1.11 is correctly added onto the solid stress, so that the total stress becomes:

$$\boldsymbol{\sigma}^e = \boldsymbol{\sigma}^e_{|\pi_0=0} + \Delta\pi = \begin{bmatrix} 0.5234 & 0.1171 & 0 \\ 0.1171 & 0.5853 & 0 \\ 0 & 0 & 0.5 \end{bmatrix} \tag{VI.3.14}$$

- $\Delta\pi = 0.5\,\mathbf{I}$ as the volume of the mixture remains constant.

(c) Dilatation with constant pressure distribution

In order to verify the proper behaviour under volumetric deformations, the cube is dilated by increasing the length of all its edges by 20% (see Fig.VI.5) while imposing a constant pressure distribution. The applied motion is:

$$\mathbf{x} = \chi(\mathbf{X}) = \begin{Bmatrix} 1.2X \\ 1.2Y \\ 1.2Z \end{Bmatrix} \tag{VI.3.15}$$

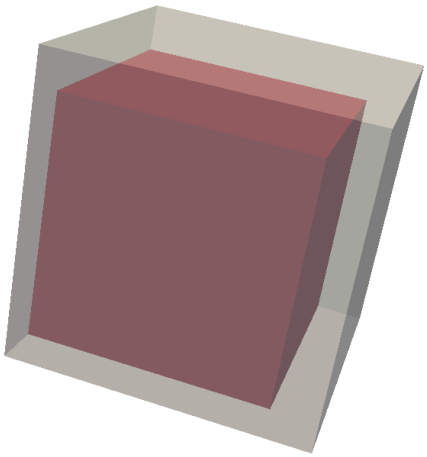

Figure VI.5: Dilated cube

In this case, the volume change of the mixture is solely driven by the prescribed volume change of the solid skeleton (div $\mathbf{v^S} \neq 0$) as Darcy flow cannot take place without any pressure gradient. We then confirm that at each gauss point of each element:

- $\mathbf{F}^{int}_{p,\text{fluid}} = \mathbf{0}$ since the seepage velocity is zero (see Eq. III.3.25)
- $\mathbf{F}^{int}_{u,\text{fluid}} = \mathbf{0}$ when the constant pressure is set to zero
- $\mathbf{F}^{int}_{p,\text{solid}} \neq \mathbf{0}$ (see discussion below)

As both the solid and the fluid are incompressible, it appears natural to compare the volume change of the cube to the fluid influx. When subjected to 20% dilatation, the change of volume of the cube is:

$$\Delta V = v - V = 1.2^3 - 1^3 = 0.728\text{mm}^3 \tag{VI.3.16}$$

However, the fluid flux resulting from volume changes of the mixture is calculated as follows:

$$\sum_{\text{nodes on 6 faces}} \Delta t\, \mathbf{F}^{int}_{p,\text{solid}} = -0.864 \neq -\Delta V \tag{VI.3.17}$$

This is due to the fact that, unlike previous tests where fluid and solid were fully decoupled, the term $\mathbf{F}^{int}_{p,\text{solid}}$ arises from linearisation of the mass balance in the direction of $\delta\mathbf{u}$. The nonlinearities arising from this coupling are therefore not captured properly for such large deformation (cubic function of the stretch of the edge). This is clearly illustrated in Fig. VI.6 where the equality $\Delta V = \sum_{\text{nodes on face}} \mathbf{F}^{int}_{p,\text{solid}}$ holds for small deformations.

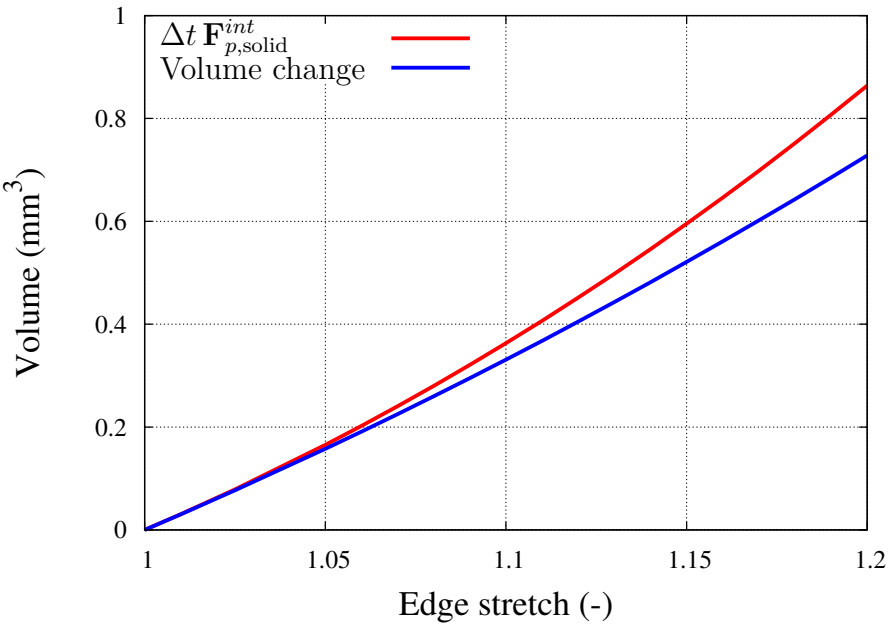

Figure VI.6: Comparison of the exact volume change to the linearised fluid influx

We also verify that the volumetric strain results in a volumetric stress-state. Similarly to the shear test, the Cauchy stress of the isotropic solid is evaluated using Eq. VI.1.4:

$$\boldsymbol{\sigma}^e_{\text{matrix}} = \begin{bmatrix} 0.19 & 0 & 0 \\ 0 & 0.19 & 0 \\ 0 & 0 & 0.19 \end{bmatrix} \tag{VI.3.18}$$

and the Cauchy stress of the fibres using VI.1.17:

$$\boldsymbol{\sigma}^e_{\text{fibre},a} = \begin{bmatrix} 1692 & 0 & 0 \\ 0 & 0 & 0 \\ 0 & 0 & 0 \end{bmatrix} \qquad \boldsymbol{\sigma}^e_{\text{fibre},b} = \begin{bmatrix} 0 & 0 & 0 \\ 0 & 1692 & 0 \\ 0 & 0 & 0 \end{bmatrix} \tag{VI.3.19}$$

The fibre stress tensors indicate, as expected, that neither family of fibres is rotated. As anticipated, it is found that the fibres stretch is identical to the stretch of the cube edges: $\lambda_a = \sqrt{I_4} = 1.2$ and $\lambda_b = \sqrt{I_6} = 1.2$.

In the same manner as in the shearing example, we verify that the numerical and analytical tractions on each face (in the case $p = 0$ at all nodes) are equal:

$$\sum_{\text{nodes (0.5,Y,Z)}} \mathbf{F}^{int}_{u,\text{solid}} = \boldsymbol{\sigma}^e \cdot \mathbf{n}_X = 1692.19 \times 1.2^2\, \mathbf{n}_X = 2436.75\, \mathbf{n}_X \tag{VI.3.20}$$

$$\sum_{\text{nodes (X,0.5,Z)}} \mathbf{F}^{int}_{u,\text{solid}} = \boldsymbol{\sigma}^e \cdot \mathbf{n}_Y = 1692.19 \times 1.2^2\, \mathbf{n}_Y = 2436.75\, \mathbf{n}_Y \tag{VI.3.21}$$

$$\sum_{\text{nodes (X,Y,0.5)}} \mathbf{F}^{int}_{u,\text{solid}} = \boldsymbol{\sigma}^e \cdot \mathbf{n}_Z = 0.191 \times 1.2^2\, \mathbf{n}_Z = 0.275\, \mathbf{n}_Z \tag{VI.3.22}$$

Finally, we make sure that if $\pi_0 = 0.5$ MPa and $m = 2$:

- the total solid stress accounts for the prestress defined in Eq. VI.1.11 so that:

$$\boldsymbol{\sigma}^e_a = \begin{bmatrix} 1692.69 & 0 & 0 \\ 0 & 1692.69 & 0 \\ 0 & 0 & 0.69 \end{bmatrix} \tag{VI.3.23}$$

- the osmotic pressure is properly evaluated:

$$\Delta\pi = \frac{\pi_0}{J^m}\mathbf{I} = \frac{0.5}{(1.2^3)^2}\mathbf{I} = 0.168\mathbf{I} \tag{VI.3.24}$$

(d) Linear gradient of pressure and undeformed solid

Percolation of the fluid is imposed through the solid matrix, by imposing a linear pressure gradient along the X-axis (see Fig. VI.7) ranging from 0 to 1.5 MPa. All displacement degrees of freedom are fixed so that the solid remains undeformed. The constant permeability is set to $k = 5.10^{-3}$ mm^4 N^{-1} s^{-1}. This test enables to validate $\mathbf{F}^{int}_{p,\text{fluid}}$.

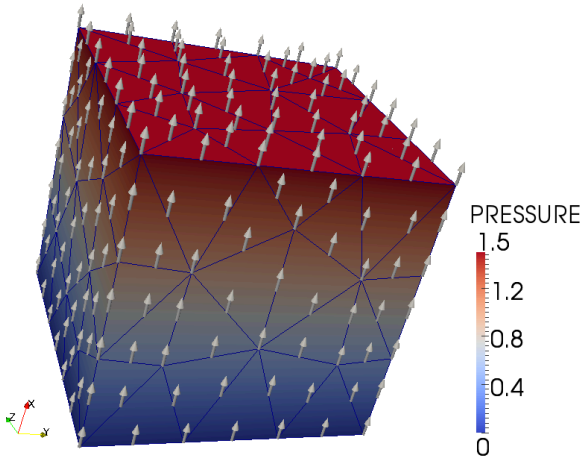

Figure VI.7: Linear pressure gradient along the X-axis, arrows representing the Darcy flow

We verify that:

- the undeformed solid is strain free ($\mathbf{F}_S = \mathbf{C}_S = \mathbf{b} = \mathbf{I}$) and, in the absence of osmotic pressure, stress free ($\boldsymbol{\sigma}^e = \mathbf{0}$)
- Darcy flux is $q_x = k \operatorname{grad} p = k \frac{\partial p}{\partial x} \approx k \frac{\Delta p}{\Delta x} = 0.0075$ mm^3/s
- as the fluid enters the cube through the bottom face and is expelled at the top:

$$\sum_{\text{nodes (-0.5,Y,Z)}} \mathbf{F}^{int}_{p,\text{fluid}} = -q_x$$
$$\sum_{\text{nodes (0.5,Y,Z)}} \mathbf{F}^{int}_{p,\text{fluid}} = q_x \qquad \text{(VI.3.25)}$$

- $\mathbf{F}^{int}_{u,\text{solid}} = \mathbf{0}$ as the solid is not stressed
- $\mathbf{F}^{int}_{p,\text{solid}} = \mathbf{0}$ as the solid is not experiencing any volumetric change
- adding the osmotic contribution has the same effects as in the shear example: solid prestress equal to the initial osmotic pressure and the osmotic pressure remains constant

VI.3.2 The Newton-Raphson solver

In the previous section, all degrees of freedom were prescribed in order to verify the correct implementation of the residuals and associated sub-routines. In this section, displacements and pressures are only imposed at the essential boundaries and the solution of the problem is determined iteratively with the Newton-Raphson solver. The same cube with fibres in the XY plane as in the previous section is used (Fig. VI.2). First, the interaction between the matrix and the fibres is investigated on two unconfined compression tests, with a loading rate of 0.01mm/s and a constant time step Δt=1s. In both cases, the permeability is set to 1×10^{30}mm^4 N^{-1} s^{-1}and free-flow boundary conditions are applied at the boundary of the cube in order to minimise the rate dependent effects. Second, the rate of convergence is examined for a third test with a low strain-dependent permeability.

In a first test, the cube is compressed in the Z-direction. The contribution of both families of fibres in resisting lateral expansion is highlighted in Fig. VI.8. Due to the symmetry of the problem, both families of fibres are equally stressed and lateral displacements are identical in X- and Y-directions. As a consequence of the fibre stress, the solid matrix experiences lateral compression.

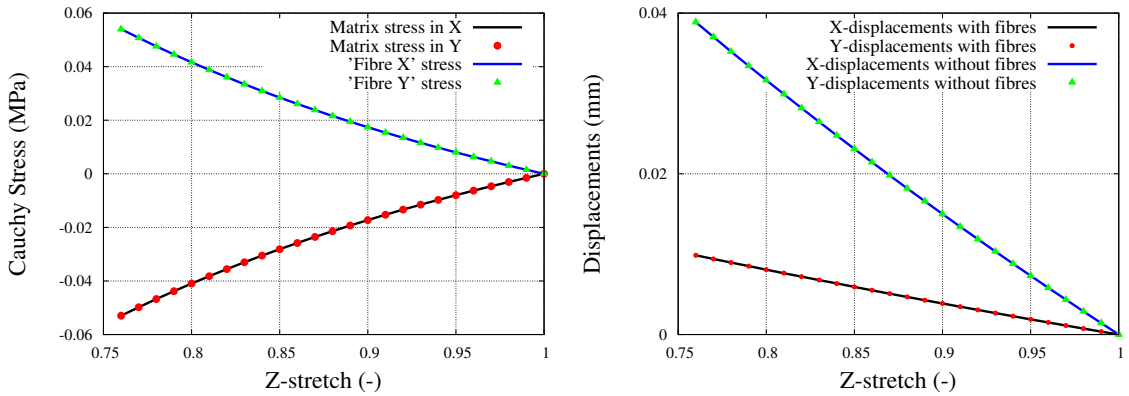

(a) Cauchy stress

(b) Point A, lateral displacements

Figure VI.8: Unconfined compression along Z-axis (fibres in X and Y directions)

In a second test (see Fig. VI.9), the cube is compressed in the X-direction. The compressive loads are solely resisted by the solid matrix along the loading direction, as the fibres are assumed to buckle under compressive strains (see condition Eq. VI.1.16). Similarly to the first test, lateral expansion induces stretches in the Y-fibres and in turn compressive stresses to the solid matrix.

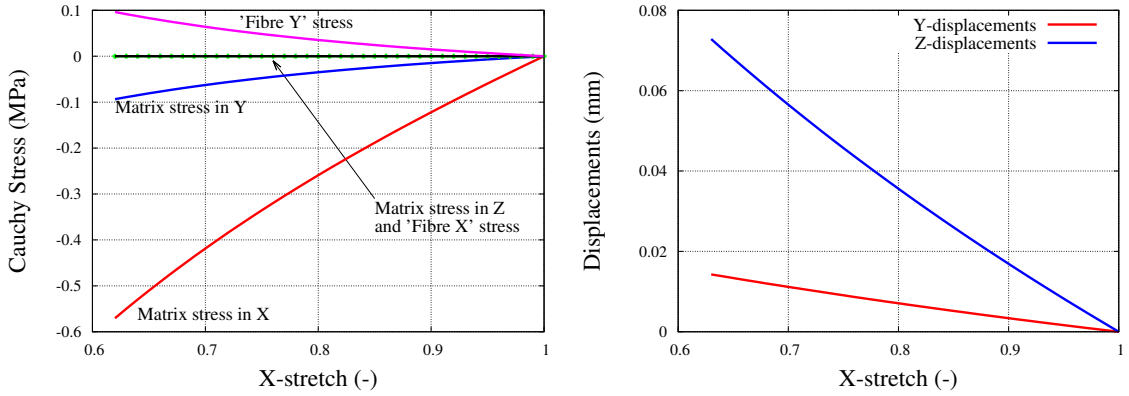

(a) Cauchy stress

(b) Point A, lateral displacements

Figure VI.9: Unconfined compression along X-axis (fibres in X and Y directions)

For illustration purposes, the rate of convergence is examined on another simple example. The same cube, with fibres in the XY-plane, is subjected to unconfined compression in the Z-direction, in a single increment of 0.02mm (i.e. 2% compression). The strain dependent permeability is defined by k_0=5×10^{-3}mm^4 N^{-1} s^{-1}and M=2, and the osmotic pressure with $\pi_0 = 0.2MPa$ and m=2. The error criteria, defined in Eq. IV.4.8 for both phases, are plotted on Fig. VI.10. In this simple example, the Newton-Raphson scheme exhibits good convergence for both phases, to 10^{-11} for the solid phase and 10^{-16} for the fluid phase, giving confidence in the implementation of the tangent operators. Note that the convergence is not quadratic as could be expected; this is a likely consequence of the fact that the tangent operator was not obtained through consistent linearisation since two terms were omitted (see Sec. IV.2).

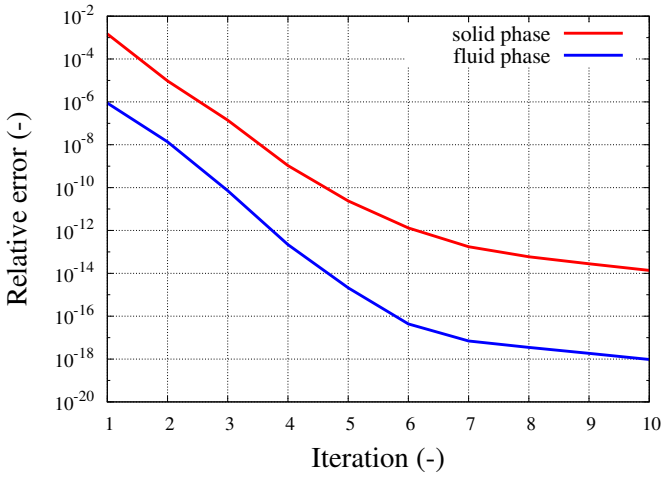

Figure VI.10: Illustration of the convergence rate

VI.4 Conclusion

In this chapter, the biphasic swelling model was specialised to the specific case of the intervertebral disc by selecting appropriate constitutive models for all constituents. It was also highlighted that the definition of the initial state of the tissue, which was already delicate in 1D, is a major challenge in the three-dimensional case. Additionally, the computing framework was described and a few high-performance computing libraries (all open source) were presented. Finally, the crucial point of the implementation of the code was tackled and a clear verification methodology proposed.

Chapter VII

The Galerkin Least-Square Stabilisation

Numerical instabilities are observed in the pressure field in regions where loads and free-draining boundary conditions are simultaneously applied. As an alternative to considerable mesh refinement, a Galerkin least-square stabilisation framework is developed in order to stabilise the solution. Results on unconfined compression tests show that this technique drastically reduces the pressure discrepancies and increases the rate of convergence. Results from confined compression tests reveal that the stabilisation, under specific circumstances, requires further refinement.

VII.1 Instabilities

Taylor-Hood tetrahedral elements (quadratic shape functions for the solid displacement, linear shape functions for the pressure) are used, aiming to fulfil the *inf-sup condition* (see Chapelle and Bathe (1993) and Brezzi and Fortin (1991)). However, numerical instabilities still manifest in the form of non-physical oscillations in the pressure field. This is illustrated on Fig. VII.1, where a laterally sealed cube is subjected to unconfined compression. The pressure is expected to monotonically increase from the top and bottom surfaces, where it is set to zero, to the highly pressurised center. Instead, spurious pressure peaks are observed near the free-flow surfaces.

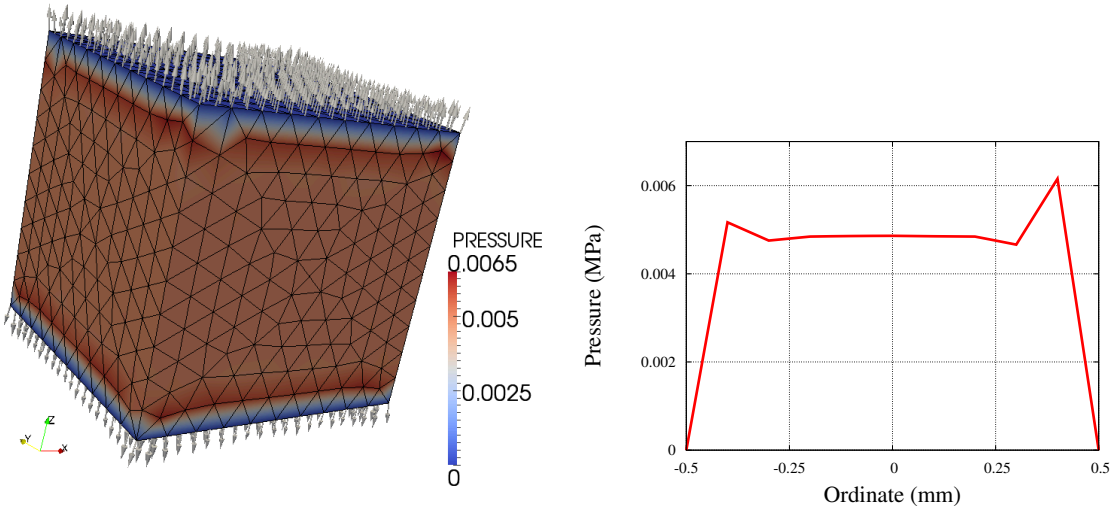

(a) Pressure contour plot - Arrows symbolise Darcy's flow

(b) Pressure along the cube's edge

Figure VII.1: Illustration of the instabilities: unconfined compression of a laterally sealed unit-length cube generate spurious pressure oscillations

This shortcoming already has been reported in the past (see for example Stokes et al. (2010) for a recent review of biological applications). Vermeer and Verruijt (1981) explain that these instabilities occur because loads applied to free-flow boundaries may lead to singularities in the derivatives of the pressure field. They also derive a lower bound critical time-step for one-dimensional problems, suggesting the requirement for large time-steps to overcome this issue, often incompatible with fast loading rates.

Several stabilisation techniques have been proposed in the context of Biot's consolidation problems for small deformations (e.g. Korsawe and Starke (2005) using least-squares mixed finite element methods, and Aguilar et al. (2008) by perturbation of the flow equation) often requiring the introduction of extra degrees of freedom and/or parameters.

The current work proposes to stabilize the pressure oscillations in the context of TPM for finite deformation problems, using a Galerkin Least-Square (GLS) formulation. It belongs to a class of stabilisation techniques developed in the 1980s (e.g. Franca and Hughes (1988); Hughes et al. (1989)), and has been used for a wide variety of problems, including Stokes flow and geotechnical problems. In this work, we follow the contribution of Truty (2001), originally formulated for consolidation analysis of fully and partially saturated soils for small strains. The derivation presented here is extended for finite deformations.

VII.2 The GLS framework

The objective of the Galerkin Least-Square formulation is to enhance the stability of the standard Galerkin scheme by adding a stabilisation term to the residual R that was derived in Chapter IV and is recalled here:

$$R = R_u - \Delta t R_p = 0 \tag{VII.2.1}$$

where R_u and R_p are respectively the residuals of the balance of linear momentum and of the balance of mass. The above variational form is then enriched by a stabilisation term R_{GLS} as follows:

$$R = R_u - \Delta t R_p + R_{GLS} = 0 \tag{VII.2.2}$$

The stabilisation term is physically motivated, as it is derived from the strong form of the fluid flow continuity equation (Eq. III.3.8). It takes the form:

$$R_{GLS} = \int_v \left[\mathrm{div}\left(\dot{\mathbf{f}} + k\nabla g\right)\right]^{\mathrm{T}} \tau^* \left[\mathrm{div}\left(\mathbf{v}^S + k\nabla p\right)\right] \, dv \tag{VII.2.3}$$

The presence of a stabilisation factor τ^*, which will subsequently be defined, is necessary to ensure unit consistency and is expressed in $\mathrm{N.s^2.m^{-2}}$. Eq. VII.2.3 is then discretised using notations defined in Chapter IV and taking into account the fact that linear pressure elements are used (i.e. $\mathrm{div}(\nabla \mathbf{N}^p) = 0$):

$$R_{GLS} = \int_v \left\{\nabla \mathbf{N}^u \dot{\mathbf{f}}^e - \nabla k \nabla \mathbf{N}^p g^e\right\}^{\mathrm{T}} \tau^* \left\{\nabla \mathbf{N}^u \dot{\mathbf{u}}^e - \nabla k \nabla \mathbf{N}^p p^e\right\} \, dv \tag{VII.2.4}$$

Introducing the time integration scheme ($\dot{\mathbf{u}}^e = \Delta \mathbf{u}^e / \Delta t$, where $\Delta \mathbf{u}^e$ is the incremental displacement) and defining $\tau^{GLS} = \tau^* / \left(\Delta t\right)^2$, leads to:

$$R_{GLS} = \int_v \left\{\nabla \mathbf{N}^u \mathbf{f}^e - \Delta t \nabla k \nabla \mathbf{N}^p g^e\right\}^{\mathrm{T}} \tau^{GLS} \left\{\nabla \mathbf{N}^u \mathbf{u}^e - \Delta t \nabla k \nabla \mathbf{N}^p p^e\right\} \, dv \tag{VII.2.5}$$

Using the same notations and assumptions as in Chapter IV, the above R_{GLS} is linearised, which results in the following system in the matrix form:

$$\begin{bmatrix} \mathbf{K}_{uu} + \mathbf{K}_{uu}^{GLS} & \mathbf{K}_{up} + \mathbf{K}_{up}^{GLS} \\ \mathbf{K}_{up}^{\mathrm{T}} + \mathbf{K}_{pu}^{GLS} & \Delta t\, \mathbf{K}_{pp} + \mathbf{K}_{pp}^{GLS} \end{bmatrix} \begin{Bmatrix} \delta \mathbf{u} \\ \delta \mathbf{p} \end{Bmatrix} = \begin{Bmatrix} \mathbf{F}_u^{ext} \\ \Delta t\, \mathbf{F}_p^{ext} \end{Bmatrix} - \begin{Bmatrix} \mathbf{F}_u^{int} + \mathbf{F}_{u,GLS}^{int} \\ \Delta t \mathbf{F}_p^{int} + \mathbf{F}_{p,GLS}^{int} \end{Bmatrix} \tag{VII.2.6}$$

where:

$$\mathbf{K}_{uu}^{GLS} = \int_v \{\nabla \mathbf{N}^u\}^{\mathrm{T}} \tau^{GLS} \nabla \mathbf{N}^u \, dv \tag{VII.2.7a}$$

$$\mathbf{K}_{up}^{GLS} = \int_v \{\nabla \mathbf{N}^u\}^{\mathrm{T}} \tau^{GLS} \left(-\Delta t \nabla \hat{k} \nabla \mathbf{N}^p\right) \, dv \tag{VII.2.7b}$$

$$\mathbf{K}_{pu}^{GLS} = \left(\mathbf{K}_{up}^{GLS}\right)^{\mathrm{T}} \tag{VII.2.7c}$$

$$\mathbf{K}_{pp}^{GLS} = \int_v \left\{\Delta t \nabla \hat{k} \nabla \mathbf{N}^p\right\}^{\mathrm{T}} \tau^{GLS} \left(\Delta t \nabla \hat{k} \nabla \mathbf{N}^p\right) \, dv \tag{VII.2.7d}$$

$$\mathbf{F}_{u,GLS}^{int} = \int_v \{\nabla \mathbf{N}^u\}^{\mathrm{T}} \tau^{GLS} \left(\nabla \mathbf{N}^u \Delta \hat{\mathbf{u}}^e - \Delta t \nabla \hat{k} \nabla \mathbf{N}^p \hat{\mathbf{p}}^e\right) \, dv \tag{VII.2.7e}$$

$$\mathbf{F}_{p,GLS}^{int} = \int_v \left\{\Delta t \nabla \mathbf{N}^p \nabla \hat{k}\right\}^{\mathrm{T}} \tau^{GLS} \left(\nabla \mathbf{N}^u \Delta \hat{\mathbf{u}}^e - \Delta t \nabla \hat{k} \nabla \mathbf{N}^p \hat{\mathbf{p}}^e\right) \, dv \tag{VII.2.7f}$$

In Truty (2002), it is observed that the most influential terms of the stabilisation are $\mathbf{K}_{uu}^{GLS}$ and its counterpart $\mathbf{F}_{u,GLS}^{int}$. As an initial simplification, these two terms only are implemented in the present formulation in order to test their performance. This is achieved by considering that, for the GLS terms only, the permeability is not strain dependent. This dependence has only slight effects at the early stage of the consolidation problem, when the instabilities arise. Eq. VII.2.6 then reduces to:

$$\begin{bmatrix} \mathbf{K}_{uu} + \mathbf{K}_{uu}^{GLS} & \mathbf{K}_{up} \\ \mathbf{K}_{up}^{\mathrm{T}} & \Delta t \, \mathbf{K}_{pp} \end{bmatrix} \begin{Bmatrix} \delta \mathbf{u} \\ \delta \mathbf{p} \end{Bmatrix} = \begin{Bmatrix} \mathbf{F}_u^{ext} \\ \Delta t \, \mathbf{F}_p^{ext} \end{Bmatrix} - \begin{Bmatrix} \mathbf{F}_u^{int} + \mathbf{F}_{u,GLS}^{int} \\ \Delta t \mathbf{F}_p^{int} \end{Bmatrix} \tag{VII.2.8}$$

Finally, the stabilisation factor is defined based on Truty (2001):

$$\tau^{GLS} = \frac{h^2}{4 k_0 \Delta t} \tag{VII.2.9}$$

In Truty (2001), the parameter h is a length characterizing the element's size in the direction of the fluid flow. In the current application, it was simply taken as the radius of the element's circumsphere. As illustrated in the following section, this definition of τ^{GLS} stems from the fact that the solution needs greater stabilisation as the mesh gets coarser and as either or both the permeability and the size of the time-step decrease. In this work, due to the soft nature of the solid phase, it was not necessary to include a measure of material stiffness in the definition of τ^{GLS}, although this may be necessary for stiffer materials (e.g. Truty (2001) and Aguilar et al. (2008)).

It can be noted that the numerical integration is performed using a 4-point Gauss

quadrature. The accuracy was verified with tests using up to 27 points. Reduced integration was also considered for the GLS terms, with no beneficial outcome.

VII.3 Numerical examples

Two numerical examples are considered in order to test the performances of the stabilisation scheme. First, the robustness of the Galerkin Least-Square framework is investigated under unconfined conditions. The influence of the loading rate, mesh size, permeability and strain level are examined. Second, limitations of this technique are presented on the extreme case of confined compression, where it will be seen that the benefits of the stabilisation vanish. Note that in this section, conversely to the previous chapter, the term convergence is to be interpreted as the convergence to the "continuum solution" that would result from an infinitely fine mesh. In the confined compression case, results from the 1D model solved with 50 elements are used to represent this idealised solution.

VII.3.1 Unconfined compression of an isotropic cylinder

The performance of the GLS stabilisation technique is first assessed on a biphasic isotropic cylinder subjected to unconfined compression. With a 18mm radius, a thickness of 8mm and a solid phase defined with $\lambda = 0.2$ MPa and $\mu = 0.5$ MPa, the cylinder can be thought of as an idealised human nucleus pulposus of the intervertebral disc when the permeability is set to $k = 1{\times}10^{-3}\text{mm}^4\text{N}^{-1}\text{s}^{-1}$.

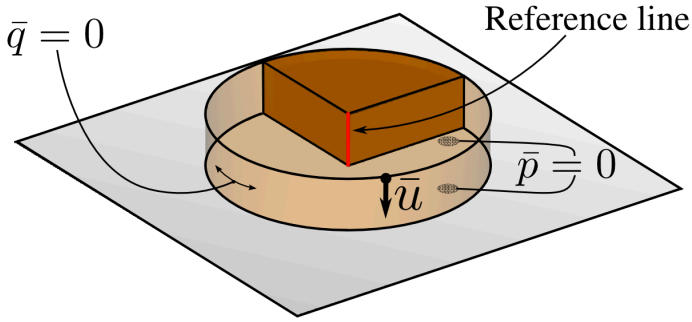

Figure VII.2: Loading and boundary conditions

The fluid flux $\bar{\mathbf{q}}$ at the boundary is prescribed to zero on the vertical faces offering a lateral seal to the cylinder. The pressure $\bar{p}$ is set to zero on the top and bottom surfaces (see Fig. VII.2). These boundary conditions define the top and bottom

surfaces as the only free-flow boundaries. This results in a near to uni-axial fluid flow through the depth of the cylinder.

In what is herein referred to as the "reference loading", the top surface is displaced downwards at a rate of 2.5μm.s^{-1} with time increments $\Delta t = 6.4$s, until the height of the cylinder reduces by 1%. Such loading rates, together with permeabilities lower than 1 mm^4 N^{-1} s^{-1}, guarantee that the steady state is not reached instantly. In order to reduce the size of the problem, symmetry boundary conditions are applied onto a quarter cylinder. Analyses are undertaken on different meshes, the main characteristics of which are shown in Fig. VII.3.

All results are plotted against nodal values gathered on the "reference line" defined in Fig. VII.2 and VII.3.

	Nodes	Elements	Elements on ref line
mesh 1	8083	5261	5
mesh 2	16507	11087	7
mesh 3	38424	26622	9
mesh 4	78033	55190	12

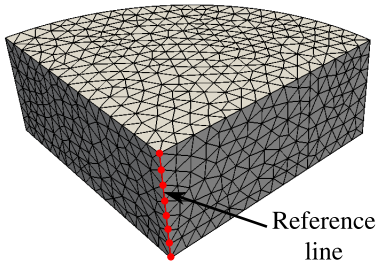

Figure VII.3: Meshes characteristics (left) and mesh 2 (right)

The low permeability hinders the fluid's ability to flow, defining two distinct regions associated with the load transfer mechanism. The first region, located near the free-flow boundaries, is dominated by solid deformation: the fluid does not have the ability to pressurize as it is squeezed out of the cylinder. This results in a lower fluid content in this region, explaining the peak strains observed near the top and bottom surfaces (see Fig. VII.4a). The second region, situated at the centre of the cylinder, is predominantly subjected to fluid pressurization (see Fig. VII.4b) due to the fact that the low permeability is confining the fluid at the centre of the cylinder.

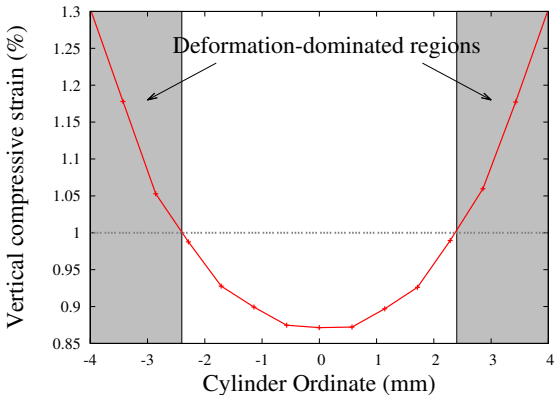

(a) Nodal strains

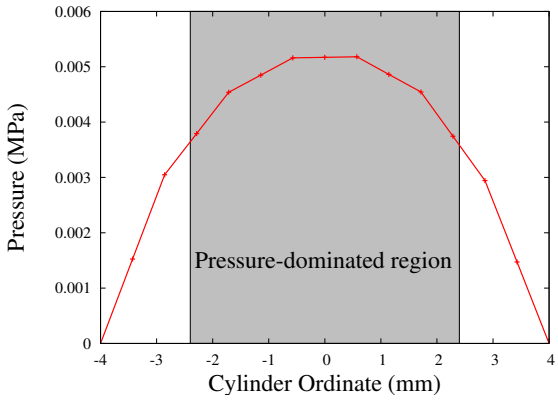

(b) Nodal pressures

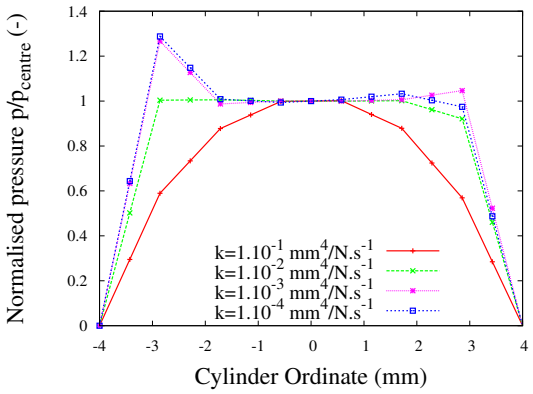

(c) Influence of permeability

Figure VII.4: Mesh 2: deformation mechanisms for $k = 0.1$ mm^{4}N^{-1}s^{-1} (left and centre) and influence of permeability (right)

As the permeability decreases, the boundary between solid- and pressure-dominated regions shifts towards the top and bottom surfaces (see Fig. VII.4c) and the level of pressurization rises. For a given mesh, when the permeability falls under a certain value ($k < 1\times10^{-1}$ mm^{4}N^{-1}s^{-1} for mesh 2 in this example), the pressure profile starts to exhibit spurious oscillations near the free-flow boundaries (over 10% discrepancies for mesh 1 and mesh 2 when $k = 5\times10^{-2}$ mm^{4}N^{-1}s^{-1}, and over 8% for all meshes when $k = 1\times10^{-2}$ mm^{4}N^{-1}s^{-1}). Furthermore, the quality of the solution can be affected through the entire mesh as the near boundary oscillation propagates toward the centre for coarse meshes (e.g. mesh 1 in Fig. VII.5c). Finally, it was verified (in line with Vermeer and Verruijt (1981)) that decreasing the time-step exaggerates the pressure oscillations, although not presented here.

Mesh refinement is the most natural and straightforward choice to overcome this issue, in particular when interested in accurately capturing the steep pressure gradients. As Fig. VII.5a and VII.5b illustrate, the non-physical pressure peaks can be removed

by using meshes denser than that characterised by mesh 2. However, this is only a valid solution in some cases. Fig. VII.5c illustrates that, for low permeability, the spurious oscillations cannot always be reduced by reasonably-sized denser meshes, but also that the rate of convergence can be affected (see mesh 1).

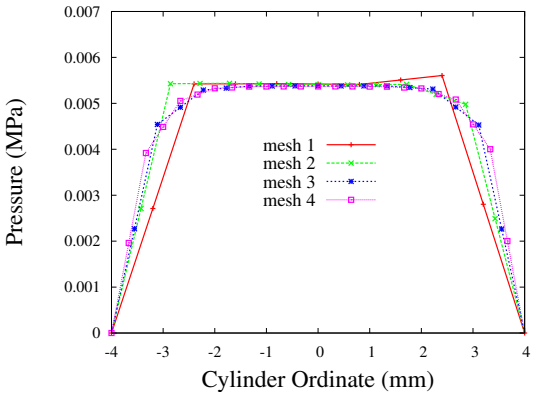

(a) $k = 1{\times}10^{-2}$ mm^{4}N^{-1}s^{-1}

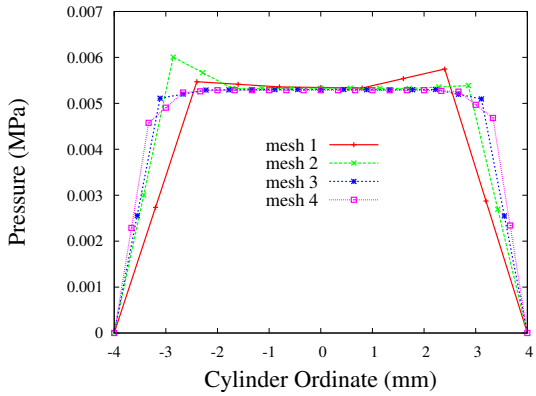

(b) $k = 5{\times}10^{-3}$ mm^{4}N^{-1}s^{-1}

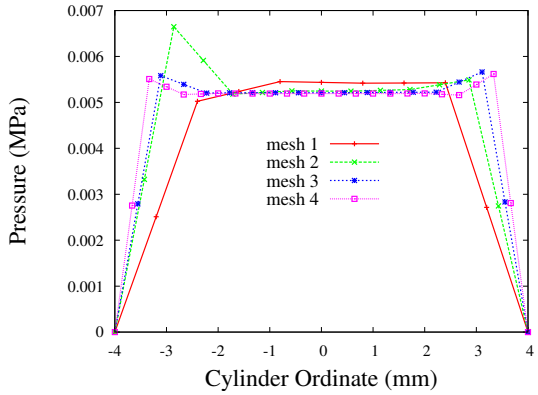

(c) $k = 1{\times}10^{-3}$ mm^{4}N^{-1}s^{-1}

Figure VII.5: Effects of mesh refinement on standard Galerkin method

The GLS stabilisation offers substantial improvements to the solution. Fig. VII.6 shows the benefits for four different meshes when $k = 5{\times}10^{-3}$ mm^{4}N^{-1}s^{-1} and $k = 1{\times}10^{-3}$ mm^{4}N^{-1}s^{-1}. The primary enhancement is that all spurious oscillations observed in Fig. VII.5 have been stabilised, with the exception of mesh 2 where, when $k = 1{\times}10^{-3}$ mm^{4}N^{-1}s^{-1}, the discrepancies decreased from 27% to 6%. Additionally, when accurate resolution of the near-boundary pressure gradient, defined as the transition between the deformation- and pressure-driven regions, is not sought, the GLS formulation allows for coarser meshes to be used, since it also prevents the oscillations from propagating towards the centre. For example, when $k = 1{\times}10^{-3}$ mm^{4}N^{-1}s^{-1}, mesh 1 (8000 nodes) with GLS offers similar performances to mesh 3

(38000) without the stabilisation (compare Fig. VII.5c and VII.6b). Finally, it is important to notice that the GLS stabilisation is only having a damping effect on the spurious oscillations, while leaving stable solutions unaffected (compare Fig. VII.5b and VII.6a at the centre).

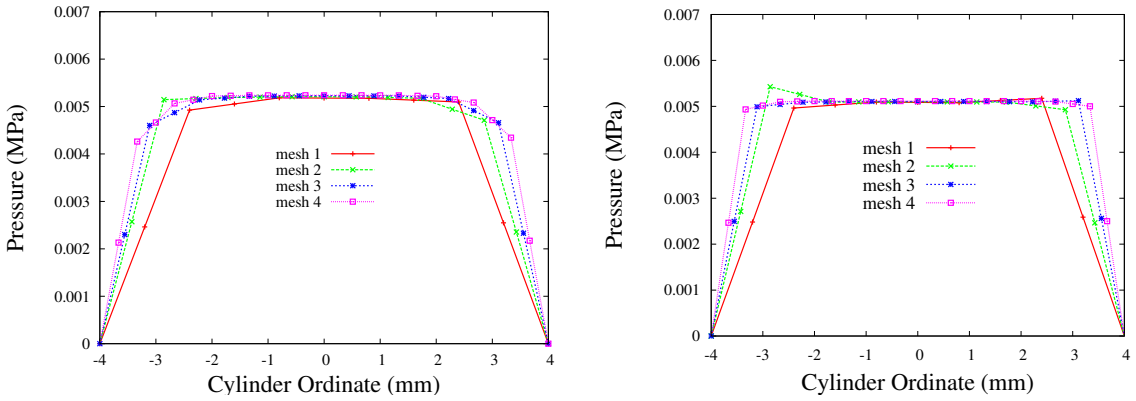

(a) $k = 5{\times}10^{-3}$ mm^{4}N^{-1}s^{-1} (b) $k = 1{\times}10^{-3}$ mm^{4}N^{-1}s^{-1}

Figure VII.6: Effects of mesh refinement on GLS stabilisation

A few observations can be made to support the choice of the stabilisation factor τ^{GLS} in (Eq. VII.2.9). First, Fig. VII.6 highlights the fact that the stabilisation performs equally well irrespective of the change of mesh and permeability, giving confidence in the way the element's characteristic size and permeability are accounted for. The impact of the time-step on the stabilisation was also investigated: it was verified that if τ^{GLS} is not inversely proportional to Δt, stabilisation is not possible. Also, in simulations not presented here, it was confirmed that the size of the time-step ($\Delta t = \{0.64\text{s}, 3.2\text{s}, 6.4\text{s}, 8\text{s}, 32\text{s}\}$) does not affect the quality of the stabilised solution. Finally, it was also verified (again not shown here) that changing the loading rate ($1.25\mu\text{m.s}^{-1}$, $2.5\mu\text{m.s}^{-1}$, $6.25\mu\text{m.s}^{-1}$) did not affect the degree of peak pressure oscillations for the stabilised results.

Performance of the GLS stabilisation was initially assessed for greater levels of deformation. As Fig. VII.7 shows, discrepancies in pressure reduce as the compressive strain increases, which is in line with the findings in Truty (2001) and Aguilar et al. (2008), where oscillations are reported to occur at the "early stage" of the consolidation problem. Although the GLS stabilisation also performs well at higher strains (see Fig. VII.7b), this observation motivated the choice to present results at 1% compression throughout this numerical example.

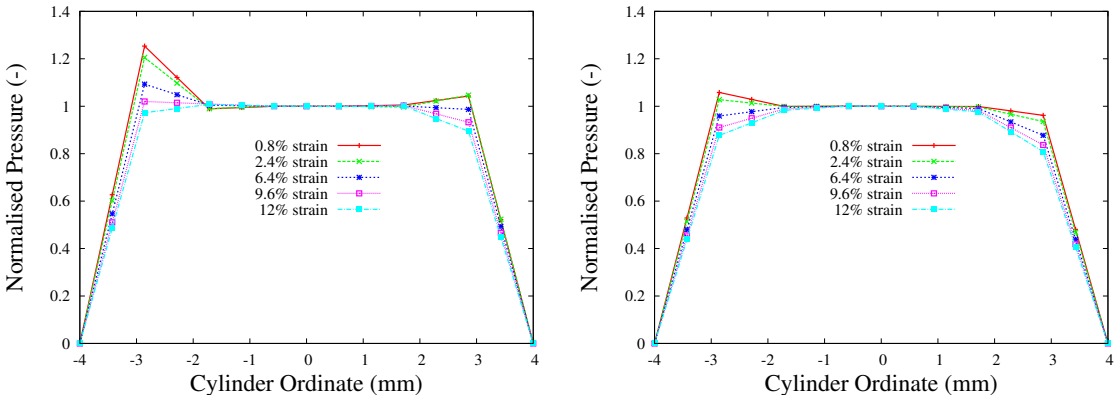

(a) Standard Galerkin (b) GLS

Figure VII.7: Effects of higher strain on stability for mesh 2

A sensitivity study was performed to characterise the parameter h in (Eq. VII.2.9). Several combinations of the radius of the circumsphere, the shortest and longest edges of the tetrahedron were tested without noticeable and consistent improvement to the overall solution.

VII.3.2 Limitations on a confined compression test

Although derived from physical considerations (i.e. the continuity equation), the introduction of a non-physical parameter τ^{GLS} is required in order to combine the GLS framework with the current formulation in a consistent manner (i.e to comply, from a unit perspective, with other quantities). It is precisely from this lack of physical justification that difficulties to derive a universal stabilisation factor arise. Although τ^{GLS} contains information about the mesh size, the permeability and the size of the time-step, it is not equipped to adapt to, for example, various boundary conditions or stiffnesses of the solid phase. The potential outcome of this shortcoming will be therein illustrated on the more extreme case of confined compression with strain-dependent permeability.

A 2mm thick sample of diameter 6mm is numerically tested, using the apparatus presented for the 1D model in Sec. V.4 and described in Fig. VII.8. Symmetries are accounted for by only modeling an eighth of the sample (i.e. a quarter of the section and half of the thickness). This way, all elements through the depth are mobilised to capture the pressure gradient near the top surface (as opposed to both surfaces in the previous section). Free-flow boundary conditions are applied to the top surface only, which is displaced vertically at a rate of 1μm.s^{-1}, until 5% compression is achieved.

This ramp phase is followed by a hold phase where the sample is held in position until steady state is reached. Confinement is modelled by lateral constraints.

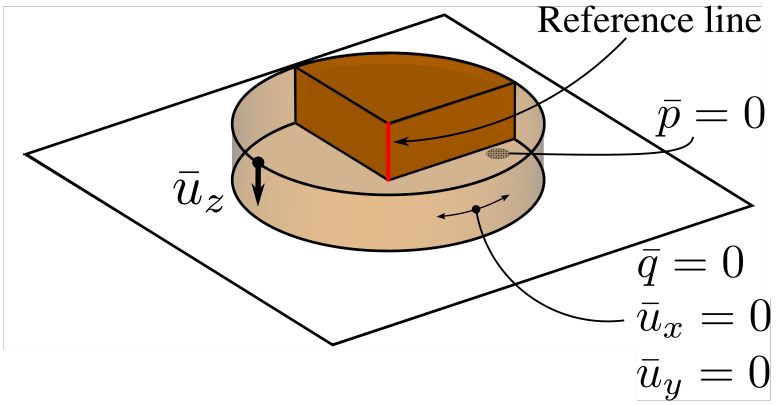

Figure VII.8: Loading and boundary conditions for the confined compression test

The material parameters of the solid phase are λ=0.5MPa and μ=0.1MPa. The initial permeability is set to k_0=1×10^{-3} mm^4 N^{-1} s^{-1}, while the parameter M controlling the strain dependency is equal to 1. Due to compression levels in excess of the applied 5% anticipated in the region below the top surface, the permeability is expected to substantially decrease:

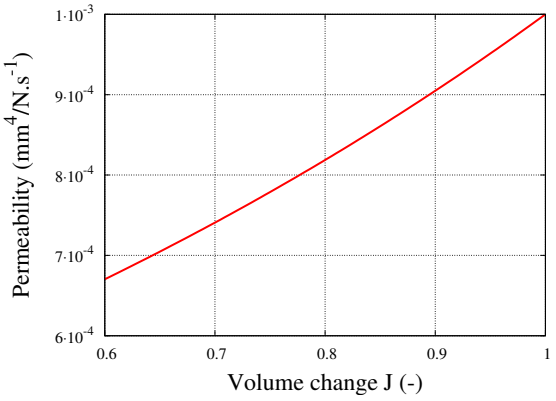

Figure VII.9: Permeability as a function of the volume change

For comparison purposes, simulations with identical parameters are performed with the 1D model. Naturally, the Neo-Hookean model defined in Sec. VI.1.1 was implemented in 1D as well. The convergence study is performed using the five meshes depicted in Fig. VII.10. Additional mesh characteristics are presented in Table VII.1.

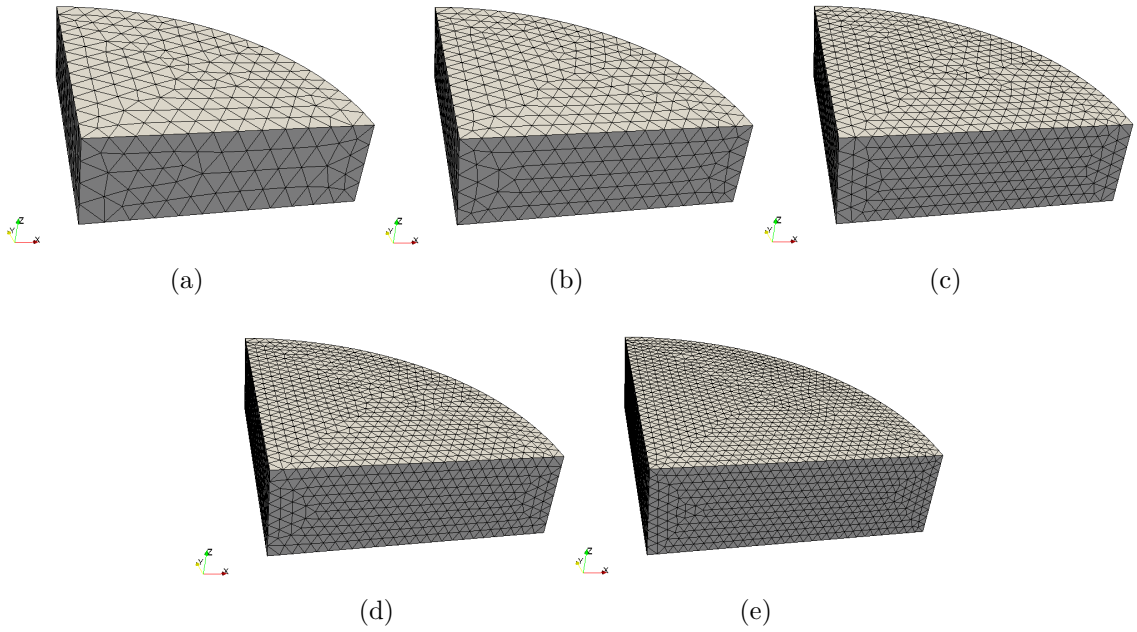

(a) (b) (c)

(d) (e)

Figure VII.10: The 5 meshes used for the confined compression test

	Nodes	Elements	Size (mm)	Elements on ref line
Mesh0	6333	4050	0.25	4
Mesh1	11982	7851	0.20	5
Mesh2	25112	17233	0.15	7
Mesh3	47494	32663	0.12	8
Mesh4	78544	54624	0.10	10

Table VII.1: Mesh characteristics - Size is an average of the elements' edge length

Fig. VII.11a and VII.11b show that the evolution of the reaction force, with and without stabilisation, is generally in good agreement with the 1D model. However, a closer look at the first few increments reveals a kink in the stabilised response (see Fig. VII.11c). Similarly, at the beginning of the hold phase the stabilised solution exhibits a sudden drop (see Fig. VII.11d). Although the rate of convergence of the stabilised solution is faster than the non-stabilised one, the latter shows superior quality when equivalent meshes are compared.

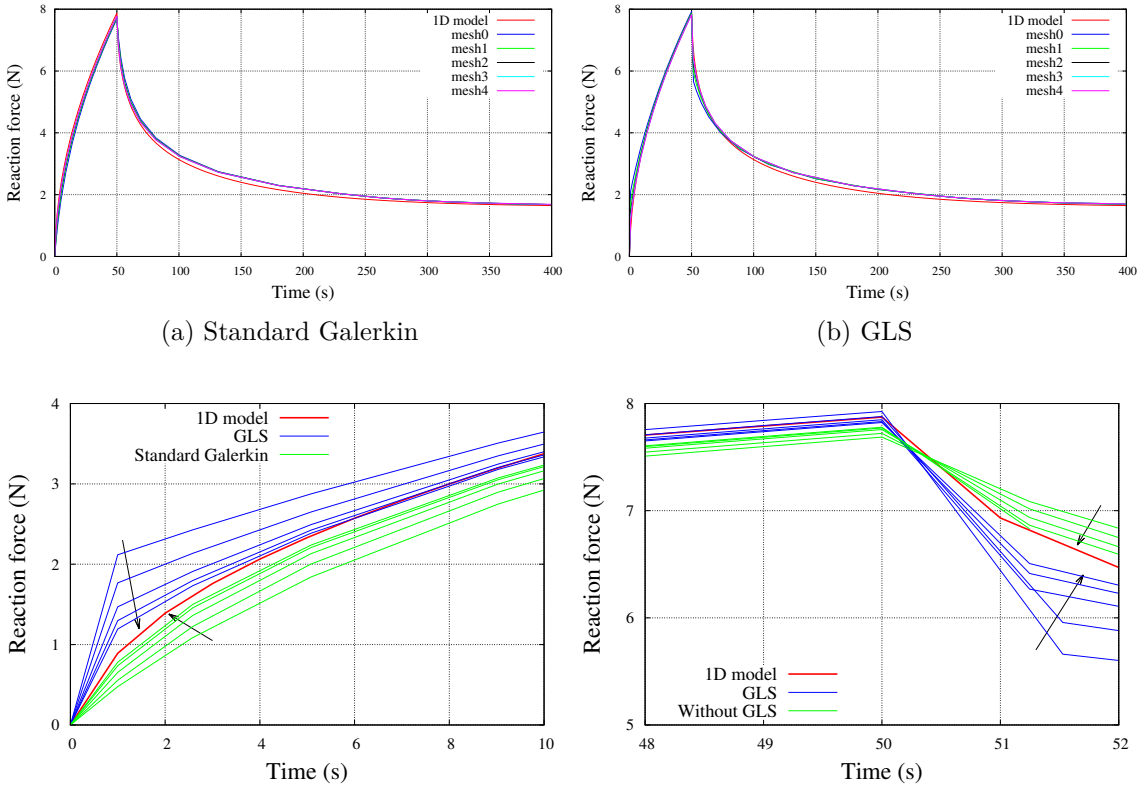

(a) Standard Galerkin

(b) GLS

(c) Beginning of the simulation

(d) End of the ramp

Figure VII.11: Reaction force - Arrows indicate mesh refinement

In order to understand the origin of these discontinuities, which are not physically motivated, pressure and stress states are investigated at the end of the first increment (i.e. t=1s) and at the end of the first increment of the hold phase (i.e. t=51s).

The non-stabilised solution exhibits a behaviour similar to the one reported in the previous section. Oscillations are observed in the pressure and stress responses at the early stage of the analysis (see Fig. VII.12a and VII.13a). These, although it is not shown here, completely disappear after a few increments (e.g. t≈15s for mesh0). Upon mesh refinement, the pressure at the centre of the sample (ordinate z=-0.5 on Fig. VII.12a) and the stress near the top surface (z=0.5 on Fig. VII.13a) converge to the solution of the 1D model, while oscillations are damped.

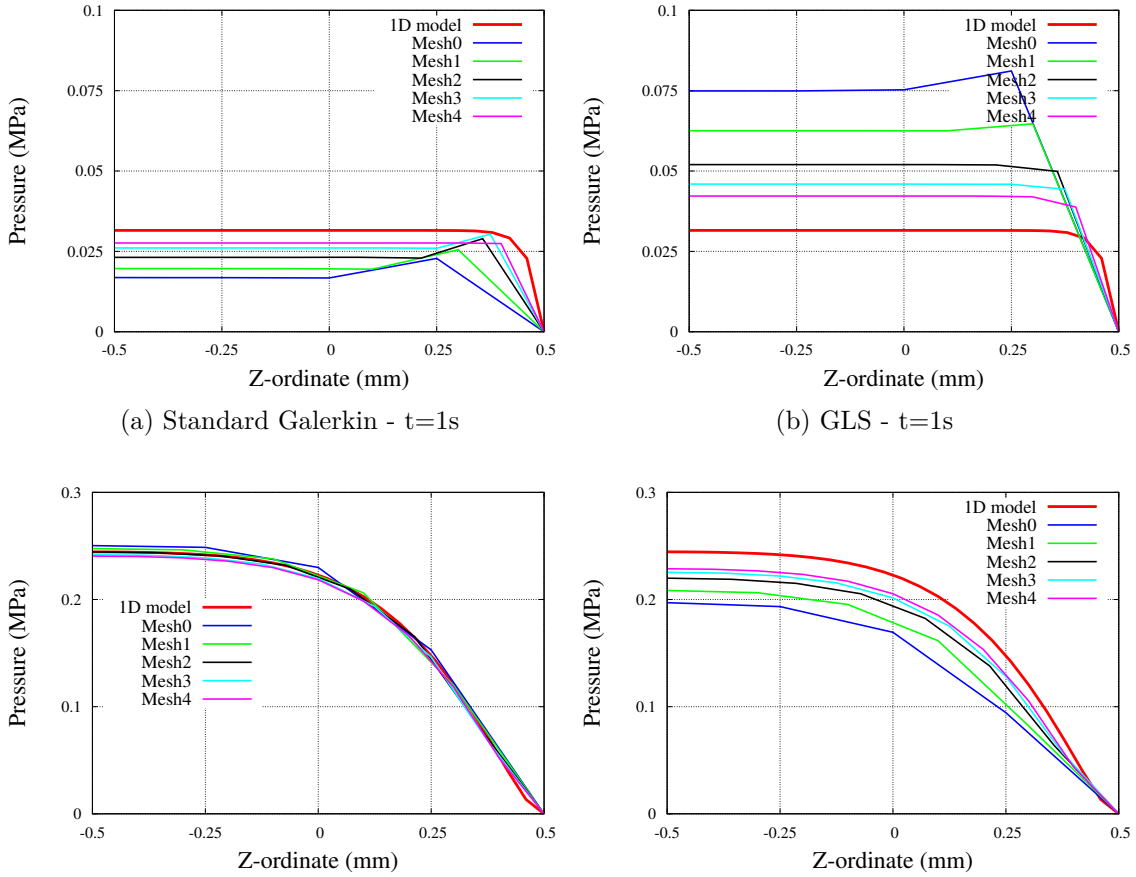

(a) Standard Galerkin - t=1s

(b) GLS - t=1s

(c) Standard Galerkin - t=51s

(d) GLS - t=51s

Figure VII.12: Pressure distribution across the sample at the end of the first increment (a) and (b) and at the end of the ramp (c) and (d)

However, the benefits resulting from the GLS stabilisation on the unconfined compression test are not reproduced in the unconfined compression case. The damping of the spurious oscillations clearly comes at the expense of the quality of the solution. Fig. VII.12(a) and (b) for pressure, and Fig. VII.13a and b for Cauchy stress show that the difference with the 1D model is 1.5 to 3 times higher with GLS than with the standard Galerkin formulation. The fact that the pressure field is highly overestimated at the centre of the sample is not sufficiently compensated by a considerably faster rate of convergence (this is better observed on Fig. VII.14). Furthermore, the GLS formulation introduces discrepancies at the beginning of the hold phase (see Fig. VII.12d and Fig. VII.13d), whereas the coarse mesh gives accurate results without stabilisation.

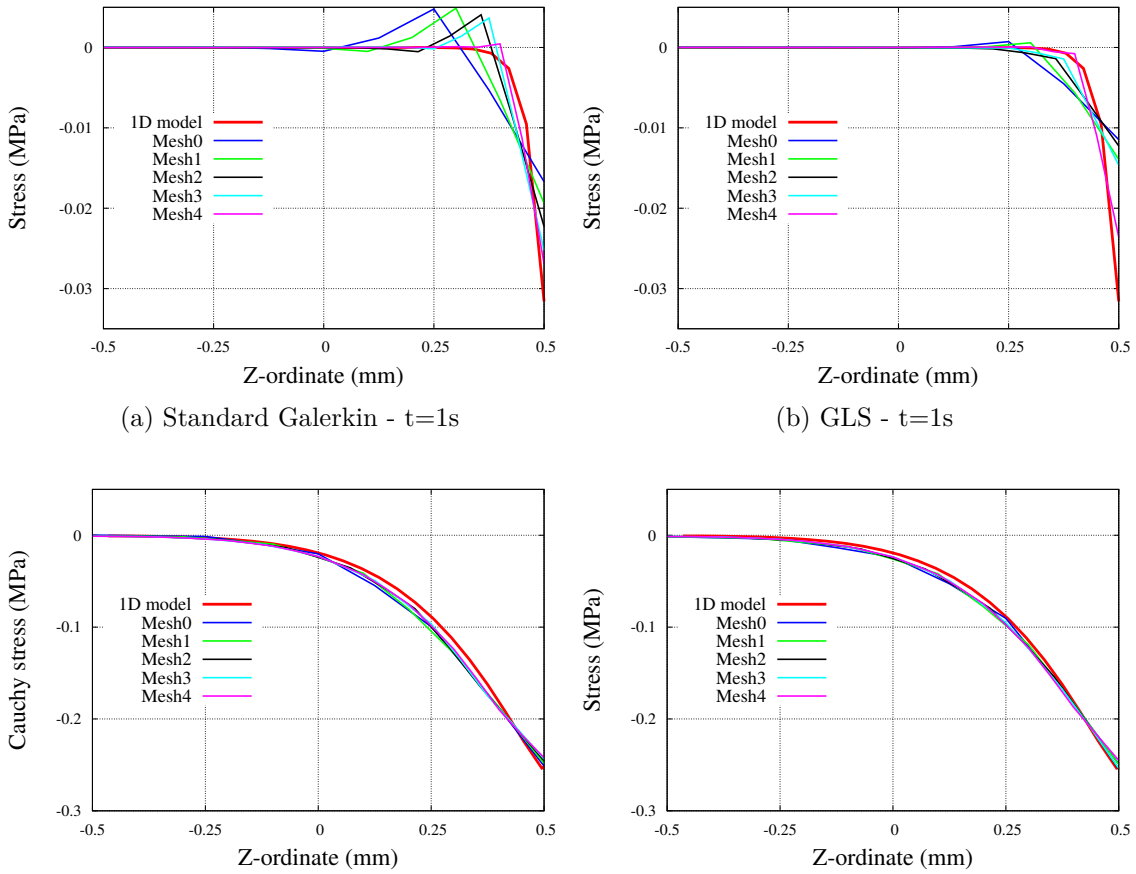

(a) Standard Galerkin - t=1s

(b) GLS - t=1s

(c) Standard Galerkin - t=51s

(d) GLS - t=51s

Figure VII.13: Cauchy stress distribution across the sample

It is important to note that conversely to the pressure field which is a primary variable evaluated at the nodes, the Cauchy stress is post-processed by extrapolation of stress from the Gauss points. This probably contributes to the disparities observed near the top surface on Fig. VII.13(a) and (b), where gradients are not accurately captured.

Fig. VII.14 summarises the above findings in a compact manner. The deterioration of the quality of the solution, both at the beginning of the ramp and the hold phase, is highlighted, together with a faster convergence rate when GLS is considered.

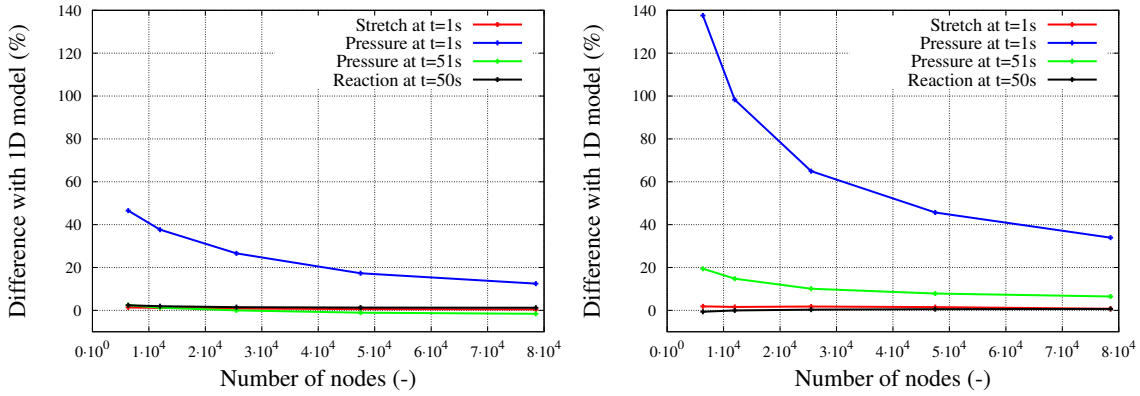

(a) Standard Galerkin (b) GLS

Figure VII.14: Comparison of the 3D results with the 1D for various meshes

Briefly, in order to demonstrate that the permeability strain-dependency is not the sole reason accounting for the aforementioned shortcomings, the same test is repeated considering constant permeability (i.e. keeping k_0=1×10^{-3} mm^4 N^{-1} s^{-1}and setting M=1). Fig. VII.15 shows that the jump in the reaction force at the early stage of the simulation and the highly overestimated pressure are deficiencies still manifesting without the strain-dependency of the permeability.

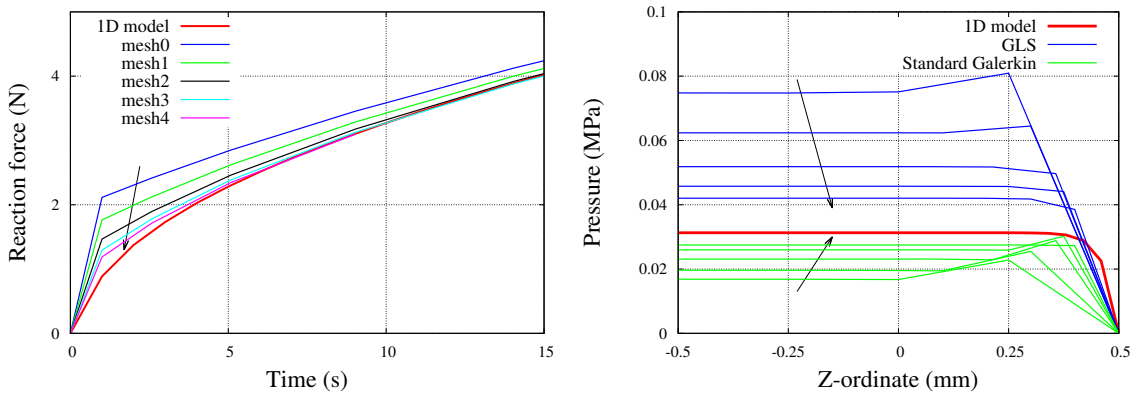

(a) Reaction - GLS (b) Pressure with and without GLS

Figure VII.15: Results with constant permeability - The arrows indicate mesh refinement

The observations made in this section, together with the results of the previous section, suggest that the GLS framework has the potential to stabilise the spurious oscillations manifesting in the pressure field, but that the currently defined stabilisation factor $\tau^{GLS} = h^2/4k_0\Delta t$ is not adequate under all circumstances. An inspection of the internal force vector relative to the displacement degrees of freedom

$$\mathbf{F}_u^{int} = \int_v \{\nabla \mathbf{N}^u\}^{\mathrm{T}} \left(\hat{\boldsymbol{\sigma}}^e - \mathbf{N}^p \hat{\mathbf{p}}^e + \tau^{GLS} \nabla \mathbf{N}^u \Delta \hat{\mathbf{u}}^e\right) dv \tag{VII.3.1}$$

suggests that an overestimated stabilisation factor may result in overly-compensated pressure and/or Cauchy stresses. In order to support this idea, simulations are run once again with reduced stabilisation factors: τ^{GLS}, 0.75 τ^{GLS}, 0.5 τ^{GLS} and 0.25 τ^{GLS}.

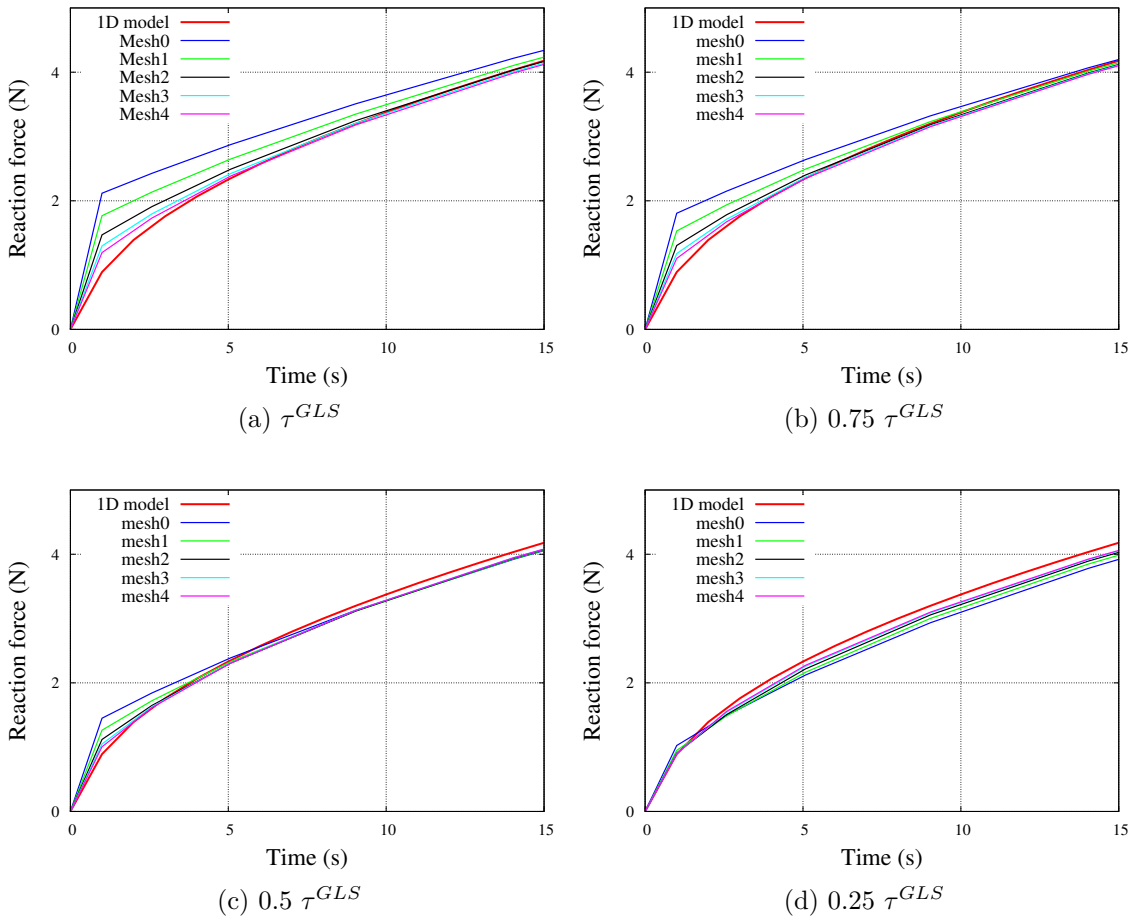

(a) τ^{GLS} (b) 0.75 τ^{GLS}

(c) 0.5 τ^{GLS} (d) 0.25 τ^{GLS}

Figure VII.16: The reaction force at the early stage of the simulation for various stabilisation factors

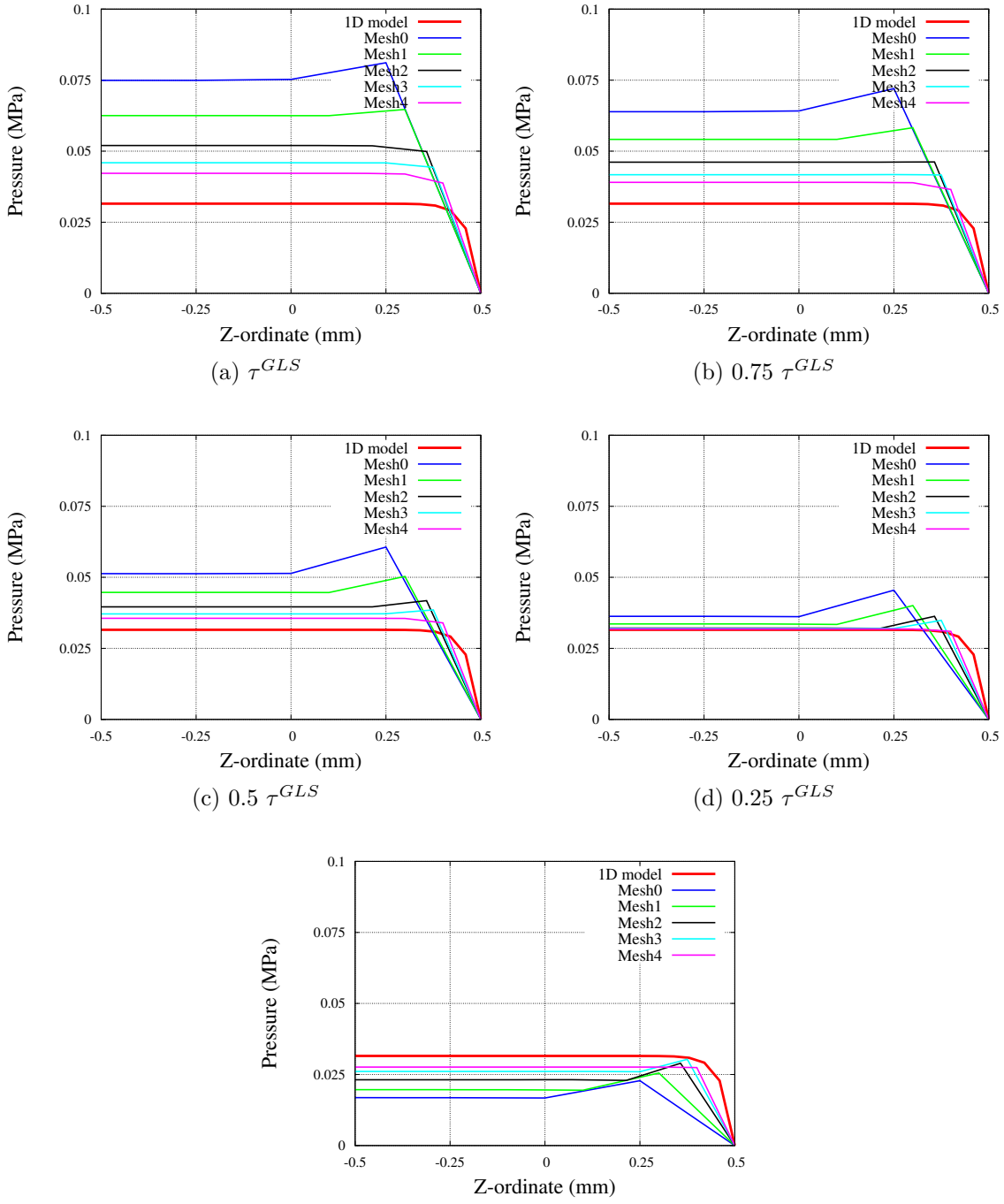

(a) τ^{GLS}

(b) 0.75 τ^{GLS}

(c) 0.5 τ^{GLS}

(d) 0.25 τ^{GLS}

(e) Standard Galerkin

Figure VII.17: The pressure distribution across the sample at t=1s for various stabilisation factors

Results, presented on Fig. VII.16 and VII.17, indicate that, as the stabilisation factor is decreased, the stabilised solution converges toward the un-stabilised one. It is, for example, interesting to notice that for 0.25 τ^{GLS}, the pressure quickly converges to the same solution as the 1D model (see Fig. VII.17d). Since both solutions offer

an upper and lower bond estimate to both the pressure and the reaction force, this suggests the existence of a stabilisation factor optimised for this analysis.

Undoubtedly, the definition of a better suited stabilisation factor cannot simply result from reducing the currently defined one, as it would under-stabilise the solution of the unconfined test. As suggested in Truty (2002), improvements could stem from the derivation of the mesh size parameter h that contains information about the direction of the fluid flow or the addition of a term that reflects the stiffness of the solid phase. At this stage, it is recommended to locally refine meshes in regions where $\mathbf{F}^{int}_{u,GLS}$ is predominant (Fig. VII.18).

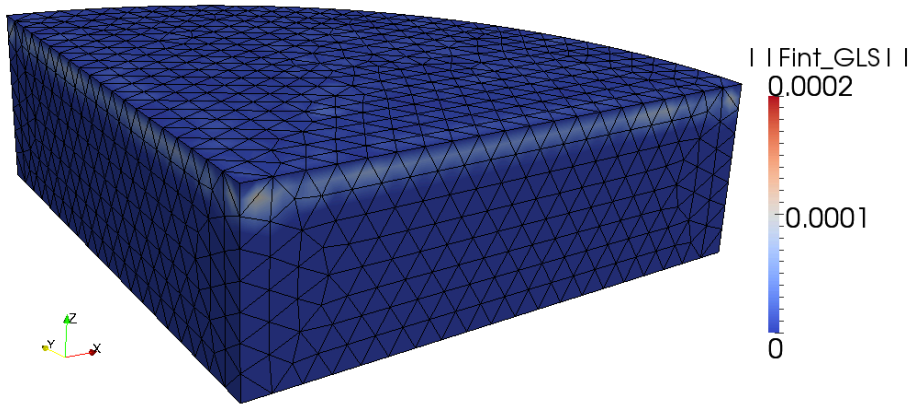

Figure VII.18: Contour plot of the norm of $\mathbf{F}^{int}_{u,GLS}$ at t=1s

VII.4 Conclusion

It was observed that an hyperelastic biphasic model, implemented in a finite element framework with Taylor-Hood tetrahedral elements, exhibits non-physical pressure oscillations for low permeabilities. A Galerkin least-square formulation was derived for finite deformations in order to stabilise these oscillations.

In the context of near to uni-axial fluid flow, the current formulation shows good results. It eliminates the spurious oscillations for most meshes (and damp the oscillations for others meshes) and also prevents these oscillations from propagating towards the centre of the medium as reported for very coarse meshes. The solution scheme proved to be robust when tested against various mesh densities, permeabilities, loading rates, compressive strains and time steps. It is also worth mentioning that the

benefits of this formulation come at minimal computational cost, as no additional degrees of freedom are required.

However, benefits observed for unconfined compression tests could not be replicated under confinement. In this case, it was demonstrated that the stabilisation factor is overestimated, which in turn results in an overestimation of the pressure distribution. Simulations with lower stabilisation factor indicated the existence of an optimised stabilisation factor for this particular confined compression analysis. This suggest the necessity to further develop this framework so that the stabilisation factor can adapt to various boundary conditions, and as suggested in Truty (2001), the directionality of the fluid flow and solid stiffness.

Chapter VIII

Preliminary tests on an idealised intervertebral disc

The objective of this chapter is to assess the current state of development of the implemented biphasic swelling model. A methodology is presented to assign properties to the fibres of the annulus fibrosus on the created idealised geometry. The model's behaviour, tested on an idealised diurnal cycle, demonstrates a number of the features of the model. It also shows relatively large deformations compared to published data. It is believed that this is due to the fact that induced deformations under compressive loading fail to engage the fibres. This is followed by a discussion proposing areas requiring further attention to potentially solve this shortcoming.

VIII.1 Geometry and mesh

An idealised disc geometry was created using an image of the mid-sagittal section of the lumbar disc already presented in Chapter II on Fig. II.2a. The points on the disc's outer boundary, as well as the interface between the nucleus and the annulus, were digitised (see illustration on Fig. VIII.1a). The main dimensions are approximately 40mm in the x-direction and 30mm in the y-direction. Subsequently, this set of data points was imported into the mesh generation toolkit Cubit (developed by the Sandia National Laboratories), and duplicated twice in order to obtain a top, mid and bottom section of the IVD. This is shown on Fig. VIII.1b, where points are connected by splines. Note that the mid-section was slightly expanded radially to create a radial bulge. Both the top and the bottom surfaces are perfectly flat and parallel, resulting in a 10mm thick disc.

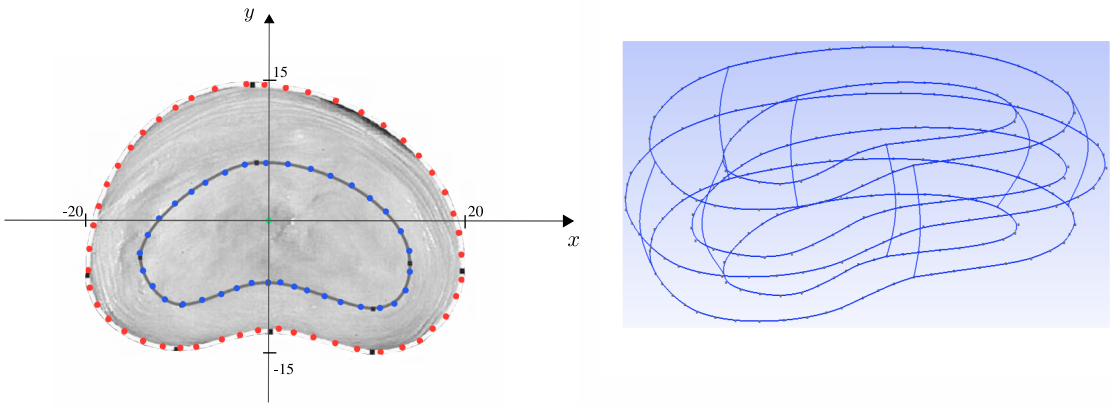

(a) Digitised contours points of the nucleus pulposus and annulus fibrosus

(b) Contour splines of the idealised IVD

Figure VIII.1: Steps toward the generation of the idealised model

The final geometry is presented on Fig. VIII.2a. It reveals the separate volumes of the nucleus pulposus and the annulus fibrosus, which are used to identify different material properties (e.g. stiffness, permeability, anisotropy).

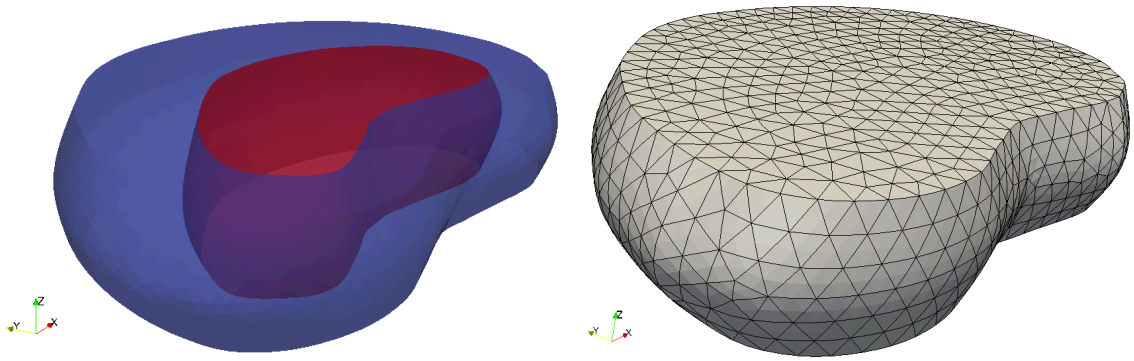

(a) AF and NP boundaries

(b) Mesh IVD3

Figure VIII.2: The disc's discretised geometry

Further to observations made in Chapter VII, it will be of great interest to investigate the convergence of the model and assess the performance of the stabilisation framework on a full disc. To this end, 5 meshes are created (IVD1, IVD2, IVD3, IVD4 and IVD5), the characteristics of which can be found in Table VIII.1. The mesh IVD3 is presented on Fig. VIII.2b.

	Nodes	Elements	Size (mm)	Elements across thickness
IVD1	6514	4186	3.0	4
IVD2	11002	7242	2.5	5
IVD3	20381	13725	2.0	6
IVD4	44793	30912	1.5	8
IVD5	66809	46548	1.3	9

Table VIII.1: Mesh characteristics - Size is an average of the elements' edge length

VIII.2 Fibres orientation and material parameters

The annulus fibrosus is a multi-lamellar structure of highly organised collagen fibres (see description in Sec. II.1 and Sec. VI.1.2). The orientation of the fibres alternates between adjacent lamellae, in directions referred to as $\mathbf{a}_0$ and $\mathbf{b}_0$. Fibre material parameters are evaluated using experimental results from Holzapfel et al. (2005), reproduced with markers on Fig. VIII.3a. The published data, resulting from uni-axial extension tests performed on single lamellae of human annulus fibrosus, characterise the evolution of the engineering stress as the stretch increases. In 3D, engineering stresses correspond to the first Piola-Kirchhoff stress tensor P_{fibre}, which can be evaluated in 1D for a single family of fibres as:

$$P_{\text{fibre}} = F_S S_{\text{fibre}} = \lambda S_{\text{fibre}} = 2k_1 \lambda \left(\lambda^2 - 1\right) \exp\left[k_2 \left(\lambda^2 - 1\right)^2\right] \tag{VIII.2.1}$$

A least square fit with an iterative solver is then built in the space $\mathbf{k} = (k_1, k_2)$ to fit the material parameters. Each of the four data sets has N data points. We first define a local residual at each of the data points (λ_i, P_i):

$$r_i = P_i - P_{\text{fibre}}(\lambda_i, k_1, k_2) \quad i \in \{1, N\} \tag{VIII.2.2}$$

The global error measure is defined as the square of the local residuals:

$$R = \sum_i^N r_i^2 \tag{VIII.2.3}$$

In order to minimise the global residual, we seek:

$$\mathbf{e} = \text{grad}\, R = \begin{Bmatrix} \frac{\partial R}{\partial k_1} \\ \frac{\partial R}{\partial k_2} \end{Bmatrix} = \mathbf{0} \tag{VIII.2.4}$$

The first order Taylor series expansion of $\mathbf{e}$ about $\mathbf{k}^i = \mathbf{k}^{i-1} + \delta\mathbf{k}$:

$$\mathbf{e}^i = \mathbf{e}^{i-1} + \frac{\partial \mathbf{e}}{\partial \mathbf{k}} \delta\mathbf{k} \tag{VIII.2.5}$$

The jacobian:

$$\frac{\partial \mathbf{e}}{\partial \mathbf{k}} = \begin{bmatrix} \frac{\partial^2 R}{\partial k_1^2} & \frac{\partial^2 R}{\partial k_1 \partial k_1^2} \\ \frac{\partial^2 R}{\partial k_2 \partial k_1} & \frac{\partial^2 R}{\partial k_2^2} \end{bmatrix} \tag{VIII.2.6}$$

can be inverted and Eq. VIII.2.5 iteratively solved for $\mathbf{e}^i = \mathbf{0}$:

$$\begin{cases} \delta\mathbf{k} = \left(\frac{\partial \mathbf{e}}{\partial \mathbf{k}}\right)^{-1} \mathbf{e}^{i-1} \\ \mathbf{k}^i = \mathbf{k}^{i-1} + \delta\mathbf{k} \end{cases} \tag{VIII.2.7}$$

The iterative solver was then used to fit the experimental data of Holzapfel et al. (2005). The resulting sets of parameters k_1 and k_2 are presented in Table (VIII.2) and the corresponding stress-stretch plotted on Fig. (VIII.3a).

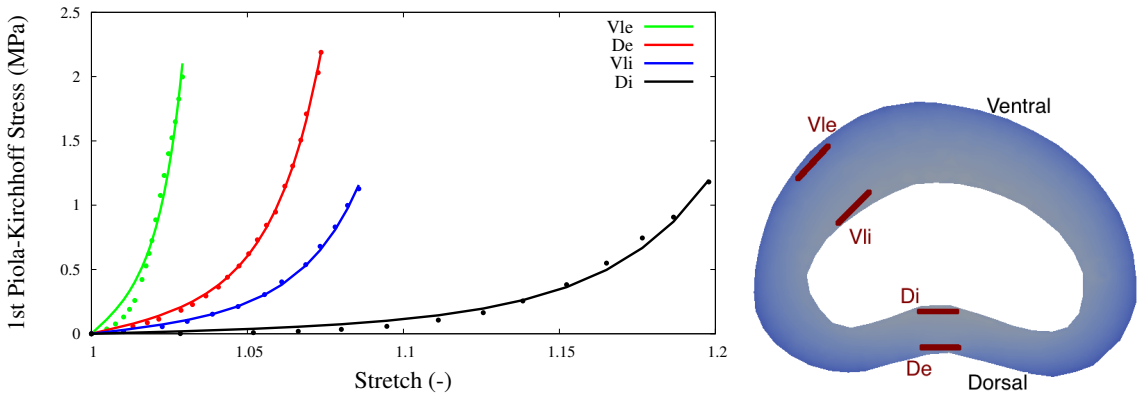

(a) (b)

Figure VIII.3: a) Comparison of the 1^{st} Piola-Kirchhoff in a uni-axial test from Holzapfel experiments Holzapfel et al. (2005) (markers) and best fit using the model derived in Eberlein et al. (2001) (lines) - b) Gauge location

It is interesting to see that the properties of the fibres considerably depend on their position in the annulus. Although all fibres experience stiffening, those located near

the outer annulus (Vle and De) are substantially stiffer than fibres located closer to the nucleus, which exhibit a longer toe-region.

	Vle	De	Vli	Di
k_1 (MPa)	5.49	1.38	0.70	0.15
k_2	326.26	67.87	45.60	10.66

Table VIII.2: Material parameters k_1 and k_2 for positions Vle, De, Vli and Di shown on Fig. VIII.3b

Finally, the fibre orientation is implemented as follows (see illustration in Fig. VIII.4). Starting with a cross section of the IVD in the mid-sagittal plane and its centre of gravity O. For each point A of the annulus fibrosus:

- the polar angle $\theta = (\mathbf{y}_1, \overrightarrow{OA})$ is determined
- the fibre angle φ is evaluated using the linear regression proposed in Holzapfel et al. (2005): $|\varphi| = 23.2 + 0.13 \times \theta$
- the point T, defined as the closest point to A on the outer boundary, is sought
- the secondary coordinate system $(\mathbf{x}_2, \mathbf{y}_2, \mathbf{z}_1)$ is defined so that we have: $\mathbf{x}_2 = \frac{\overrightarrow{AT}}{||\overrightarrow{AT}||}$, $\mathbf{x}_2 \cdot \mathbf{y}_2 = 0$ and $\mathbf{x}_2 \times \mathbf{y}_2 = \mathbf{z}_1$
- both fibre angles families are finally positioned in the plane $(A\mathbf{y}_2\mathbf{z}_1)$ so that:

$$\mathbf{a_0} = \begin{Bmatrix} \cos\varphi \\ 0 \\ \sin\varphi \end{Bmatrix} \qquad \mathbf{b_0} = \begin{Bmatrix} -\cos\varphi \\ 0 \\ \sin\varphi \end{Bmatrix} \tag{VIII.2.8}$$

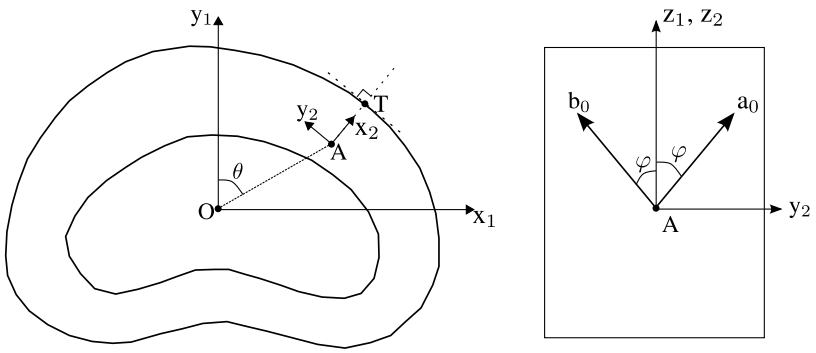

Figure VIII.4: Methodology to build the fibre orientation - Left: IVD section in transverse plane defining point A in the annulus - Right: corresponding fibre plane (Ay_2z_1)

A representation of the evolution of the orientation of the fibres with the polar angle can be seen on Fig. VIII.5:

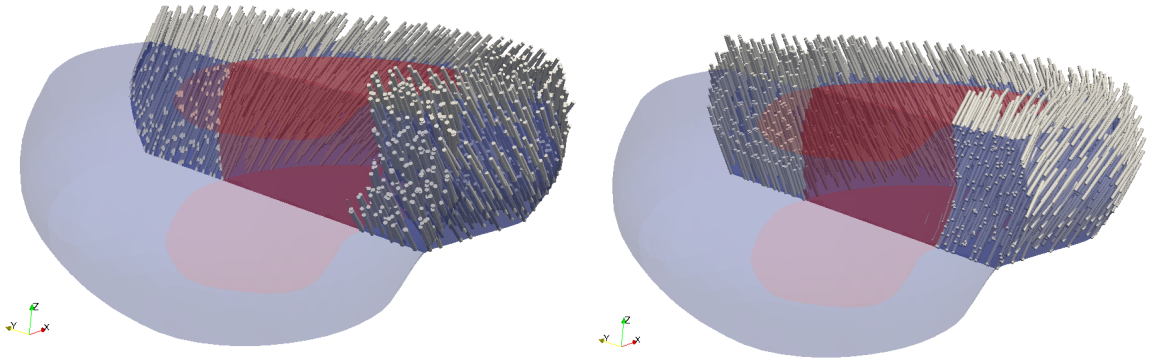

(a) Family 1 (b) Family 2

Figure VIII.5: A representation of the fibres orientation within the annulus

VIII.3 Qualitative numerical results

The performance of the implemented biphasic swelling model is qualitatively investigated in a series of simple tests involving compressive loading and creep events. The disc's response is compared to data found in the literature and the mechanisms governing the behaviour of the IVD are inspected. Additionally, this test allows the convergence of the model to be verified and to assess the benefits of the GLS stabilisation. This is followed by a discussion assessing the current development and associated limitations.

VIII.3.1 Response to a diurnal cycle

Long-term loading is herein considered by investigating the response of the disc to an idealised daily loading. A total compressive load of 440N is applied to the disc in 6min 20s, which is representative of the load transfered through the spine in relaxed erect posture as mentioned in Chapter II. Since the superior surface is approximately 1000mm^2, this is equivalent to applying a 0.4MPa traction at a rate of 1kPa.s^{-1}. Subsequently, the disc is left to relax under this load for a further 16 hours, representing the span of a day. At this point the load is removed at the same rate it was applied. The loading pattern is shown on Fig. VIII.6

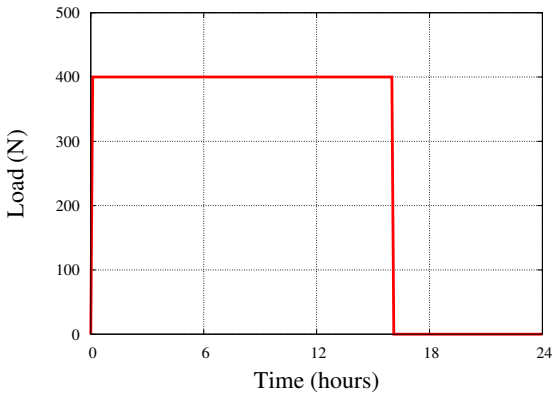

Figure VIII.6: Idealised daily loading

The material parameters were taken from Eberlein et al. (2001), Gu et al. (1999) and Karajan (2009) (from the latter, using elastic parameters from the model without viscosity). The initial permeability is set to 1×10^{-3}mm^4 N^{-1} s^{-1} throughout the entire disc. Regarding the solid matrix, the shear modulus is μ=0.5 MPa for the nucleus and μ=1 MPa for the annulus, while $\lambda = 0.5$MPa everywhere.

As the endplates and vertebral bodies are not explicitly modelled, idealised boundary conditions are applied to the upper and lower surfaces of the disc:

- It is assumed that the whole of the disc's boundary experiences free-flow. Aside from the lateral boundary where fluid flow is not hindered, this assumption is motivated by the fact that the thin cartilage endplates, located at the superior and inferior surfaces, exhibit permeability of similar magnitude as the disc's (approximately 7.5×10^{-3}mm^4 N^{-1} s^{-1} as reported in Ferguson et al. (2004) from literature review). The endplates are connected to bony structures, which have a very high permeability of 2×10^{5}mm^4 N^{-1} s^{-1} (from the same study). Therefore, this assumption is equivalent to underestimating the endplate's permeability and assuming that free-flow is permitted through the bone. This naturally overestimates the ability of the fluid to flow axially in the IVD.

- The upper and lower surfaces of the disc are fully bonded to the endplates and the vertebrae. As it is reported in Ferguson et al. (2004) that the cancellous and cortical bone respectively have elastic moduli of 100MPa and 10000MPa, it will be assumed that these surfaces cannot expand radially.

Before discussing the response of the disc, the performance of the GLS stabilisation is briefly investigated. To this end, and in a similar fashion to that in Sec. VII.3.2,

the convergence upon mesh refinement of the displacements at the top of the disc and the pressure at the centre are scrutinised (see Fig. VIII.7).

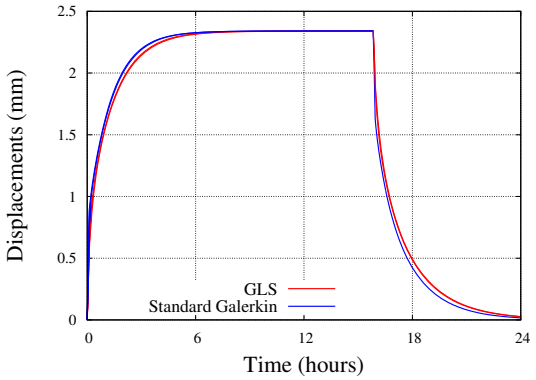

(a) Downward displacements measured at the centre of the top surface

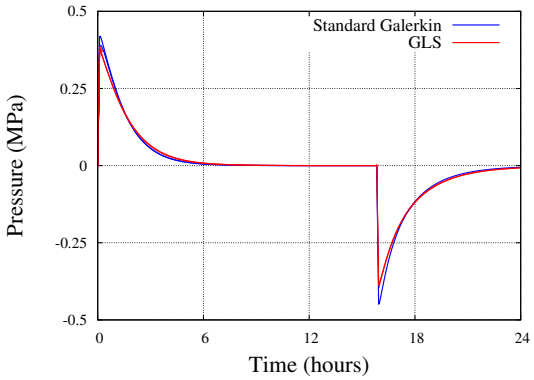

(b) Hydrostatic pressure measured at the centre for disc

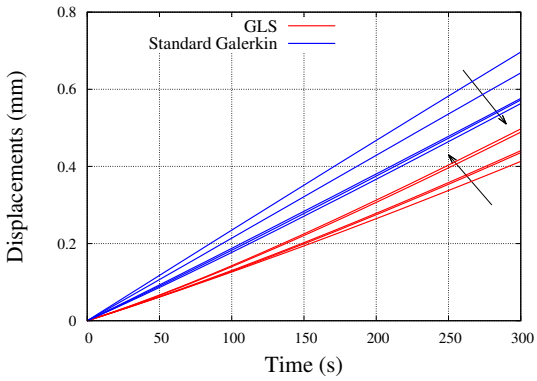

(c) Downward displacements measured at the centre of the top surface - Loading phase

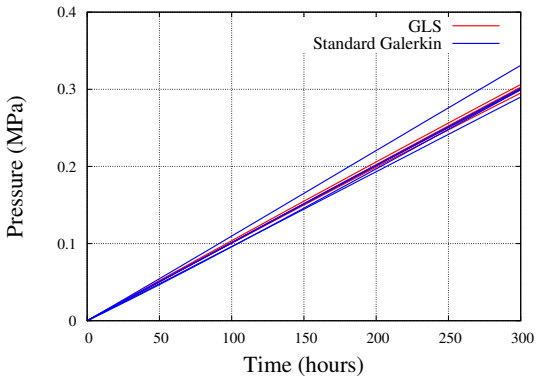

(d) Hydrostatic pressure measured at the centre for disc - Loading phase

Figure VIII.7: Convergence for pressure and displacement, for both standard Galerkin and GLS formulations - Arrows on (c) indicate mesh refinement

Although finer meshes would be required to demonstrate the actual convergence, the stabilised and non-stabilised solutions in displacement exhibit similar rates of convergence (Fig. VIII.7c). Fig. VIII.7d shows, similarly to the unconfined compression test presented in Sec. VII.3.1, that pressure levels at the centre of the sample remain unaffected by either mesh refinement or stabilisation. This comes with the exception of the mesh IVD1 in the un-stabilised case, due to the fact that the standard Galerkin solution exhibits strong instabilities, which can be observed as deep as the centre of the disc for the mesh IVD1 (see Fig. VIII.8a). Generally, Fig. VIII.7 reveals that, under these conditions, the adverse effects of the GLS stabilisations presented in Sec. VII.3.2 are not materialising. The spurious jumps previously observed at the

early stages of the simulation for the reaction vs time response are not reproduced in the displacements vs time response (see Fig. VIII.7c). Note that all examples were displacement controlled in Chapter VII and are force controlled in the present chapter.

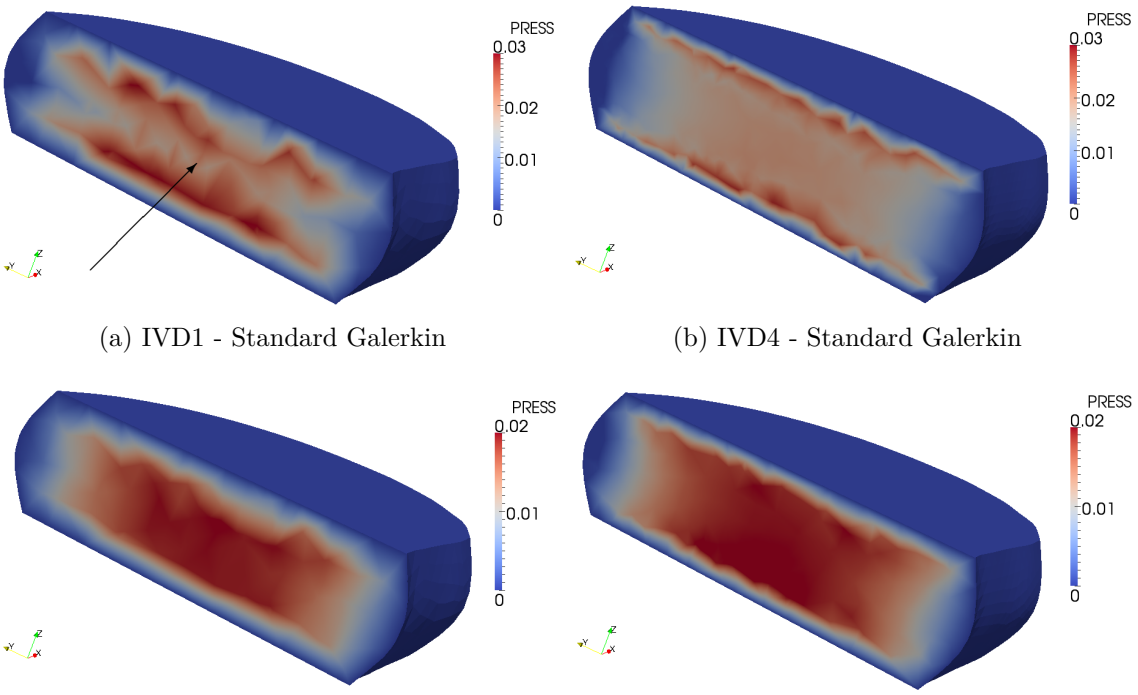

(a) IVD1 - Standard Galerkin

(b) IVD4 - Standard Galerkin

(c) IVD1 - GLS

(d) IVD4 - GLS

Figure VIII.8: Pressure at the centre of the disc with and without stabilisation at t=20s - The arrow on (a) indicates a location where spurious oscillations propagated to the centre

At the end of the loading ramp, the centre of the superior face displaced vertically by 0.65mm (see Fig. VIII.7c for mesh IVD5), which represents a 6.5% decrease of the disc's height. Steady state is reached after approximately 6 hours, at which point the disc's height decreased by 23% at the centre of the disc. This is accompanied by a maximum radial bulge of 1.02mm in the x-direction, 1.1mm anteriorly and 1.2mm posteriorly (i.e. the positive and negative y-direction respectively). Upon unloading, the steady state, which corresponds to the initial configuration, is reached within 6 hours.

However, Fig. VIII.9 reveals that during the loading phase, the top surface experiences greater displacements in the region of the annulus fibrosus.

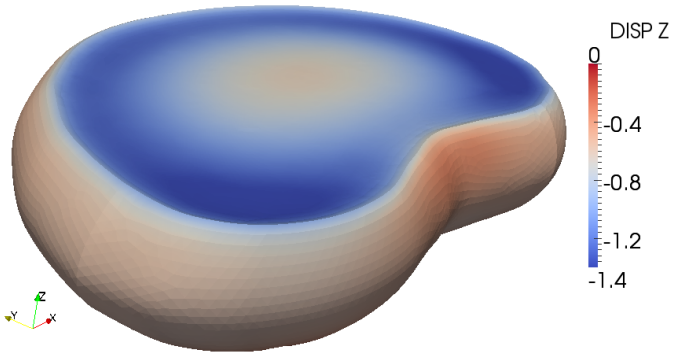

Figure VIII.9: Vertical displacements on the deformed geometry at the end of the ramp

This is the result of a mechanism combining high fluid pressurisation in the volume enclosed by the nucleus pulposus on the one hand and radial bulging of the annulus fibrosus on the other hand. Axially, near the centre, the disc behaves in a similar manner as samples subjected to confined compression, as described in Chapter V. This is materialised by circles in Fig. VIII.10, where the nucleus experiences little radial expansion and constant pressure. This pattern is repeated for each z-ordinate. First, this pressurisation prevents the centre from large downward displacements. Second, it forces the annulus to bulge outwards. Near the outer boundary, as Fig. VIII.10b shows, the axial compressive loads are not resisted by pressurisation as free flow is permitted. This, combined with the absence of radial constrains, explain the displacement pattern observed in Fig. VIII.9.

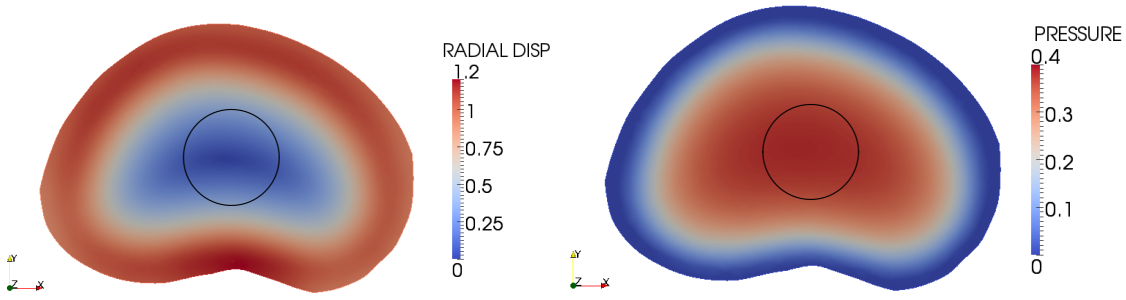

(a) Radial displacements (b) Pressure

Figure VIII.10: At the end of the loading ramp, radial displacements (a) and pressure (b) contour plots in the mid-sagittal section

This analogy with the 1D model is further motivated by the osmotic pressure distribution depicted on Fig. VIII.11. Due to the nature of the constitutive model (Eq. VI.1.7), the osmotic pressure is an inverse law of the mixture's volume change.

Regions where the osmotic pressure exceeds the initial osmotic pressure of 0.1MPa experience compaction, as observed near the top and bottom surfaces. The core of the IVD remains largely unaffected by volume changes, while the regions of high bulging experienced a mild volume increase.

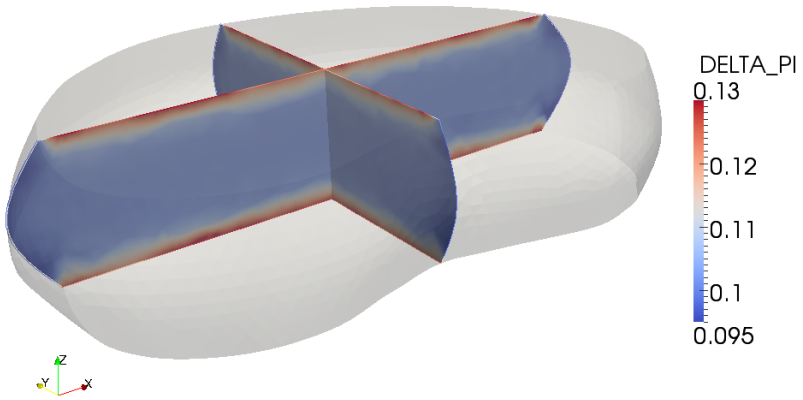

Figure VIII.11: At the end of the loading ramp, contour plot of the osmotic pressure distribution across the thickness of the disc

VIII.3.2 Discussion

Comparing the numerical results to experimental data is a challenging task. It is partly due to the fact that the primary focus of present work was limited to the development of a computational framework for the modeling of the disc, but also due to the difficulty in identifying published experimental setups suited for a truly equivalent comparison: species (e.g. human, porcine, rat, bovine), disc's geometry, boundary conditions, loading conditions (e.g. type of loading, rate), method of determining height reduction (i.e. centre, side or average) and predominantly the physiological conditions of the tissue (i.e. age/degeneration, water content, strain/stress state at the start of the experiment).

Experimental work focussing on geometrical changes of the intervertebral disc essentially falls into three categories:

- *in-vivo* experiments usually focus on changes in stature (i.e body, rather than individual disc, height change) when a patient performs pre-determined activities (e.g. sitting, standing, lifting a weight). This is for example the case in Tyrell et al. (1985) and Broberg (1993), where daily body height changes under normal activity are estimated to 20mm. This loss of stature, which represents the cumulative compression of each of the 23 discs, cannot be apportioned to

each disc as they all vary in shape and size (i.e. thicker and wider in the lumbar region), but also experience different levels of loading. Another considerable difference with the above simulation is the complex interaction with surrounding muscles, ligament and vertebra's facet joints and neural arch, resulting in intricate loading of the disc.

- *in-vitro* experiments using so called motion segments, which are functional units vertebrae-disc-vertebrae, where external soft tissues and bony parts are kept intact.
  - Adams et al. (1996a) reported approximately 0.6mm displacement under 1500N axial load applied fast (rate not specified)
  - Campana et al. (2011) measured a displacement of 1.3mm when 400N are applied in 30s (i.e rate of 13N.s^{-1}), and a total of 1.45mm after 5 minutes of creep
- *in-vitro* experiments on motion segments, after removal of posterior bony structures, muscles and ligaments:
  - Heuer et al. (2007) reported 1.14mm after immediate application of 500N and 1.3mm after 15 minutes
  - in another experimental setup, O'Connell et al. (2011) measured 2.08mm when 2000N are applied at 1N.s^{-1} (i.e. after 33 minutes)
  - another loading case in O'Connell et al. (2011), 0.75mm were measured after rapid application of 400N, with a total of 2.85mm after 8h.

In an attempt to explain these large discrepancies, O'Connell et al. (2011) argued that, in addition to the issues mentioned at the beginning of this section, the mechanisms within the disc are highly dependent on the rate and duration of loading. Additionally, it is also argued that creep-recovery tests are different from diurnal tests, mainly because of the initial state of the disc.

However, it seems that preliminary results from the current model consistently overestimate axial displacements. This seems to also apply to lateral bulging, which was reported in Heuer et al. (2007, 2008) under 400N compressive load to be 0.6mm in the x-direction, 0.8mm anteriorly and 1mm posteriorly (resp. 1.02, 1.1 and 1.2 in our analysis). At this juncture, it is worth noting potential issues over the fibres' response and the mechanisms that engage them. As Fig. VIII.12 shows, only the outer fibres of the annulus are participating to the stiffening of the disc, with a maximum fibre strain of 3%, compared to the 6.7% reported in Heuer et al. (2008) for similar levels

of compression (albeit more rapidly applied). This is not the anticipated behaviour of the annulus.

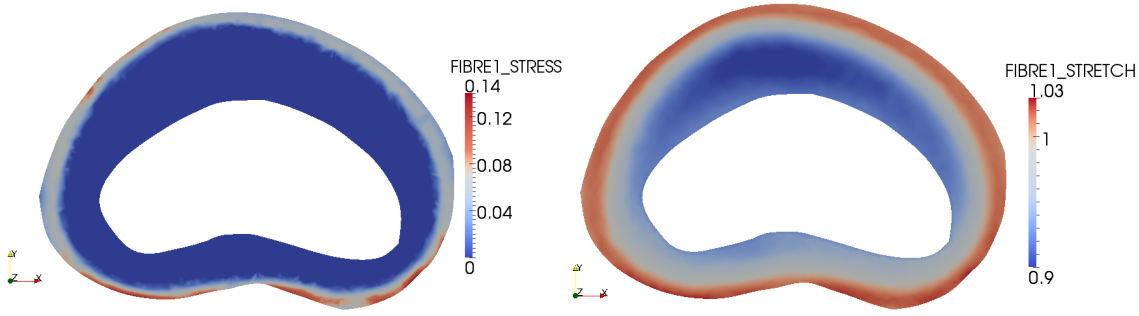

(a) Stress in fibres (b) Stretch in fibres

Figure VIII.12: At the end of the loading ramp, mid-sagittal section: stress (a) and stretch (b) distributions in the fibres

Investigation of the principal stretches within the annulus fibrosus reveals that the largest principal stretch is compressive in the height of the lamella near the mid-sagittal plane of the disc (i.e. compression in the plane of the fibres, normal to the hoop direction) and compression perpendicularly to the plane of the fibres near the top and bottom surfaces. This is illustrated in Fig. VIII.13a. The second largest principal stretch is tension in the hoop direction (VIII.13b). Although tension in the hoop direction seems intuitive, the other principal stretch was anticipated to be tensile along the height of the lamella, following rotation of the tissue due to bulging.

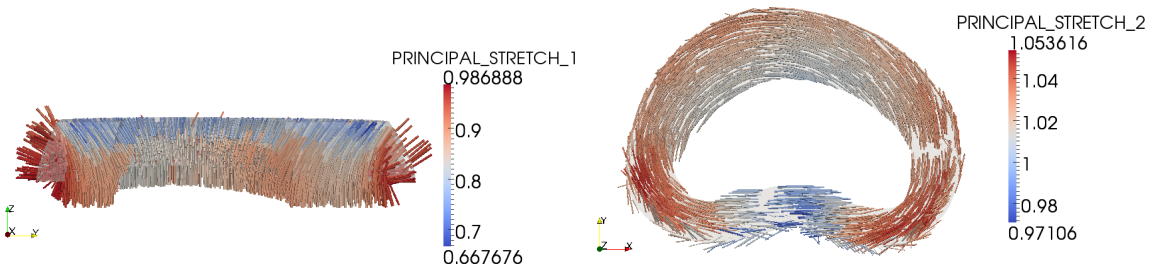

(a) Direction of the principal stretch 1 in the upper left side of the AF (b) Direction of the principal stretch 2 in the mid-sagittal plane

Figure VIII.13: The direction of the two largest principal stretches within the annulus fibrosus

This bi-axial compression-tension state suggests that the inactivation of the fibres is not caused by errors in the implementation of the fibre model (e.g. orientation, stress and stress derivation), but rather by more complex phenomena. Before investigating

what these might be, two further tests are performed in order to gain confidence on the fibres' implementation.

First, the ramp of the diurnal test is revisited, with the fibres positioned along the hoop direction, i.e. in the sagittal plane following the curvature of the annulus. This is to verify that the fibres are engaged as expected when oriented in a direction that is known to experience tension (see Fig. VIII.13b). This resulted in fibre stretching across the whole width of the annulus, and a decrease in the displacement of 16% vertically and 22% radially.

In a second test, bending about the X-axis is applied to the top surface of the disc. Fig. VIII.14a shows the external nodal forces; note that the magnitude of the nodal force vectors is not fully linear along the Y-axis because it is proportional to the surface area of the element it is connected to. Over 200s, a total compressive force of 130N is applied, together with a bending moment of 650N.mm.

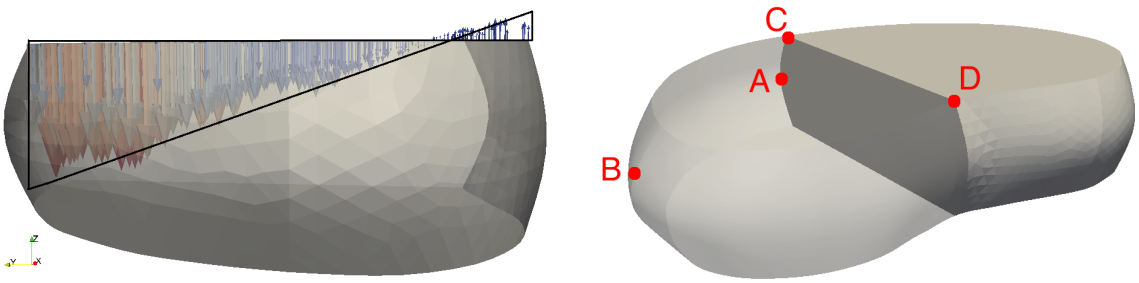

(a) External nodal forces (b) Control points

Figure VIII.14: External nodal forces applied for bending about X-axis (a) and location of the control points

Four different configurations are compared. Fibres are not considered in the reference case, making case 1 fully isotropic. Case 2 includes fibres as described in Sec. VIII.2. Case 3 is similar to case 2, but with stiffness parameters increased by 10%. Case 4 is also a variation of case 2, but fibres are initially pre-stretched by 5%. As essential and natural boundary conditions cannot be applied simultaneously, case 4 necessitated an equilibrium phase prior to loading, effectively cancelling the pre-stretch. A similar test was run, where the bending was applied in displacement control (i.e. without equilibrium phase), showing similar results to case 4.

	case 2	case 3	case 4
$u_{y,A}$	-1.07	-1.25	-1.58
$u_{x,B}$	-1.13	-1.26	-3.44
$u_{z,C}$	0.22	0.24	-0.56
$u_{z,D}$	-35.66	-44.62	-35.61

Table VIII.3: Difference (%) in displacements at control points between case 1 and case 2-4

Table VIII.3 clearly indicates that the fibres only marginally contribute toward the disc's stiffness. The only impact takes place on the tension side (point D), where the loading direction is close to the fibres' direction and therefore directly activating them.

The last two tests further demonstrate that fibres respond as expected when the continuum experiences tension in the fibres' direction. This suggests a shortcoming in the overall behaviour of the isotropic biphasic medium. Although more tests are clearly necessary to draw strong conclusions, a few potential reasons are proposed to explain this behaviour:

- *The initial conditions.* The state of the tissue is experimentally far more complex than in the idealised model. The solid matrix, as well as the fibres, physiologically present an intricate stress state across the disc, which is not accounted for in the simulations. Moreover, the annulus exhibits residual stresses even for the unloaded disc Michalek et al. (2012). Additionally, the idealised model should take into consideration the conditioning of the tissue performed in the experiments, which includes initial compression and swelling. Finally, the behaviour of the tissue is highly related to the osmotic pressure distribution and the level of hydration, which have not been accounted for accurately. These considerations naturally impact the initial stiffness of the tissue.

- *The influence of the loading rate.* As demonstrated in O'Connell et al. (2011), the disc's behaviour is highly dependent of the rate at which it is loaded. Unfortunately, it was not possible to achieve faster rates of loading in the present study to verify the importance of the phenomenon.

- *The material parameters.* Few numerical studies considered the investigation of the model's sensitivity on material parameters. In Karajan (2009), it was found that the impact of the parameters describing the solid phase play a non-negligible role in the way the disc pressurises and deforms. As literature is

abundant in material parameters, sometimes spanning several order of magnitude, it would be of great interest to explore this area, and in particular the λ which controls the ability of the mixture to undergo volumetric changes. It is also reasonable to question whether the chosen Neo-Hookean model is adequate to properly describe the behaviour of the disc.

- *The fibre model.* A possible shortcoming of the current formulation is that in reality, fibres are discrete entities, spanning between superior and inferior vertebral bodies. This implies that the behaviour of the annulus fibrosus, say at the bottom of the disc, is not completely independent from deformations occurring at the top of the disc. This is not accounted for in the continuum model, where there is no information at the point level about the stress state at the other end of the fibres.

- *Boundary conditions.* Constraints at the top and bottom surfaces have been so far crudely modelled. Although it is not expected to drastically modify the current global behaviour, finer stiffness and permeability should be defined at these location by specifically modelling the endplates and the vertebral bodies.

VIII.4 Conclusion

This chapter was concerned with the application of the 3D biphasic swelling model to the particular case of the intervertebral disc. A methodology was presented to create a simple geometry, and assign properties to the annulus fibrosus. The idealised disc's response to a ramp-creep loading showed excessive axial and lateral displacements compared to published experimental data, as the deformation mechanism within the tissue fails to trigger stretching of the fibres, as would be expected. Further tests are required to solve this shortcoming. Of particular interest, the influence of the loading rates and the refinement of the initial state of the tissue should be investigated. Although preliminary simulations show encouraging result regarding the GLS stabilisation, the performance has yet to be tested once fibres are properly activated and offer more confinement to the nucleus pulposus.

Chapter IX

Overview

The computational modelling of the intervertebral disc is a truly inter-disciplinary process. The first task was to build understanding of the intervertebral disc as a structure, and more specifically, to identify the salient features the model needed to exhibit in order to accurately describe the disc's behaviour. This was complemented by a review of existing soft tissue models, and in particular those related to articular cartilage. The difficulty was to find a balance between essential features and what could reasonably be implemented within the scope of this project. This was achieved by defining a modelling philosophy and the establishment of a consistent level of complexity for the model.

Subsequently, the theoretical framework could be derived. It involved building proficiency in mixture and finite deformation theories, and enhancements to include the osmotic pressure and strain dependent permeability. Computational aspects started at this stage only, with the derivation of an iterative solver. The implementation of the three dimensional, nonlinear finite element code was in itself a substantial task. It turned particularly rewarding to design the verification methodology, not only because this stepwise procedure ensured a steady progression of the implementation, but also because it provided a deeper understanding of the nature of the governing equations and of the model in general.

Numerical instabilities materialised as an unforeseen challenge, which, although exciting, hindered the progression toward a more mature model of the disc. Other techniques were envisaged to tackle this issue, for example $\bar{\mathbf{F}}$, without success. Although it was beyond the scope of the thesis, it would have been interesting to further investigate the origin of these instabilities, and in particular the reason why it has not been more widely reported in other publications. Potential directions could have been the implementation of a viscous model, brick elements, or linear approximations of the displacement field, all of which seem to have been extensively used in other

studies.

The results obtained both in 1D and 3D, showed the potential of the proposed framework even if the 3D model requires further consideration to offer a faithful representation of the intervertebral disc. This involves a number of aspects, the most crucial of which is thought to be the determination of finer initial conditions for the simulations. The significance of the initial state of the tissue on its behaviour have been discussed in a number of sections, and needs to be addressed in the model in a more physiologically representative manner. It was also reported that the biphasic swelling model is markedly sensitive to material parameters. It would therefore be of great interest to quantify this sensitivity, but also the sensitivity to loading rates. Finally, the derivation of a specific constitutive model for intervertebral disc tissue could be beneficial.

To conclude, the main achievements of this thesis are concisely reiterated:

- **Theoretical framework:** a model based on mixture theory under finite deformations was formulated, with particular attention to the treatment of osmotic and rate-dependent effects.

- **Numerical treatment:** the weak form of the resulting set of governing equations was derived and linearised, enabling the use of a Newton-Raphson scheme. A specific termination criteria was derived for the iterative solver.

- **1D implementation:** the biphasic swelling model was restricted to the one dimensional case and implemented in Matlab. Validation against experimental data demonstrated the capabilities of the model and facilitated familiarity with the mechanics of porous and soft tissues.

- **3D implementation:** a methodology was specifically designed for the verification of the implementation of the biphasic swelling model in a C/C++ code.

- **Stabilisation:** a Galerkin least-square stabilisation framework was formulated to address the encountered numerical instabilities. Performances and limitations of this technique were clearly demonstrated.

- **Full IVD tests:** preliminary tests were performed on an idealised intervertebral disc, which demonstrated a number of the features of the model. Areas requiring further developments were identified.

Bibliography

M.A. Adams and W.C. Hutton. The effect of posture on the fluid content of lumbar intervertebral discs. *Spine*, 8(6):665–71–, September 1983.

M.A. Adams, D.S. McNally, H. Chinn, and P. Dolan. Posture and the compressive strength of the lumbar spine. *Clinical Biomechanics*, 9(1):5–14, January 1994. ISSN 0268-0033.

M.A. Adams, D.W. McMillan, T.P. Green, and P. Dolan. Sustained loading generates stress concentrations in lumbar intervertebral discs. *Spine*, 21(4):434–438, FEB 15 1996a. ISSN 0362-2436. 1st ISSLS Basic Science Meeting, BRUSSELS, BELGIUM, AUG 26-27, 1994.

M.A. Adams, D.S. McNally, and P. Dolan. 'stress' distributions inside intervertebral discs - the effects of age and degeneration. *Journal of Bone and Joint Surgery-British Volume*, 78B(6):965–972, November 1996b.

M.A. Adams, B.J.C. Freeman, H.P. Morrison, I.W. Nelson, and P. Dolan. Mechanical initiation of intervertebral disc degeneration. *Spine*, 25(13):1625–1636, July 2000.

M.A. Adams, N. Bogduk, K. Burton, P. Dolan, and B.J.C. Freeman. *The Biomechanics of Back Pain*. Elsevier, 2006.

M.A. Adams, M. Stefanakis, and P. Dolan. Healing of a painful intervertebral disc should not be confused with reversing disc degeneration: Implications for physical therapies for discogenic back pain. *Clinical Biomechanics*, 25(10):961 – 971, 2010. ISSN 0268-0033. doi: DOI:10.1016/j.clinbiomech.2010.07.016.

G. Aguilar, F. Gaspar, F. Lisbona, and C. Rodrigo. Numerical stabilization of biot's consolidation model by a perturbation on the flow equation. *Int. J. Numer. Meth. Engng.*, 75(11):1282–1300, 2008. ISSN 1097-0207.

E.S. Almeida and R.L. Spilker. Finite element formulations for hyperelastic transversely isotropic biphasic soft tissues. *Computer Methods in Applied Mechanics*

and Engineering, 151(3-4):513–538, 1998. ISSN 0045-7825. doi: DOI:10.1016/S0045-7825(97)82246-3. Containing papers presented at the Symposium on Advances in Computational Mechanics.

G.B.J. Andersson. Epidemiological features of chronic low-back pain. *The Lancet*, 354(9178):581–585, August 1999. ISSN 0140-6736. doi: 10.1016/S0140-6736(99)01312-4.

M. Argoubi and A. Shirazi-Adl. Poroelastic creep response analysis of a lumbar motion segment in compression. *Journal of Biomechanics*, 29(10):1331–1339, oct 1996.

G.A. Ateshian and J. A. Weiss. Anisotropic hydraulic permeability under finite deformation. *Journal of Biomechanical Engineering*, 132(11):111004, 2010. doi: 10.1115/1.4002588.

G.A. Ateshian, M.B. Albro, S. Maas, and J.A. Weiss. Finite element implementation of mechanochemical phenomena in neutral deformable porous media under finite deformation. *Journal of Biomechanical Engineering-transactions of the Asme*, 133 (8):081005, August 2011. doi: 10.1115/1.4004810.

R.J. Atkin and R.E. Craine. Continuum theories of mixtures - basic theory and historical development. *Quarterly Journal of Mechanics and Applied Mathematics*, 29:209–244, 1976. doi: 10.1093/qjmam/29.2.209.

D.C. Ayotte, S. Tepic, and K. Ito. Fluid flow in the intervertebral disc and its relation to disc degeneration. *Journal of Bone and Joint Surgery (BR)*, 81-B (Suppl. 1): 67, 1999.

U.M. Ayturk, J.J. Garcia, and C.M. Puttlitz. The micromechanical role of the annulus fibrosus components under physiological loading of the lumbar spine. *J. Biomech. Eng.*, 132(6):061007–8, June 2010.

N.M. Bachrach, V.C. Mow, and F. Guilak. Incompressibility of the solid matrix of articular cartilage under high hydrostatic pressures. *Journal of Biomechanics*, 31 (5):445–451, May 1998. doi: 10.1016/S0021-9290(98)00035-9.

E. Baer, J.J. Cassidy, and A. Hiltner. Hierarchical structure of collagen composite systems - lessons from biology. *Pure and applied chemistry*, 63(7):961–973, July 1991. ISSN 0033-4545.

S. Balay, W.D. Gropp, L. Curfman McInnes, and B.F. Smith. Efficient management of parallelism in object oriented numerical software libraries. In E. Arge,

A. M. Bruaset, and H. P. Langtangen, editors, *Modern Software Tools in Scientific Computing*, pages 163–202. Birkhäuser Press, 1997.

S. Balay, J. Brown, K. Buschelman, W.D. Gropp, D. Kaushik, M.G. Knepley, L. Curfman McInnes, B.F. Smith, and H. Zhang. PETSc users manual. Technical Report ANL-95/11 - Revision 3.2, Argonne National Laboratory, 2011a.

S. Balay, J. Brown, K. Buschelman, W.D. Gropp, D. Kaushik, M.G. Knepley, L. Curfman McInnes, B.F. Smith, and H. Zhang. PETSc Web page, 2011b. http://www.mcs.anl.gov/petsc.

M.C. Battie and T. Videman. Lumbar disc degeneration: Epidemiology and genetics. *Journal of Bone and Joint Surgery-american Volume*, 88A:3–9, 2006. doi: 10.2106/JBJS.E.01313.

T. Belytschko, W. K. Liu, and B. Moran. *Nonlinear Finite Elements for Continua and Structures*. John Wiley & Sons, 2000.

M.A. Biot. General theory of three dimensional consolidation. *Journal of Applied Physics*, 12:155–164, February 1941.

M.A. Biot. General solutions of the equations of elasticity and consolidation for a porous material. *Journal of Applied Mechanics*, 23:91–96, March 1956.

M.A. Biot. Theory of finite deformations of porous solids. *Indiana University Mathematics Journal*, 21(7):597–620, 1972. doi: 10.1512/iumj.1972.21.21048.

J. Bonet and R.D. Wood. *Nonlinear Continuum Mechanics for Finite Element Analysis*. Cambridge University Press, 2nd edition edition, 2008.

N. Boos, R. Rieder, V. Schade, K.F. Spratt, N. Semmer, and M. Aebi. The diagnostic accuracy of magnetic resonance imaging, work perception, and psychosocial factors in identifying symptomatic disc herniations. *Spine*, 20(24):2613–2625, 1995.

R.M. Bowen. Toward a thermodynamics and mechanics of mixtures. *Archive for Rational Mechanics and Analysis*, 24(5):370–403, January 1967. ISSN 0003-9527.

R.M Bowen. Incompressible porous media models by use of the theory of mixtures. *International Journal of Engineering Science*, 18(9):1129–1148, 1980. ISSN 0020-7225. doi: 10.1016/0020-7225(80)90114-7.

R.M. Bowen. Compressible porous-media models by use of the theory of mixtures. *International Journal of Engineering Science*, 20(6):697–735, 1982. doi: 10.1016/0020-7225(82)90082-9.

F. Brezzi and M. Fortin. *Mixed and Hybrid Finite Element Methods*. Springer-Verlag, 1991.

K.B. Broberg. Slow deformation of intervertebral discs. *Journal of Biomechanics*, 26 (4-5):501 – 512, 1993. ISSN 0021-9290. doi: DOI:10.1016/0021-9290(93)90012-4.

S. Campana, E. Charpail, J.A. de Guise, L. Rillardon, W. Skalli, and D. Mitton. Relationships between viscoelastic properties of lumbar intervertebral disc and degeneration grade assessed by mri. *Journal of the Mechanical Behavior of Biomedical Materials*, 4(4):593–599, May 2011. ISSN 1751-6161.

D. Chapelle and K.J. Bathe. The inf-sup test. *Computers & Structures*, 47(4-5): 537–545, June 1993. ISSN 0045-7949.

Y. Chen, X. Chen, and T. Hisada. Non-linear finite element analysis of mechanical electrochemical phenomena in hydrated soft tissues based on triphasic theory. *International Journal for Numerical Methods in Engineering*, 65(2):147–173, 2006.

K.M.C. Cheung, D. Samartzis, J. Karppinen, F.P.S. Mok, D.W.H. Ho, D.Y.T. Fong, and K.D.K. Luk. Intervertebral disc degeneration: New insights based on "skipped" level disc pathology. *Arthritis & Rheumatism*, 62(8):2392–2400, 2010. ISSN 1529-0131. doi: 10.1002/art.27523.

M.B. Coventry. Anatomy of the intervertebral disks. *Clinical Orthopaedics and Related Research*, 67:9–15, 1969.

S.C. Cowin. Bone poroelasticity. *Journal of Biomechanics*, 32(3):217–238, March 1999. ISSN 0021-9290. doi: 10.1016/S0021-9290(98)00161-4.

H. Darcy. *Les fontaines publiques de la ville de Dijon*. Victor Dalmont, 1856.

R. de Boer. Highlights in the historical development of the porous media theory: Toward a consistent macroscopic theory. *Appl. Mech. Rev.*, 49(4):201–262, April 1996.

R. de Boer. Theory of porous media - past and present. *Z. angew. Math. Mech.*, 78 (7):441–466, 1998. ISSN 1521-4001.

R. de Boer. Porous media theory: A survey. *Z. angew. Math. Mech.*, 80(S1):133–136, 2000. ISSN 1521-4001.

R. de Boer. *Trends in Continuum Mechanics of Porous Media*. Sp, 2005.

R. de Boer and W. Ehlers. A historical review of the formulation of porous media theories. *Acta Mechanica*, 74(1):1–8, 1988. ISSN 0001-5970.

R. de Borst, J. Réthoré, and M.-A. Abellan. A numerical approach for arbitrary cracks in a fluid-saturated medium. *Archive of Applied Mechanics*, 75:595–606, 2006. ISSN 0939-1533. 10.1007/s00419-006-0023-y.

E. A. de Souza Neto, D. Peric, and D. R. J. Owen. *Computational Methods for Plasticity*. John Wiley and Sons, Ltd, 2008.

G. deBotton, I. Hariton, and E.A. Socolsky. Neo-hookean fiber-reinforced composites in finite elasticity. *Journal Of The Mechanics And Physics Of Solids*, 54(3):533–559, mar 2006.

R. Eberlein, G.A. Holzapfel, and C.A.J. Schulze-Bauer. An anisotropic model for annulus tissue and enhanced finite element analyses of intact lumbar disc bodies. *Computer Methods in Biomechanics and Biomedical Engineering*, 4(3):209–229, 2001. ISSN 1025-5842.

R. Eberlein, G.A. Holzapfel, and M. Frohlich. Multi-segment FEA of the human lumbar spine including the heterogeneity of the annulus fibrosus. *Computational Mechanics*, 34(2):147–163, July 2004.

W. Ehlers. *Porous media: theory, experiments and numerical applications*, chapter 1: Foundations of multiphasic and porous materials, pages 3–86. Springer, Berlin, 2002.

W. Ehlers and A. Acarturk. The role of weakly imposed dirichlet boundary conditions for numerically stable computations of swelling phenomena. *Computational Mechanics*, 43(4):545–557, mar 2009.

W. Ehlers, N. Karajan, and B. Markert. A porous media model describing the inhomogeneous behaviour of the human intervertebral disc. *Materialwissenschaft und Werkstofftechnik*, 37(6):546–551, 2006.

W. Ehlers, N. Karajan, and B. Markert. An extended biphasic model for charged hydrated tissues with application to the intervertebral disc. *Biomechanics and Modeling in Mechanobiology*, 8(8):1617–7959, 2008.

W. Ehlers, A. Acarturk, and N. Karajan. Advances in modelling saturated soft biological tissues and chemically active gels. *Archive of Applied Mechanics*, pages – , 2009.

J. Eisenfeld, V.C. Mow, and H. Lipshitz. Mathematical-analysis of stress relaxation in articular-cartilage during compression. *Mathematical Biosciences*, 39(1-2):97–112, 1978. doi: 10.1016/0025-5564(78)90029-9.

D.M. Elliott and L.A. Setton. A linear material model for fiber-induced anisotropy of the anulus fibrosus. *Journal Of Biomechanical Engineering - Transactions of ASME*, 122(2):173–179, APR 2000. ISSN 0148-0731.

S.J. Ferguson, K. Ito, and L.-P. Nolte. Fluid flow and convective transport of solutes within the intervertebral disc. *Journal of Biomechanics*, 37(2):213–221, feb 2004.

A. Fick. Ueber diffusion. *Ann. Phys.*, 170(1):59–86, 1855. ISSN 1521-3889.

L.P. Franca and T.J.R. Hughes. Two classes of mixed finite element methods. *Computer Methods in Applied Mechanics and Engineering*, 69(1):89–129, July 1988. ISSN 0045-7825. doi: 10.1016/0045-7825(88)90168-5.

A.J. Freemont, T.E. Peacock, P. Goupille, J.A. Hoyland, J. OBrien, and M.I.V. Jayson. Nerve ingrowth into diseased intervertebral disc in chronic back pain. *Lancet*, 350(9072):178–181, July 1997. doi: 10.1016/S0140-6736(97)02135-1.

A.J.H. Frijns. *A Four-Component Mixture Theory Applied to Cartilaginous Tissues*. PhD thesis, Eindhoven University of Technology, 2000.

A.J.H. Frijns, J.M. Huyghe, and J.D. Janssen. A validation of the quadriphasic mixture theory for intervertebral disc tissues. *International Journal Of Engineering Science*, 35(15):1419–1429, 1997.

F.H. Geisler, S.L. Blumenthal, R.D. Guyer, P.C. McAfee, J.J. Regan, J.P. Johnson, and B. Mullin. Neurological complications of lumbar artificial disc replacement and comparison of clinical results with those related to lumbar arthrodesis in the literature: results of a multicenter, prospective, randomized investigational device exemption study of charité intervertebral discs. *Journal of Neurosurgery: Spine*, 1 (2):143–154, 2004. doi: 10.3171/spi.2004.1.2.0143. PMID: 15346999.

M.G. Glover, A.R. Hargens, M.M. Mahmood, S. Gott, M.D. Brown, and S.R. Garfin. A new technique for the in vitro measurement of nucleus pulposus swelling pressure. *Journal of Orthopaedic Research*, 9(1):61–67, 1991. ISSN 1554-527X. doi: 10.1002/jor.1100090109.

M.L. Goins, D.W. Wimberley, P.S. Yuan, L.N. Fitzhenry, and A.R. Vaccaro. Nucleus pulposus replacement: an emerging technology. *The Spine Journal*, 5(6, Supplement 1):317, 2005.

W.Y. Gu, X.G. Mao, R.J. Foster, M. Weidenbaum, V.C. Mow, and B.A. Rawlins. The anisotropic hydraulic permeability of human lumbar anulus fibrosus: Influence of age, degeneration, direction, and water content. *Spine*, 24(23):–, 1999. ISSN 0362-2436.

H.L. Guerin and D.M. Elliott. Quantifying the contributions of structure to annulus fibrosus mechanical function using a nonlinear, anisotropic, hyperelastic modelso. *Journal of Orthopaedic Research*, 25(4):508–516, April 2007. doi: 10.1002/jor.20324.

Z.Y. Guo, F. Caner, X. Peng, and B. Moran. On constitutive modelling of porous neo-hookean composites. *Journal of the Mechanics and Physics of Solids*, In Press, Corrected Proof, 2007.

T.R. Haher, M. O'Brien, J.W. Dryer, R. Nucci, R. Zipnick, and D.J. Leone. The role of the lumbar facet joints in spinal stability: Identification of alternative paths of loading. *Spine*, 19(23):2667–2670, 1994.

H.V. Henderson and S.R. Searle. On deriving the inverse of a sum of matrices. *SIAM Review*, 23(1):53–60, January 1981. ISSN 00361445.

P. Heneghan and P.E. Riches. Experimental determination of the strain-dependent aggregate modulus and ionic osmotic pressure of the bovine nucleus pulposus. *Journal of Biomechanics*, 40(Supplement 2):312, 2007. ISSN 0021-9290. doi: DOI:10.1016/S0021-9290(07)70308-1. Program and Abstracts of the XXI Congress, International Society of Biomechanics.

P. Heneghan and P.E. Riches. The strain-dependent osmotic pressure and stiffness of the bovine nucleus pulposus apportioned into ionic and non-ionic contributors. *Journal of Biomechanics*, 41(11):2411–2416, 2008a. ISSN 0021-9290. doi: DOI: 10.1016/j.jbiomech.2008.05.025.

P. Heneghan and P.E. Riches. Determination of the strain-dependent hydraulic permeability of the compressed bovine nucleus pulposus. *Journal of Biomechanics*, 41 (4):903–906, 2008b.

F. Heuer, H. Schmitt, H. Schmidt, L Claes, and H.-J. Wilke. Creep associated changes in intervertebral disc bulging obtained with a laser scanning device. *Clinical Biomechanics*, 22(7):737 – 744, 2007. ISSN 0268-0033. doi: DOI:10.1016/j.clinbiomech.2007.04.010.

F. Heuer, H. Schmidt, and H.-J. Wilke. The relation between intervertebral disc bulging and annular fiber associated strains for simple and complex loading. *Journal of Biomechanics*, 41(5):1086–1094, 2008. ISSN 0021-9290. doi: 10.1016/j.jbiomech.2007.11.019.

N.T. Hollingsworth and D.R. Wagner. Modeling shear behavior of the annulus fibrosus. *Journal of the Mechanical Behavior of Biomedical Materials*, 4(7):1103–1114, October 2011. ISSN 1751-6161. doi: 10.1016/j.jmbbm.2011.03.019.

M.H. Holmes. A theoretical-analysis for determining the nonlinear hydraulic permeability of a soft-tissue from a permeation experiment. *Bulletin of Mathematical Biology*, 47(5):669–683, 1985. doi: 10.1016/S0092-8240(85)90027-8.

M.H. Holmes. Finite deformation of soft-tissue. analysis of a mixture model in uniaxial compression. *Journal of Biomechanical engineering - Transactions of the ASME*, 108(4):372–381, NOV 1986. ISSN 0148-0731.

M.H. Holmes and V.C. Mow. The nonlinear characteristics of soft gels and hydrated connective tissues in ultrafiltration. *Journal of Biomechanics*, 23(11):1145–1156, 1990. ISSN 0021-9290. doi: DOI:10.1016/0021-9290(90)90007-P.

M.H. Holmes, W.M. Lai, and V.C. Mow. Singular perturbation analysis of the nonlinear, flow-dependent compressive stress-relaxation behavior of articular-cartilage. *Journal of Biomechanical Engineering-transactions of the Asme*, 107(3):206–218, 1985.

G.A. Holzapfel, C.A.J. Schulze-Bauer, G. Feigl, and P. Regitnig. Single lamellar mechanics of the human lumbar anulus fibrosus. *Biomechanics and Modeling in Mechanobiology*, 3(3):125–140, 2005.

A.H. Hsieh, D.R. Wagner, L.Y. Cheng, and J.C. Lotz. Dependence of mechanical behavior of the murine tail disc on regional material properties: A parametric finite element study rid a-5684-2010. *Journal of Biomechanical Engineering-transactions of the Asme*, 127(7):1158–1167, December 2005. doi: 10.1115/1.2073467.

T.J.R. Hughes. *The Finite Element Method*. Prentice Hall, 1987.

T.J.R. Hughes, L.P. Franca, and G.M. Hulbert. A new finite element formulation for computational fluid dynamics: Viii. the galerkin/least-squares method for advective-diffusive equations. *Computer Methods in Applied Mechanics and Engineering*, 73(2):173–189, May 1989. ISSN 0045-7825.

M. Hussain, R.N. Natarajan, G. Chaudhary, H.S. An, and G.B.J. Andersson. Relative contributions of strain-dependent permeability and fixed charged density of proteoglycans in predicting cervical disc biomechanics: A poroelastic c5-c6 finite element model study. *Medical Engineering & Physics*, 33(4):438–445, May 2011. doi: 10.1016/j.medengphy.2010.11.011.

J.M. Huyghe and J.D. Janssen. Quadriphasic mechanics of swelling incompressible porous media. *International Journal of Engineering Science*, 35(8):793–802, 1997. ISSN 0020-7225. doi: DOI:10.1016/S0020-7225(96)00119-X.

J.C. Iatridis, M. Weidenbaum, L.A. Setton, and V.C. Mow. Is the nucleus pulposus a solid or a fluid?: Mechanical behaviors of the nucleus pulposus of the human intervertebral disc. *Spine*, 21(10):1174–1184, may 1996.

J.C. Iatridis, L.A. Setton, M. Weidenbaum, and V.C. Mow. The viscoelastic behavior of the non-degenerate human lumbar nucleus pulposus in shear. *Journal of Biomechanics*, 30(10):1005 – 1013, 1997. ISSN 0021-9290. doi: DOI: 10.1016/S0021-9290(97)00069-9.

J.C. Iatridis, L.A. Setton, R.J. Foster, B.A. Rawlins, M. Weidenbaum, and V.C. Mow. Degeneration affects the anisotropic and nonlinear behaviors of human anulus fibrosus in compression. *Journal of Biomechanics*, 31(6):535–544, JUN 1998. ISSN 0021-9290.

J.C. Iatridis, J.P. Laible, and M.H. Krag. Influence of fixed charge density magnitude and distribution on the intervertebral disc: Applications of a poroelastic and chemical electric (peace) model. *Journal of Biomechanical Engineering - Transactions of ASME*, 125(1):12–24, FEB 2003. ISSN 0148-0731. doi: 10.1115/1.1533804.

J.J.T. Jim, N. Noponen-Hietala, K.M.C. Cheung, J. Ott, J. Karppinen, A. Sahraravand, K.D.K. Luk, S.P. Yip, P.C. Sham, Y.Q. Song, J.C.Y. Leong, K.S.E. Cheah, L. Ala-Kokko, and D. Chan. The trp2 allele of col9a2 is an age-dependent risk factor for the development and severity of intervertebral disc degeneration. *Spine*, 30(24):2735–2742, December 2005. doi: 10.1097/01.brs.0000190828.85331.ef.

W. Johannessen and D.M. Elliott. Effects of degeneration on the biphasic material properties of human nucleus pulposus in confined compression. *Spine*, 30(24): E724–E729, DEC 15 2005. ISSN 0362-2436.

N. Karajan. *An Extended Biphasic Description of the Inhomogeneous and Anisotropic Intervertebral Disc*. PhD thesis, Universitat Stuttgart, 2009.

S.M. Klisch and J.C. Lotz. Application of a fiber-reinforced continuum theory to multiple deformations of the annulus fibrosus. *Journal of Biomechanics*, 32(10): 1027–1036, October 1999.

J. Korsawe and G. Starke. A least-squares mixed finite element method for biot's consolidation problem in porous media. *Siam Journal On Numerical Analysis*, 43 (1):318–339, 2005. doi: 10.1137/S0036142903432929.

J. Kraemer, D. Kolditz, and R. Gowin. Water and electrolyte content of human intervertebral disks under variable load. *Spine*, 10(1):69–71, 1985. doi: 10.1097/00007632-198501000-00011.

G. Kreichati, F. Kassab, and K. Kharrat. Herniated intervertebral disc associated with a lumbar spine dislocation as a cause of cauda equina syndrome: a case report. *European Spine Journal*, 15:1015–1018, 2006. ISSN 0940-6719. 10.1007/s00586-005-0947-x.

M.K. Kwan, W.M. Lai, and V. Mow. A finite deformation theory for cartilage and other soft hydrated connective tissues–i. equilibrium results. *Journal of Biomechanics*, 23(2):145 – 155, 1990. ISSN 0021-9290. doi: DOI:10.1016/0021-9290(90)90348-7.

W.M. Lai and V.C. Mow. Drag-induced compression of articular-cartilage during a permeation experiment. *Biorheology*, 17(1-2):111–123, 1980.

W.M. Lai, V.C. Mow, and V. Roth. Effects of nonlinear strain-dependent permeability and rate of compression on the stress behavior of articular cartilage. *J. Biomech. Eng.*, 103(2):61–66, May 1981.

W.M. Lai, J.S. Hou, and V.C. Mow. A triphasic theory for the swelling and deformation behaviors of articular-cartilage. *Journal Of Biomechanical Engineering-Transactions Of The Asme*, 113(3):245–258, 1991.

J.P. Laible, D.S . Pflaster, M.H. Krag, B.R. Simon, and L.D. Haughe. A poroelastic-swelling finite-element model with application to the intervertebral disc. *Spine*, 18 (5):659–670, April 1993. doi: 10.1097/00007632-199304000-00019.

Y. Lanir. Biorheology and fluid flux in swelling tissues .1. bicomponent theory for small deformations, including concentration effects. *Biorheology*, 24(2):173–187, 1987.

C.K. Lee. Accelerated degeneration of the segment adjacent to a lumbar fusion. *Spine*, 13(3):375–377, March 1988. doi: 10.1097/00007632-198803000-00029.

L.P. Li, J. Soulhat, M.D. Buschmann, and A. Shirazi-Adl. Nonlinear analysis of cartilage in unconfined ramp compression using a fibril reinforced poroelastic model. *Clinical Biomechanics*, 14(9):673–682, November 1999. doi: 10.1016/S0268-0033(99)00013-3.

L.P. Li, A. Shirazi-Adl, and M.D. Buschmann. Investigation of mechanical behavior of articular cartilage by fibril reinforced poroelastic models. *Biorheology*, 40(1-3): 227–233, 2003.

N. Maniadakis and A. Gray. The economic burden of back pain in the uk. *Pain*, 84 (1):95–103, January 2000. doi: 10.1016/S0304-3959(99)00187-6.

B. Markert, W. Ehlers, and N. Karajan. A general polyconvex strain-energy function for fiber-reinforced materials. *Proc. Appl. Math. Mech.*, 5(1):245–246, 2005. ISSN 1617-7061.

J.B. Martinez, V.O.A. Oloyede, and N.D. Broom. Biomechanics of load-bearing of the intervertebral disc: an experimental and finite element model. *Medical Engineering & Physics*, 19(2):145–156, mar 1997.

D.W. McMillan, D.S. McNally, G. Garbutt, and M.A. Adams. Stress distributions inside intervertebral discs: the validity of experimental "stress profilometry'. *Proc Inst Mech Eng H*, 210(2):81–7, 1996.

D.S. McNally, I.M. Shackleford, A.E. Goodship, and R.C. Mulholland. In vivo stress measurement can predict pain on discography. *Spine*, 21(22):2580–2587, November 1996. doi: 10.1097/00007632-199611150-00007.

A.J. Michalek, M.G. Gardner-Morse, and J.C. Iatridis. Large residual strains are present in the intervertebral disc annulus fibrosus in the unloaded state. *Journal of Biomechanics*, 45(7):1227 – 1231, 2012. ISSN 0021-9290. doi: 10.1016/j.jbiomech.2012.01.042.

J.A.A. Miller, C. Schmatz, and A.B. Schultz. Lumbar-disk degeneration - correlation with age, sex, and spine level in 600 autopsy specimens. *Spine*, 13(2):173–178, February 1988. doi: 10.1097/00007632-198802000-00008.

K. Miller. How to test very soft biological tissues in extension? *Journal of Biomechanics*, 34(5):651–657, May 2001. doi: 10.1016/S0021-9290(00)00236-0.

L.W. Morland. A simple constitutive theory for a fluid-saturated porous solid. *J. Geophys. Res.*, 77(5):890–900, 1972. ISSN 0148-0227.

V.C. Mow and J.M. Mansour. The nonlinear interaction between cartilage deformation and interstitial fluid flow. *Journal of Biomechanics*, 10(1):31–39, 1977. ISSN 0021-9290. doi: 10.1016/0021-9290(77)90027-6.

V.C. Mow, S.C. Kuei, W.M. Lai, and C.G. Armstrong. Biphasic creep and stress-relaxation of articular-cartilage in compression - theory and experiments. *Journal Of Biomechanical Engineering-Transactions Of The Asme*, 102(1):73–84, 1980.

A. Nachemson and J.M. Morris. In vivo measurements of intradiscal pressure: Discometry, a method for the determination of pressure in the lower lumbar discs. *J Bone Joint Surg Am*, 46(5):1077–1092, 1964.

R.N. Natarajan, J.H. Ke, and G.B. Andersson. A model to study the disc degeneration process. *Spine*, 19(3):259–265, February 1994. doi: 10.1097/00007632-199402000-00001.

R.N. Natarajan, J.R. Williams, S.A. Lavender, and G.B.J. Andersson. Poro-elastic finite element model to predict the failure progression in a lumbar disc due to cyclic loading. *Computers & Structures*, 85(11-14):1142–1151, jun 2007.

N.L. Nerurkar, R.L. Mauck, and D. M. Elliott. ISSLS prize winner: Integrating theoretical and experimental methods for functional tissue engineering of the annulus fibrosus. *Spine*, 33(25):2691–2701, DEC 1 2008. ISSN 0362-2436.

J. Noailly, D. Lacroix, and J.A. Planell. Finite element study of a novel intervertebral disc substitute. *Spine*, 30(20):2257–2264, OCT 15 2005. ISSN 0362-2436.

G.D. O'Connell, N.T. Jacobs, S. Sen, E.J. Vresilovic, and D.M. Elliott. Axial creep loading and unloaded recovery of the human intervertebral disc and the effect of degeneration. *Journal of the Mechanical Behavior of Biomedical Materials*, 4(7):933–942, October 2011. ISSN 1751-6161. doi: 10.1016/j.jmbbm.2011.02.002.

S. Olsen, A. Oloyede, and C. Adam. A finite element formulation and program to study transient swellling and load-carriage in healthy and degenerate articular cartilage. *Computer Methods in Biomechanics and Biomedical Engineering*, 7(2):111–120, 2004. doi: 10.1080/10255840410001672185.

D. Perie, D. Korda, and J.C Iatridis. Confined compression experiments on bovine nucleus pulposus and annulus fibrosus: sensitivity of the experiment in the determination of compressive modulus and hydraulic permeability. *Journal of Biomechanics*, 38(11):2164 – 2171, 2005. ISSN 0021-9290. doi: DOI:10.1016/j.jbiomech.2004.10.002.

C.A. Pezowicz. Analysis of selected mechanical properties of intervertebral disc annulus fibrosus in macro and microscopic scale. *Journal of Theoretical and Applied Mechanics*, 48:917–932, 2010. ISSN 1429-2955.

C.A. Pezowicz, P.A. Robertson, and N.D. Broom. The structural basis of interlamellar cohesion in the intervertebral disc wall. *Journal of Anatomy*, 208(3):317–330, 2006. ISSN 1469-7580.

A. Polikeit, L.P. Nolte, and S. J. Ferguson. Simulated influence of osteoporosis and disc degeneration on the load transfer in a lumbar functional spinal unit. *Journal of Biomechanics*, 37(7):1061–1069, jul 2004.

P. Pollintine, P. Dolan, J.H. Tobias, and M.A. Adams. Intervertebral disc degeneration can lead to "stress-shielding" of the anterior vertebral body - a cause of osteoporotic vertebral fracture? *Spine*, 29(7):774–782, April 2004. doi: 10.1097/01.BRS.0000119401.23006.D2.

A. Przybyla, P. Pollintine, R. Bedzinski, and M.A. Adams. Outer annulus tears have less effect than endplate fracture on stress distributions inside intervertebral discs: Relevance to disc degeneration. *Clinical Biomechanics*, 21(10):1013–1019, dec 2006.

P.P. Raj. Intervertebral disc: anatomy-physiology-pathophysiology-treatment. *Pain Pract*, 8(1):18–44–, 2008.

S. Rajasekaran, J.N. Babu, R. Arun, B.R.W. Armstrong, A.P. Shetty, and S. Murugan. Issls prize winner: A study of diffusion in human lumbar discs: A serial magnetic resonance imaging study documenting the influence of the endplate on diffusion in normal and degenerate discs. *Spine*, 29(23):2654–2667, December 2004. doi: 10.1097/01.brs.0000148014.15210.64.

M. Recuerda, S.P. Cote, I. Villemure, and D. Perie. Influence of experimental protocols on the mechanical properties of the intervertebral disc in unconfined compression. *Journal of Biomechanical Engineering-transactions of the Asme*, 133(7): 071006, July 2011. doi: 10.1115/1.4004411.

P.E. Riches. Indirectly determining permeability: effect of experimental sampling and hold time. In *Proceedings of the 9th International symposium on Computer Methods in Biomechanics and Biomedical Engineering; 24-27 February; Valencia, Spain*, 2010.

P.E. Riches. Sensitivity analysis of permeability parameters of bovine nucleus pulposus obtained through inverse fitting of the nonlinear biphasic equation: effect of sampling strategy. *Computer methods in biomechanics and biomedical engineering*, 15(1):29–36, July 2012.

P.E. Riches and D.S. McNally. A one-dimensional theoretical prediction of the effect of reduced end-plate permeability on the mechanics of the intervertebral disc. *Proceedings Of The Institution Of Mechanical Engineers Part H-Journal Of Engineering In Medicine*, 219(H5):329–335, sep 2005.

P.E. Riches, N. Dhillon, J. Lotz, A.W. Woods, and D.S. McNally. The internal mechanics of the intervertebral disc under cyclic loading. *Journal of Biomechanics*, 35(9):1263–1271, sep 2002.

S. Roberts, J.P.G. Urban, and S.M. Evans, H. and; Eisenstein. Transport properties of the human cartilage endplate in relation to its composition and calcification. *Spine*, 21(4):415–420, 1996.

H. Schmidt, A. Shirazi-Adl, F. Galbusera, and H.-J. Wilke. Response analysis of the lumbar spine during regular daily activities–a finite element analysis. *Journal of Biomechanics*, In Press, Corrected Proof:–, 2010. ISSN 0021-9290. doi: DOI: 10.1016/j.jbiomech.2010.03.035.

M.L. Schollum, P.A. Robertson, and N.D. Broom. ISSLS prize winner: Microstructure and mechanical disruption of the lumbar disc annulus part i: A microscopic investigation of the translamellar bridging network. *Spine*, 33(25):2702–2710, DEC 1 2008. ISSN 0362-2436.

Y. Schroeder, W. Wilson, J.M. Huyghe, and F.P.T. Baaijens. Osmoviscoelastic finite element model of the intervertebral disc. *European Spine Journal*, Volume 15, Supplement 3 / August, 2006:361–371, 2006.

Y. Schroeder, S. Sivan, W. Wilson, Y. Merkher, J.M. Huyghe, A. Maroudas, and F.P.T. Baaijens. Are disc pressure, stress, and osmolarity affected by intra- and extrafibrillar fluid exchange? *Journal of Orthopaedic Research*, 25(10):1317–1324, 2007.

Y. Schroeder, D.M. Elliott, W. Wilson, F.P.T. Baaijens, and J.M. Huyghe. Experimental and model determination of human intervertebral disc osmoviscoelasticity. *Journal of Orthopaedic Research*, 26(8):1141–1146, AUG 2008. ISSN 0736-0266. doi: 10.1002/jor.20632.

Y. Schroeder, J.M. Huyghe, C.C. van Donkelaar, and K. Ito. A biochemical/biophysical 3D FE intervertebral disc model. *Biomechanics And Modeling In Mechanobiology*, 9(5):641–650, 2010.

A. Schultz, G. Andersson, R. Ortengren, K. Haderspeck, and A. Nachemson. Loads on the lumbar spine - validation of a biomechanical analysis by measurements of intradiscal pressures and myoelectric signals. *Journal of Bone and Joint Surgery-american Volume*, 64(5):713–720, 1982.

H. Shankar, J.A. Scarlett, and S.E. Abram. Anatomy and pathophysiology of intervertebral disc disease. *Techniques in Regional Anesthesia and Pain Management*, 13(2):67–75, April 2009. ISSN 1084-208X. doi: 10.1053/j.trap.2009.05.001.

A. Shirazi-Adl. Nonlinear stress analysis of the whole lumbar spine in torsion - mechanics of facet articulation. *Journal of Biomechanics*, 27(3):289–299, March 1994. ISSN 0021-9290. doi: 10.1016/0021-9290(94)90005-1.

A. Shirazi-Adl, A.M. Ahmed, and S.C. Shrivastava. Mechanical response of a lumbar motion segment in axial torque alone and combined with compression. *Spine*, 11 (9):914–927, 1986a. doi: 10.1097/00007632-198611000-00012.

A. Shirazi-Adl, A.M. Ahmed, and S.C. Shrivastava. A finite element study of a lumbar motion segment subjected to pure sagittal plane moments. *Journal of Biomechanics*, 19(4):331–350, 1986b. ISSN 0021-9290. doi: 10.1016/0021-9290(86) 90009-6.

B.R. Simon. Multiphase poroelastic finite element models for soft tissue structures. *Applied Mechanics Review*, 45:191–218, June 1992.

B.R. Simon, J.S.S. Wu, M.W. Carlton, J.H. Evans, and L.E. Kazarian. Structural models for human spinal motion segments based on a poroelastic view of the intervertebral disk. *J. Biomech. Eng.*, 107(4):327–335, November 1985.

B.R. Simon, J.P. Liable, D. Pflaster, Y. Yuan, and M.H. Krag. A poroelastic finite element formulation including transport and swelling in soft tissue structures. *Journal Of Biomechanical Engineering-Transactions Of The Asme*, 118(1):1–9, feb 1996.

E. Sitthipornvorakul, P. Janwantanakul, N. Purepong, P. Pensri, and A. van der Beek. The association between physical activity and neck and low back pain: a systematic review. *European Spine Journal*, 20:677–689, 2011. ISSN 0940-6719. 10.1007/s00586-010-1630-4.

H. Snijders, J.M. Huyghe, and J.D. Janssen. Triphasic finite element model for swelling porous media. *International Journal for Numerical Methods in Fluids*, 20 (8-9):1039–1046, 1995.

A.J.M. Spencer. *Continuum Theory of the Mechanics of Fibre-Reinforced Composites*, chapter Constitutive theory for strongly anisotropic solids, pages 1–32. Springer, 1984.

J. Stefan. Uber das gleichgewicht und bewegung, insbesondere die diffusion von gemischen. *Sitzungsberichte der Kaiserlichen Akademie der Wissenschaften Wien*, 63:63–124, 1871.

I. Stokes, S. Chegini, S. Ferguson, M. Gardner-Morse, J. Iatridis, and J. Laible. Limitation of finite element analysis of poroelastic behavior of biological tissues undergoing rapid loading. *Annals of Biomedical Engineering*, 38(5):1780–1788, May 2010.

S. Strandring. *Gray's Anatomy*. Elsevier, 2008.

J.K. Suh, R.L. Spilker, and M.H. Holmes. A penalty finite element analysis for nonlinear mechanics of biphasic hydrated soft tissue under large deformation. *International Journal for Numerical Methods in Engineering*, 32(7):1411–1439, 1991.

S.J. Tang and B.J. Rebholz. Does anterior lumbar interbody fusion promote adjacent degeneration in degenerative disc disease? a finite element study. *Journal of Orthopaedic Science*, 16(2):221–228, March 2011. doi: 10.1007/s00776-011-0037-3.

T.J. Tautges, R.E. Meyers, K. Merkley, C. Stimpson, and C. Ernst. Moab: a mesh-oriented data base. Technical report, Sandia National Laboratories, Albuquerque, NM, Report SAND2004-1592 2004.

C. Taylor and P. Hood. A numerical solution of the navier-stokes equations using the finite element technique. *Computers & Fluids*, 1(1):73–100, January 1973. ISSN 0045-7930.

K. Terzaghi. Die berechnung der durchlassigkeitsziffer des tones aus dem verlauf der hydrodynamischen spannungserscheinungen. *Sitzungsbericht der Akademie der Wissenschaften (Wien): Mathematisch-Naturwissenschaftlichen Klasse*, 182:125–138, 1923.

K. Terzaghi. *Erdbaumechanik auf bodenphysikaliseher Grundlage*. Leipzig–Wien: Franz Deuticke, 1925.

C.A. Truesdell. Sulle basi della termomeccanica. *Rend.Lineei(8)*, 22:33–38, 1957.

C.A. Truesdell. *Rational Thermodynamics*, chapter Thermodynamics of diffusion, pages 219–236. Springer-Verlag, New-York, 2nd edition, 1984.

C.A. Truesdell and R.A. Toupin. *Handbuch der Physik*, volume Vol. III/1, chapter The classical field theories, pages 226–902. Springer-Verlag, Berlin, 1960.

C.A. Truesdell, W. Noll, and S.S. Antman. *The non-linear field theories of mechanics*. Springer-Verlag, Berlin, 1965.

A. Truty. A galerkin/least-squares finite element formulation for consolidation. *Int. J. Numer. Meth. Engng.*, 52(8):763–786, 2001. ISSN 1097-0207.

A. Truty. *On Certain Classes of Mixed and Stabilized Mixed Finite Element Formulations for Single and Two-phase Geomaterials*. Seria Inzynieria Srodowiska, 2002.

A.R. Tyrell, T. Reilly, and J.D.G. Troup. Circadian variation in stature and the effects of spinal loading. *Spine*, 10(2):161–164, 1985. doi: 10.1097/00007632-198503000-00011.

J. P. G. Urban and J. F. McMullin. Swelling pressure of the lumbar intervertebral discs: Influence of age, spinal level, composition, and degeneration. *Spine*, 13(2): –, 1988. ISSN 0362-2436.

J.P.G. Urban and S. Roberts. Degeneration of the intervertebral disc. *Arthritis Research & Therapy*, Vol 5 No 3:120–130, 2003.

J.P.G. Urban, S. Smith, and J.C.T. Fairbank. Nutrition of the intervertebral disc. *Spine*, 29(23):2700–2709, 2004.

J. Van Goethem, E. Van de Kelft, I. Biltjes, B. van Hasselt, L. van den Hauwe, P. Parizel, and A. De Schepper. Mri after successful lumbar discectomy. *Neuroradiology*, 38:S90–S96, 1996. ISSN 0028-3940. 10.1007/BF02278130.

R. van Loon, J.M. Huyghe, M.W. Wijlaars, and F.P.T. Baaijens. 3D FE implementation of an incompressible quadriphasic mixture model. *International Journal For Numerical Methods In Engineering*, 57(9):1243–1258, jul 2003.

W.J. Vankan, J.M. Huyghe, M.R. Drost, J.D. Janssen, and A. Huson. A finite element mixture model for hierarchical porous media. *International Journal for Numerical Methods in Engineering*, 40(2):193–210, 1997.

S.P. Veres, P.A. Robertson, and N.D. Broom. Issls prize winner: Microstructure and mechanical disruption of the lumbar disc annulus part ii: How the annulus fails under hydrostatic pressure. *Spine*, 33(25):2711–2720, DEC 1 2008. ISSN 0362-2436.

S.P. Veres, P.A. Robertson, and N.D. Broom. Issls prize winner: How loading rate influences disc failure mechanics a microstructural assessment of internal disruption. *Spine*, 35(21):1897–1908, October 2010. doi: 10.1097/BRS.0b013e3181d9b69e.

P.A. Vermeer and A. Verruijt. An accuracy condition for consolidation by finite elements. *Int. J. Numer. Anal. Meth. Geomech.*, 5(1):1–14, 1981. ISSN 1096-9853.

B. Vernon-Roberts, N.L. Fazzalari, and B.A. Manthey. Pathogenesis of tears of the anulus investigated by multiple-level transaxial analysis of the t12-l1 disc. *Spine*, 22(22):2641–2646, 1997.

D.R. Wagner and J.C. Lotz. Theoretical model and experimental results for the nonlinear elastic behavior of human annulus fibrosus. *Journal of Orthopaedic Research*, 22(4):901–909, JUL 2004. ISSN 0736-0266. doi: 10.1016/j.orthres.2003.12.012.

J.L. Wang, M. Parnianpour, A. Shirazi-Adl, A.E. Engin, S. Li, and A. Patwardhan. Development and validation of a viscoelastic finite element model of an L2/L3 motion segment. *Theoretical and Applied Fracture Mechanics*, 28(1):81–93, 1997. ISSN 0167-8442. doi: 10.1016/S0167-8442(97)00032-3.

S. Wang, Q. Xia, P. Passias, K. Wood, and G. Li. Measurement of geometric deformation of lumbar intervertebral discs under in-vivo weightbearing condition. *Journal of Biomechanics*, 42(6):705–711, 2009. ISSN 0021-9290. doi: DOI:10.1016/j.jbiomech.2009.01.004.

A. Watanabe, L.M. Benneker, C. Boesch, T. Watanabe, T. Obata, and S.E. Anderson. Classification of intervertebral disk degeneration with axial t2 mapping. *American Journal of Roentgenology*, 189(4):936–942, October 2007. doi: 10.2214/AJR.07.2142.

H.-J. Wilke, P. Neef, M. Caimi, T. Hoogland, and L.E. Claes. New in vivo measurements of pressures in the intervertebral disc in daily life. *Spine*, 24(8):755–762, April 1999.

H.-J. Wilke, Peter Neef, B. Hinz, H. Seidel, and L. Claes. Intradiscal pressure together with anthropometric data - a data set for the validation of models. *Clinical Biomechanics*, 16(Supplement 1):111, 2001.

W. Wilson, C.C. van Donkelaar, and J.M. Huyghe. A comparison between mechano-electrochemical and biphasic swelling theories for soft hydrated tissues. *Journal Of Biomechanical Engineering-Transactions Of The Asme*, 127(1):158–165, 2005a.

W. Wilson, C.C. van Donkelaar, B. van Rietbergen, and R. Huiskes. A fibril-reinforced poroviscoelastic swelling model for articular cartilage. *Journal of Biomechanics*, 38(6):1195–1204, 2005b.

W. Wilson, C.C. van Donkelaar, R. van Rietbergen, and R. Huiskes. The role of computational models in the search for the mechanical behavior and damage mechanisms of articular cartilage. *Medical Engineering and Physics*, 27(10):810–826, DEC 2005c. ISSN 1350-4533. doi: 10.1016/j.medengphy.2005.03.004.

H. Yao, M.-A. Justiz, D. Flagler, and W.Y. Gu. Effects of swelling pressure and hydraulic permeability on dynamic compressive behavior of lumbar annulus fibrosus. *Annals of Biomedical Engineering*, 30(10):1234–1241, November 2002.